Building Molecular Electronic Devices from the Bottom Up

Julia Del Re
Department of Chemistry
McGill University, Montreal, Canada

A thesis submitted to McGill University in partial fulfillment of the requirements of the degree of doctorate of philosophy.

August 2015

This thesis is dedicated to my late grandfather Francesco Del Re whose love of learning and pursuit of knowledge has served as an inspiration for me.

Table of Contents

Abstract

Ever since Aviram and Ratner's revolutionary paper in 1974 that proposed that molecules could conduct electrical current molecular electronics has attracted a great deal of interest as a potential replacement for silicon technology. Using molecules in electronic devices offers many advantages including high device density due to their small size and the ability to integrate new functions into devices with well-designed synthesis. One such example is sensing as the conduction in a molecular wire has been shown to be incredibly sensitive to its local environment. Proof-of-concept experiments have demonstrated that the conduction of oligophenylene vinylene (OPV), a well-studied molecular wire, is sensitive to nitroaromatic molecules. In order to be able use molecules in molecular electronic devices though it is necessary to be able to control their switching between the on and off state. Preliminary work has attempted to understand how voltage-induced switching works in bipyridyl-dinitro oligophenylene ethynylene dithiol (BPDN). The subsequent step is to look at integrating these molecules into functional devices.

One proposed way for integrating conducting molecules into functional devices is to form networks of densely-packed gold nanoparticles and molecular wires between metal electrodes on insulating substrates. This design requires that nanoparticles be spaced closely enough together otherwise molecular wires will fail to bind between neighbouring nanoparticles thus decreasing device efficiency. Biomolecules have proven to be excellent templates for self-assembly and offer the advantage of being able to work under mild, aqueous conditions. Two examples are peptides and viruses. Peptides are known to provide excellent control over the size, shape and assembly of inorganic materials. Their activity can further be enhanced by fusing two different functional domains together to form a fusion peptide which is multifunctional in nature.

Viruses are highly desirable templates for self-assembly for a variety of reasons including their monodispersity and well-defined shapes. The tobacco mosaic virus is one such example and its coat protein is capable of forming different assemblies depending on pH and ionic strength. One assembly of interest is the 20S disk which is 18 nm in diameter.

In this work the Flg-A3 peptide was first used to form gold nanoparticles which can form stable aggregates upon interaction with metal ions. These aggregates are then bound in high density to silicon dioxide surfaces using the A3-QBP1 peptides. The Flg-A3 gold nanoparticles were also covalently bound to tobacco mosaic virus disks with the hopes of eventually being able to increase the size of the aggregates that it forms. The gold nanoparticles were covalently bound to the N terminus of this structure which is located on the circumference of the disk for further studies of their aggregation properties.

The final step focused on making functional devices from oligophenylene vinylene and these gold nanoparticle networks formed using fusion peptides. The nanoparticle networks were plated on silicon dioxide substrates with lithographically-defined gold electrodes. They were treated with ultraviolet ozone cleaning in order to remove the peptide prior to using these films for electrical measurements with oligophenylene vinylene.

Résumé

Depuis l'article révolutionnaire d'Aviram et Ratner en 1974 qui avait proposé que les molécules peuvent conduire l'électricité le domaine d'électroniques moléculaires a attiré beaucoup d'intérêt. L'usage des molécules dans les appareils électroniques offre plusieurs avantages incluant une haute densité dans ces systèmes á cause de leur taille petite et la possibilité d'intégrer les nouvelles fonctions dans les fils moléculaires avec la synthèse. Un exemple serait le développement d'un détecteur parce que la conduction d'une molécule est sensible à son environnement local. Les expériences ont montré que la conduction d'oligophenylene vinylene (OPV), un fil moléculaire bien étudié, diminue dans la présence des molécules nitroaromatiques. Pour utiliser les fils moléculaires dans les appareils électroniques il faut qu'ils puissent changer entre un état de conduction élevée et un état bas. Les expériences préliminaires avec bipyridyl-dinitro oligophenylene ethynylene dithiol (BPDN), une molécule qui peut changer entre les deux états avec la tension, ont essayé de découvrir un lien entre la structure et ce fonctionnement. La prochaine étape est d'intégrer ces molécules dans un appareil fonctionnel.

Une stratégie proposée pour intégrer les fils moléculaires dans un appareil fonctionnel est la formation des ensembles des fils moléculaires et nanoparticules métalliques sur les substrats isolants. Les nanoparticules doivent être assez proches sinon les fils n'attachent pas entre eux. Il faut qu'il y ait quelque chose pour contrôler l'espace. C'est établi que les biomolécules sont les modèles excellents pour diriger auto-assemblage et elles marchent sous les conditions douces et aqueuses. Les peptides et les virus sont deux exemples. Les peptides peuvent contrôler la taille, forme et l'assemblage des matières inorganiques. Si on fusionne deux domaines avec deux fonctions différentes c'est possible de créer un peptide de fusion qui est un exemple d'un

matériel multifonctionnel. Les virus sont un modèle idéal pour auto-assemblage à cause de leur monodispersité et leur forme bien définie. Le virus de la mosaïque du tabac est un virus bien étudié et il peut se former les assemblages différents qui dépendent sur pH et la force ionique. Le disque 20S, qui a un diamètre de 18 nm, est un de ces assemblages et il serait un bon modèle pour l'auto-assemblage.

Dans ce travail le peptide, Flg-A3 est utilisé pour synthétiser les nanoparticules d'or et diriger leur assemblage quand il interagit avec les ions de métal. Ces assemblages se fixent en haute densité sur les surfaces du dioxide de silicium avec le peptide A3-QBP1. Pour augmenter la région où les nanoparticules s'assemblent les nanoparticules Flg-A3 étaient attachées d'une manière covalente à l'extérieur du disque du virus de la mosaïque du tabac. Comme ça ce sera possible de former les bagues des nanoparticules et étudier leur auto-assemblage.

La dernière étape est d'intégrer oligophenylene vinylene dans ces ensembles des nanoparticules. Les assemblages des nanoparticules Flg-A3 se sont fixés sur les surfaces du dioxide de silicium avec A3-QBP1. Les substrats contiennent les électrodes d'or qui sont définies par la lithographie. Ils sont traités avec le nettoyage à l'ozone ultraviolet avant de les utiliser pour les expériences électriques avec oligophenylene vinylene.

Acknowledgements

First and foremost I would like to thank my supervisor Dr. Amy Szuchmacher Blum for all her guidance and support over the years. The enthusiasm with which you approach research with is admirable and contagious. It was a privilege to have worked in your lab and I am appreciative of the many opportunities that you provided for me. I am also grateful towards my committee members, Dr. Christopher Barrett and Dr. Dmitri Perepichka, for the fruitful discussions and valuable advice about this project as well as the access to laboratory resources necessary for it.

The past six years would not have been the same without my colleagues in the Blum group: Serene Bayram, Shoronia Cross, Dr. Katalin Korpany, Josue Lucate and Dr. Omar Zahr. It has been a pleasure working with all of you and thank you for the guidance and many laughs over the years. I would also like to thank my undergraduates who I had the honour of supervising: Jung Young Jung, Peter Quinn and Nasser Sarket. I am very appreciative of your hard work in the lab and the valuable contributions you made. I also could not forget Joël Poisson who I consider an honourary Blum group member. Thank you for the many entertaining moments over the years.

I would like to thank Dr. Alex Wahba for his expertise in mass spectroscopy and for the large amount of time he dedicated to the protein work. I am also grateful towards Mohini Ramkaran for her expertise in scanning probe microscopy and the many delightful conversations. David Liu and Line Mongeon were instrumental in succeeding in the electron microscopy portions of this work and I would like to thank them for all their time invested in training and help with the experimental work. I also would like to thank Dr. Hareem Maune, Dr. Alshakim Nelson and Dr. Jane Frommer of IBM Research, San Jose, CA who provided me the opportunity

to spend two months of my PhD there. It was an honour to have worked alongside such talented scientists and the learning experience was phenomenal.

The administrative staff of the Department of Chemistry provided invaluable support throughout my PhD and I'm very grateful towards them. I would especially like to thank Chantal Marotte for always going above and beyond the call of duty to support the graduate students and make sure that no one is left behind. I also would like to acknowledge Karen Turner and Colleen McNamee for their help in navigating the administrative side of things.

Last but not least I would like to thank my family who without their unconditional love and support I would not have made it this far. I am truly grateful for all that you have done for me and thank you for encouraging me to pursue my dreams.

Contributions of the Authors

Chapter 3

In Chapter 3 Julia Del Re carried out the fluorescence experiments, scanning tunneling microscope experiments and data analysis. Martin H. Moore of the Naval Research Laboratory synthesized the oligophenylene vinylene molecule studied in this chapter. Dr. Banahalli Ratna of the Naval Research Laboratory provided manuscript edits and experimental guidance. Dr. Amy S. Blum served as the principal investigator in this work and was responsible for edits to the manuscript and experimental guidance.

Chapter 4

Julia Del Re did all experimental work in this chapter. Dr. Amy S. Blum served as the principal investigator providing manuscript edits and experimental guidance.

Chapter 5

Julia Del Re did all experimental work in this chapter with the exception of the LC-MS which was performed by Dr. Alex Wahba. Dr. Amy S. Blum served as the principal investigator.

Chapter 6

Dr. Charles Rettner of IBM Research performed all the lithography for the gold electrode samples. Dr. Hareem Maune of IBM Research and Dr. Amy S. Blum provided experimental guidance. Julia Del Re did all Raman experiments, SEM experiments and electrical experiments. The OPV was synthesized by David Levan and Dr. Rajeswara Rao. Dr. Dmitri Perepichka provided experimental guidance on the synthetic portion of this work.

Chapter 7

Julia Del Re performed all electrical experiments. The molecular wire candidates were synthesized by Martin H. Moore of the Naval Research Laboratory. Dr. Amy S Blum provided experimental guidance.

List of Figures

List of Tables

List of Schemes

List of Abbreviations

A: Alanine
AFM:Atomic force microscopy
AuNP: Gold nanoparticle
Boc:Tertiary-butyloxycabonyl
BPDN: Bipyridyl-dinitro oligophenylene ethynylene dithiol
C: Cysteine
Cp-AFM: Conductive probe atomic force microscopy
D: Aspartic acid
DCC: N,N'-dicyclohexylcarbodiimide
DCM: Dichloromethane
DCU: Dicyclohexyl urea
DLS: Dynamic light scattering
DTT: Dithiothreitol
EDC: 1-Ethyl-3-(3-dimethylaminopropyl)carbodiimide
ESI-MS: Electrospray ionisation mass spectroscopy
F: Phenylalanine
Fmoc: 9-fluorenylmethoxycarbonyl
HOMO: Highest occupied molecular orbital
HPLC: High performance liquid chromatography
I-V: Current-voltage
K: Lysine
L: Leucine
LC-MS: Liquid chromatography – mass spectroscopy
LUMO: Lowest occupied molecular orbital
Lys: Lysine
M: Methionine
MIBK: Methyl isobutyl ketone
MOSFET: Metal oxide semiconductor field effect transistor
NHS: N-hydroxysuccinimide
NMP: N-methyl-2-pyrrolidone
OPE: Oligophenylene ethylene
OPV: Oligophenylene vinylene
P:Proline
PDMS: Polydimethylsiloxane
PMMA: Poly(methylmethacrylate)
S: Serine
SAM: Self-assembled monolayer
SEM: Scanning electron microscopy
Ser: Serine
SERS: Surface enhanced Raman spectroscopy
SPR: Surface plasmon resonance

STM: Scanning tunneling microscopy
STM-BJ: Scanning tunneling microscopy break junction
TEM: Transmission electron microscopy
THF: Tetrahydrofuran
TMAH: Tetramethylammonium hydroxide
TMV: Tobacco mosaic virus
TMVcp: Tobacco mosaic virus coat protein
UV/VIS – Ultraviolet/visible spectroscopy
W: Tryptophan
WT-TMVcp: Wild-type tobacco mosaic virus coat protein
Y: Tyrosine

Rationale for Thesis Studies

With the rapidly rising cost of production for silicon transistors a cost-effective alternative is required. Molecular electronics has been one proposed solution as molecules are incredibly small, can be produced on a large scale with ease and expensive lithographic facilities are not required to produce them. Furthermore new functions can be engineered into molecular electronic devices further expanding their potential. In order to harness the full power of molecular electronics though it is necessary to understand charge transport phenomena in single molecules and develop methods to integrate them into functional devices. One such way is to develop networks of densely-packed gold nanoparticles on insulating surfaces however a template is needed to control nanoparticle spacing and binding. Biomolecules such as peptides and viruses are two suitable templates which are simple to use.

Chapter 3 focuses on proof-of-concept experiments which demonstrate that the conduction of a well-studied molecular wire, oligo(phenylene vinylene) (OPV) is sensitive to nitroaromatic compounds thus demonstrating its potential usefulness in sensing devices. Chapter 4 examines the use of dual-affinity peptides to form densely packed networks of gold nanoparticles on silicon dioxide surfaces. These networks will be used as a means for integrating molecular wires into functional devices. The tobacco mosaic virus coat protein was studied in Chapter 5 for its ability to template the self-assembly of gold nanoparticles with the hopes of eventually being able to use these assemblies in molecular electronic devices. In Chapter 6 the networks formed in Chapter 4 were plated on silicon dioxide substrates with lithographically-defined gold electrodes with the hopes of integrating OPV into the network to form a functioning molecular electronic device. The last research chapter, Chapter 7, shows preliminary work that examines the switching mechanism in bipyridyl-dinitro oligophenylene ethynylene dithiol

(BPDN) which is known to display voltage-induced switching. The ability to switch between high and low conductance states is necessary if molecular electronics is ever to be used in technological applications.

1 Understanding the Behaviour of Single Conducting Molecules for their Use in Molecular Electronic Devices.

1.1 Preface

With the rising costs of chip production a more economical alternative is required to continue Moore's Law. Molecular electronics has been proposed as one possible solution as it provides many advantages over current silicon technology. However, there are many questions that need to be addressed. Firstly it is necessary to understand charge transport in molecules. Secondly in order for the field to be applicable in commercial applications it is necessary to develop a method for incorporating molecular wires into functional devices.

1.2 Silicon Technology

The first silicon transistor was developed by Tanenbaum et al. at Bell Laboratories in 1955[1]. The device revolutionized solid state electronics as silicon is a material with conduction properties that can easily be controlled[2]. As such it has found many uses in fields like telecommunications, computing and so on[3]. What makes silicon such a highly desirable material is that it is in its elemental form which means that the composition of the material is quite simple[2]. Furthermore it is capable of forming a highly stable oxide which is helpful in controlling current flow[4]. Lastly silicon also provides the advantage of being easily doped with other atoms to control the electrical properties of the transistor[5].

The most common design for transistors which make up integrated circuits is the metal oxide semiconductor field effect transistor (MOSFET)[6]. A MOSFET is comprised of four basic parts: the source, drain, gate and body[7]. Figure 1.1 represents a general design of a MOSFET:

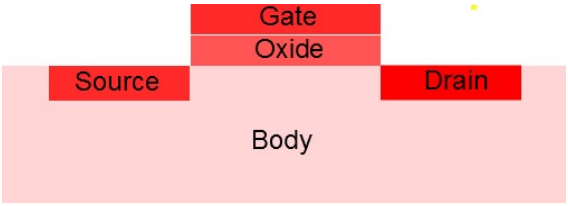

Figure 1.1 Basic design of a MOSFET

When a voltage is applied to the gate contact it generates an electric field. At a certain threshold voltage a conduction channel opens between the source and drain allowing current to flow through the body[7]. MOSFETs are most commonly used as switches or amplifiers because of this property[3].

Perhaps the greatest achievement with silicon MOSFETs has been the ability to easily scale them down, thus increasing the number of transistors on a chip, and consequently the performance of electronic devices[4]. In 1965 Gordon Moore of Intel famously stated that the number of transistors in an integrated circuit would double approximately every two years[8]. This would eventually become known as Moore's Law. Owing to the scaling rules for MOSFET device parameters developed by Dennard et al., which determine how each device parameter changes with decreasing size, as well as advances in lithographic techniques, the semiconductor industry has been able to realize Moore's law for almost five decades[9,10]. Until the 90 nm technology node, scaling was relatively simple, however after this there started to be major problems with device performance[4]. As more and more transistors are packed onto an integrated circuit, more power is required to drive all of them thus increasing heat dissipation[2]. With shrinking device dimensions, the separation between the source and drain becomes sufficiently small that current will flow even in the device's off state[10]. Lastly from an economics standpoint, as the devices become smaller they become more complex and the cost per design increases[2]. This is a result of having to rely on new, more expensive lithographic techniques to

achieve smaller device dimensions[11]. With transistor dimensions currently at 7 nm it remains to be seen how much longer Moore's Law can continue[2].

A number of solutions have been proposed that would extend Moore's Law such as modifications to the current MOSFET design[12], and the introduction of new materials such as graphene[13] and carbon nanotubes[14] to highlight a few. Molecular electronics is another area of active inquiry for this problem. The idea of being able to use molecules in conducting devices was first proposed by Aviram and Ratner in 1974[15]. Using molecules in electronic devices offers many exciting advantages, including small size dimensions which would give rise to high-density devices[16]. It would also be possible to take advantage of well-designed synthesis to integrate novel functions into molecular electronic devices[17]. Furthermore, it is quite simple to produce large quantities of molecular components during synthesis without the requirement for expensive lithographic facilities[18]. For these reasons molecular electronics is a field with a promising future. However it is first necessary to understand how molecules conduct electricity.

1.3 Understanding Charge Transport in Molecular Junctions

1.3.1 What is a Molecular Junction?

In its simplest form a molecular junction consists of a molecule sandwiched between two metal electrodes (Figure 1.2). This makes it a two terminal device. The selected metal must be very conductive with gold being a popular choice[19]. Linker groups on the end of the molecule serve to connect the central portion, the bridge, to the electrodes[20]. To date a number of linker groups have been identified and shown to play an important role in charge transport. The most popular choices tend to include thiols[21–23], carboxylic acids[24,25] and amines[26–28]. Thiols in particular are attractive due to the strength of the Au-S bond, which will ensure good molecule-electrode coupling[29]. This will be discussed in further detail in Section 1.3.3. Ideally, the

bridges tend to have a large amount of π conjugation however other variables which shall be discussed also influence whether or not a molecule will serve as a good conductor[30]. For this reason aromatic molecules tend to be a popular molecular wire candidate.

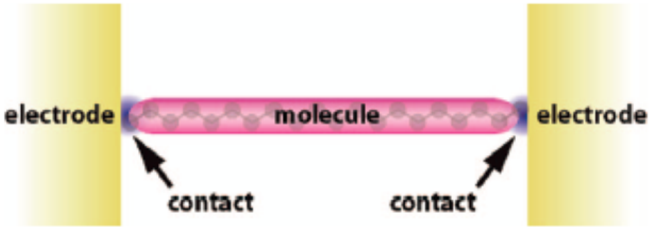

Figure 1.2 Basic schematic of a molecular junction. Reprinted with permission from Bumm, L, *ACS Nano*, **2008**, 2 (3), 403 – 407. Copyright 2008. American Chemical Society.

1.3.2 Mechanisms of Charge Transport

There are two principal mechanisms of charge transport in molecular junctions: hopping and tunneling[31]. Identifying which mechanism is responsible for charge transport is relatively simple as both are influenced by different variables. Hopping is a temperature-dependent process while tunneling is independent of this variable[18].

In tunneling electrons or holes move through the bridge or molecular wire which serves merely as medium for charge transport[32]. Multiple factors govern whether a wire will conduct through holes or electron[33]. Tunneling transport can be resonant or non-resonant depending on how the lowest unoccupied molecular orbital (LUMO) or the highest occupied molecular orbital (HOMO) align with the metal electrode's Fermi level. The Fermi level refers to the highest occupied state at 0 K[34]. This particular mechanism of charge transport is a length-dependent process that decays exponentially with length of the molecule (Equation 1.1)[35].

$$G = G_c e^{-\beta L} \qquad \text{Equation 1.1}$$

Here G is the conductance in siemens, L is the length of the molecule in Å, β is the tunneling decay constant in $Å^{-1}$ and G_c is the contact conductance in siemens[35]. It is important to note that the value of β is not unique to just the molecular wire portion or bridge of a molecular junction but to the combination of the electrodes and the wire[32]. In order for this mechanism to occur, the charge carrier (holes or electrons) must overcome the tunneling barrier. In its simplest form the tunneling barrier (φ) is the energy difference between the Fermi level (E_F) of the metal electrode and either the HOMO or LUMO of the molecular wire[36]. The charge carrier type (holes or electrons) is determined by whether the smallest tunneling barrier is φ_{HOMO} or φ_{LUMO}[37]. Figure 1.3 represents a simplified diagram of a tunneling barrier.

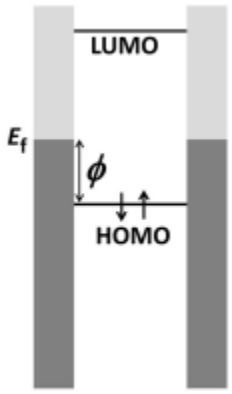

Figure 1.3 Simplified representation of a tunneling barrier. Reprinted with permission from Sayed, SY. et al, Proc. Nat. Acad. Sci., 2012, 109 (29), 11498-11503.

Owing to the fact that tunneling is a quantum mechanical effect, this mechanism only applies over distances where the electronic or hole wave function for a material extends into space[38]. This wave function refers to the probability of finding an electron in the LUMO or a hole in the HOMO respectively and is therefore limited to where in space these molecular orbitals extend. Consequently tunneling only applies to shorter molecules when discussing the mechanism of charge transfer[39].

Tunneling can further be broken down into two types: elastic and inelastic tunneling (Figure 1.4). In the former case, when a bias is applied to the system the charge carrier is injected and tunnels from one state to another without loss of energy. In this particular case, current fluctuates linearly with applied bias[40]. In inelastic tunneling, a loss of energy occurs in the tunneling charge carrier[41]. This takes place when there is a vibrational mode with some frequency ω for which the charge carrier can couple to[42]. If the applied bias is greater than the energy of this vibration then there will be an excitation of this mode, and consequently the charge carrier will tunnel through a new path that is lower in energy[43]. Equation 1.2 summarizes this relation[40].

$$eV \geq \hbar\omega \qquad \text{Equation 1.2}$$

V is the applied bias in V, e is the charge of the electron in C, $\hbar$ is Planck's constant in J s^{-1} and ω is the frequency of the vibrational mode in s^{-1}. One consequence of inelastic tunneling is that it tends to increase conductance and cause deviations from linearity in the I-V curve. Experimentally an increase in current is observed at energies that can couple to the vibrational modes[42]. This is the result of an additional path for current flow.

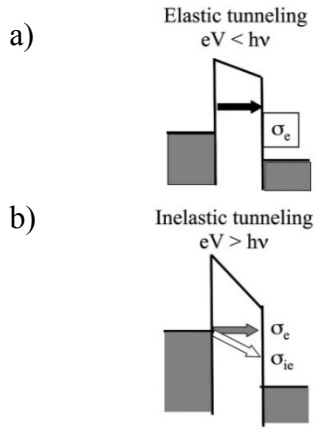

Figure 1.4 Diagrams for a) elastic tunneling and b) inelastic tunneling. Reprinted with permission from Joachim, C. et al., *Proc. Nat. Acad. Sciences*, 2005, 102 (25), 8801 – 8808. Copyright 2005. National Academy Sciences, U.S.A.

In contrast to tunneling, hopping has a weak dependence on the length of the molecule and therefore tends to be the dominant mechanism of charge transport for longer molecules[44]. If the Fermi level of the donor electrode is nearly resonant with the LUMO of the molecular wire, then hopping will be the favoured mechanism of charge transport[32]. In hopping, electron transfer occurs across the neighbouring sites of the molecular wire and involves nuclear motion, meaning that the formation of local redox states tends to occur[38]. The conduction follows an Arrhenius relation described below:

$$G \propto e^{a\frac{-E_A}{k_b T}} \qquad \text{Equation 1.3}$$

Where G is the conduction in siemens, T is temperature in K and E_A is the activation energy in kJ mol^{-1}[35]. Hopping is a thermally activated process and so enough energy must be supplied to overcome the activation energy barrier[44].

1.3.3 Variables which Contribute to Charge Transport

Many variable influence charge transport significant with the linker group being one such example[37]. For the purpose of this thesis only the –SH linker will be discussed as it is the only one used in this work. As previously mentioned, the thiol linker is a popular choice because of the ability of sulfur to form a strong covalent bond with gold electrodes with a binding energy of 167 kJ/mol[25,45]. Molecular wires containing these sorts of groups tend to tunnel through the HOMO[46]. Another advantage of thiols is that they have a low contact resistance due to the Au-S bond strength, which leads to better coupling between the HOMO in the wire and the states in the metal[25]. Despite the fact that they are relatively simple to work with, understanding how the thiol group affects charge transport is challenging. In experiments involving this particular linker, a broad range of measured conductances tends to be observed[25].

There are many reasons behind why conduction varies so much when thiols are used to contact the metal electrode. One of the most well-known is that thiols bind to Au surfaces using different geometries[27]. Theoretical work has demonstrated that these varying geometries may have a significant impact on single molecule conductance, and that certain geometries may make the wire three times more conductive than others due to the varying coupling of the wire's orbitals to the states of the gold[29,47,48]. Furthermore, it is well-established that in the presence of oxygen, the thiol (-SH) group oxidizes to form disulfide (-S-S-) bonds which would in turn lead to oligomerization or polymerization of the molecular wires[27,49]. If this did occur the wire's length would increase leading to a drop in conductance.

Another factor that influences the charge transport properties of a molecular wire is the molecule's behaviour when bound to the metal electrodes. If the bonds in the wire can undergo rotation, then the coupling between molecular orbitals is reduced at certain bond angles, thus lowering conduction[50]. Indeed, in molecules where rotation is restricted, a narrower distribution of conductances is observed[51]. There are also high frequency fluctuations like internal vibrations that can have a similar effect on the conduction[52].

The choice of metal for the electrode material is also crucial in the charge transport properties of a metal-molecule-metal junction[53]. As previously stated, the interaction between the linker group and electrode will have a significant impact on the measured resistance. In cases where the molecule is physisorbed to the electrode, the contact resistance will be higher than when it is chemisorbed[54]. Other work has further supported this observation, and determined that in wires that are covalently bound to the metal electrodes, the tunneling barrier tends to be lower thus producing lower contact resistances[55].

Moreover, metals with lower work function tend to have larger contact resistances[56]. The most fundamental reason for this is that different metals have different work functions, and this difference varies the position of the Fermi level with respect to the HOMO and LUMO of the molecular wire, thus changing the tunneling barrier (Figure 1.5). The work function is defined as the energy required to remove an electron from the highest occupied energy level in a solid to a point in the vacuum just outside its surface[57]. Equation 1.4 can be used to describe the work function mathematically:

$$\boldsymbol{W = -e\varphi - E_F} \qquad \text{Equation 1.4}$$

where W is the work function, e is the charge of the electron, E_F is the Fermi level of the metal and φ is the electrostatic potential[57]. The electrostatic potential is the amount of potential energy a point charge has at any given point in space, and equals the amount of energy required to bring a charge of opposite sign to it from infinity to that point. A handful of electrode materials have been studied for molecular electronics including palladium[58], silver[59] and platinum[60] in addition to gold. Gold electrodes tend to be the most common choice for electrodes because they are chemically inert, enabling measurements under ambient conditions, and the nature of the gold-thiol bond (a popular choice for linker) is well-understood[59].

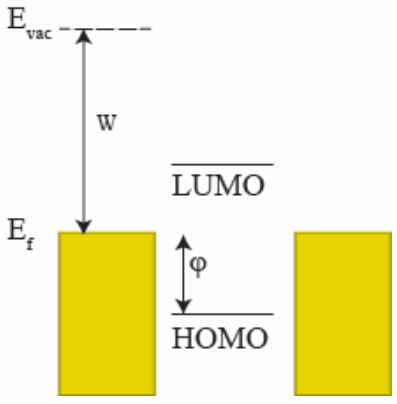

Figure 1.5 Diagram illustrating how work function, W, and the tunneling barrier, φ, are related. When the work function is larger the Fermi level, E_f is lower thus reducing the tunneling barrier.

Previous work in molecular conduction has established that wires that are rich in π conjugation and have a low degree of bond length alteration will be significantly better conductors than those that are not[30]. These criteria are known to lead to smaller HOMO-LUMO gaps which are common for good conductors[61]. The effect of increased π conjugation can best be explained by looking at Huckel theory which dictates that the π and π* orbitals must all be confined to a defined energy gap, therefore as the number of these orbitals increases the spacing between them decreases. When looking at the effect that bond-length alteration has on the HOMO-LUMO gap it is best to look at it from a solid state physics perspective. In this case a smaller degree of bond-length alteration is akin to a small Peierls transition or lesser degree of alternation in spacing between neighbouring metal atoms in a 1D chain. The smaller the Peierls distortion the better the metallic character which in turn leads to better conduction [62]. Smaller gaps lead to lower tunneling barriers thus favouring charge transport[63]. Molecular wires containing aromatic rings are frequently studied due to their rich pi conjugation. Furthermore systems involving alkynes (-C≡C-) or alkenes (-C=C-) have also been studied quite a bit for the aforementioned reasons[64].

The last effect to be discussed in detail and the one with the most relevance to this work is the effect that local environment has on charge transport in molecular wires. Indeed many studies have demonstrated that factors such as hydration in the junction[65], molecules in the vicinity of the junction[66–68] and solvent in the case of solution-phase conduction measurements[69] can influence molecular conduction. All these effects alter the difference between the electrode's Fermi level and either the HOMO or LUMO but what causes that change is highly dependent upon the environmental factor. Sometimes molecules present in the local environment will interact directly with the molecular wire via non-covalent interactions such as

π-π interactions[68,70,71]. It is thought that these lead to a change in the HOMO-LUMO gap which in turn changes the conduction[70]. This property is what makes molecular wires highly attractive candidates for sensing devices[70,72,73].

1.4 Measuring Charge Transport in Molecular Junctions

Charge transport in molecular junction is incredibly complex since many factors contribute to it as detailed in Section 1.3.3. For this reason the measured conductance of a molecular wire can vary over several orders of magnitude, and adequate sample size is required when studying the electronic properties of conducting molecules. This also means that a reliable, reproducible method of measuring conduction is necessary. Single molecules must be isolated for analysis as previous studies have shown that neighbouring molecules have an impact on the measured conductance[66]. There are several methods that have been developed, each with their own advantages and disadvantages. These include the scanning tunneling microscopy break junction method[74], mechanical break junction method[75], and conductive probe atomic force microscopy (cp-AFM) or scanning tunneling spectroscopy of isolated molecules in self-assembled monolayers (SAMs)[64,76].

The scanning tunneling break junction method (STM-BJ) was developed by Tao and coworkers (Figure 1.6). In this particular method, a gold STM tip is crashed into a gold surface in the presence of a solution of the molecular wire to be measured. The tip is then slowly retracted while measuring the conductance[18]. Initially, the conductance decreases in a step-wise manner where each step is an integer value of the quantum conductance, or the conductance of a single electron in atomic size contacts. This suggests that initially, the contacts get reduced to a one-dimensional chain of gold atoms. Following this, the chain breaks, making it possible for molecules to bridge the gap between the two electrodes. If this happens, a step is observed in the

conductance profile when it is plotted against tip sample separation[74]. If no molecule bridges the gap then the conduction does not plateau. Thousands of conductance traces can be readily collected, and a histogram can be plotted of the measured conductances, which gives a characteristic conductance value for the molecule studied[77]. This method is quite reliable for rapidly measuring the conductance of single molecules. Its main drawback though is that for dithiol molecules, the distribution of measured conductances is rather broad due to a variety of gold-thiol binding geometries and oxidation of the –SH group to form an –S-S- bond thus leading to oligomerization[27].

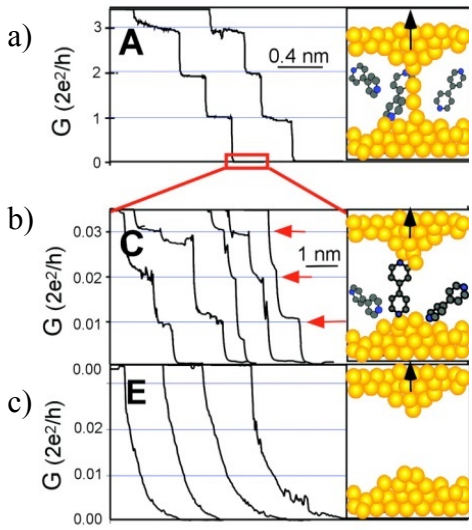

Figure 1.6 In the STM-BJ method the STM tip is first crashed into the substrate and retracted forming a 1D chain of gold atoms. b) The chain is then broken at which point molecular wires bridge the gap before c) nothing can bridge. Reprinted with permission from Xu, B. et al., *Science,* **2003**, 301 (5637), 1221 – 1223. Copyright 2006. American Society for the Advancement of Science.

In the mechanical break junction method (MC-BJ), a metal wire (typically gold) on a flexible and insulating substrate is elongated in a solution of molecular wire (Figure 1.7)[78]. Eventually the wire breaks forming a gap through which the molecules will bind. The separation between the metal contacts can be readily controlled by incorporation of a piezoelectric component into the experimental setup. This also allows for repeated back and forth bending of

the electrodes making it possible to collect an adequate number of conductance measurements for a statistical analysis[18]. This method provides the advantage of superior mechanical stability of the junctions when compared to the STM-BJ method. This is because with the STM-BJ method there is a problem with mechanical drift owing to issues such as temperature fluctuations[79]. The STM-BJ method however provides the advantage of being able to image the molecule being studied owing to the use of the scanning tunneling microscope which may provide valuable insights into its behaviour[79].

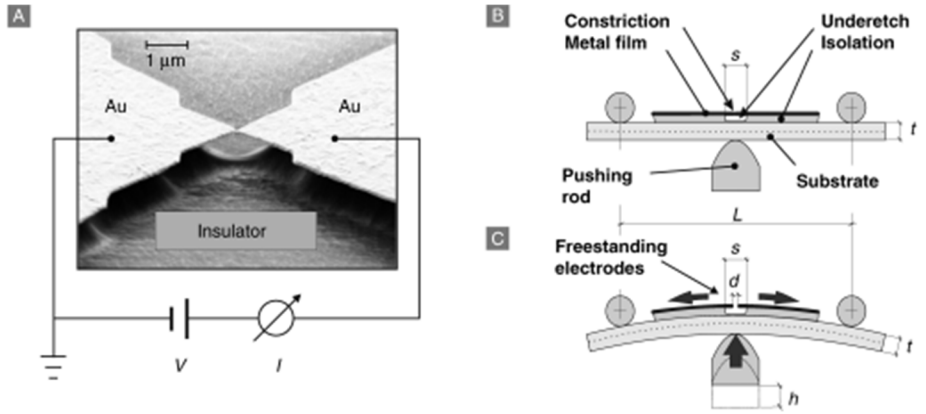

Figure 1.7 Scanning electron micrograph of a) a MC-BJ setup. b) The metal wire is mounted on a flexible substrate and c) pressure is applied until the wire breaks. Reprinted with permission from Lortscher, E. et al., *Small*, **2006**, 2 (8), 973 - 977. Copyright 2006. Wiley.

Conductive probe atomic force microscopy (cp-AFM) is an imaging mode of atomic force microscopy (AFM). In this particular mode, a metallized AFM probe is used to image the surface while a bias is applied. The probe is in constant contact with the surface, and it is quite simple to collect current-voltage data for the sample by sweeping the bias of the tip[80]. In order to study single molecules an insulating self-assembled monolayer (typically alkanethiols) is deposited on a metal surface like gold (111)[76]. Single molecular wires are then able to insert at defects in the film such as domain boundary edges or around gold vacancy islands where the insulating alkanethiol molecules will be structurally relaxed[81]. The junction can then be

completed with a metallic nanoparticle, or the AFM tip can serve as the second electrode (Figure 1.8). Cp-AFM is useful for studying highly resistive or longer molecules which cannot be studied by scanning tunneling microscopy, however precaution must be taken to minimize the loading force applied to the sample from the tip as this is known to affect conduction[80].

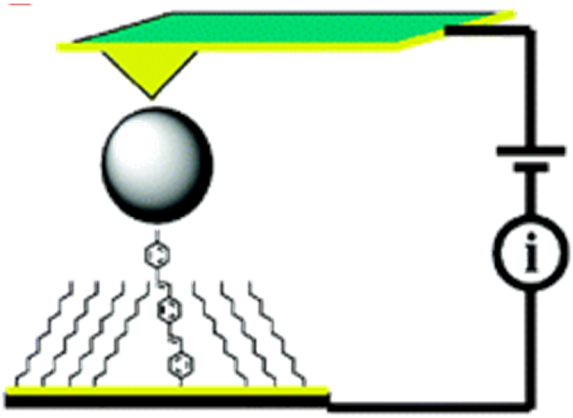

Figure 1.8 Depiction of a molecular wire isolated in an alkanethiol monolayer for study by cp-AFM. Reprinted with permission from Blum, A.S. et al., *J. Am. Chem. Soc.*, **2006**, 128 (34), 11 260 - 11267. Copyright 2006. American Chemical Society.

Using scanning tunneling spectroscopy to study the conduction of single molecules is a simple process developed by Bumm and coworkers[81,82]. An insulating alkanethiol monolayer is first deposited on an Au (111) surface[64]. As with the previous method, molecular wires can then insert into defect sites in the monolayer where they will be isolated as single molecules. The molecular junction can then be completed by functionalizing the free end of the molecular wire that is sticking out of the SAM with a gold nanoparticle[83]. Figure 1.9 provides STM images demonstrating the various steps in the formation of single molecule junctions.

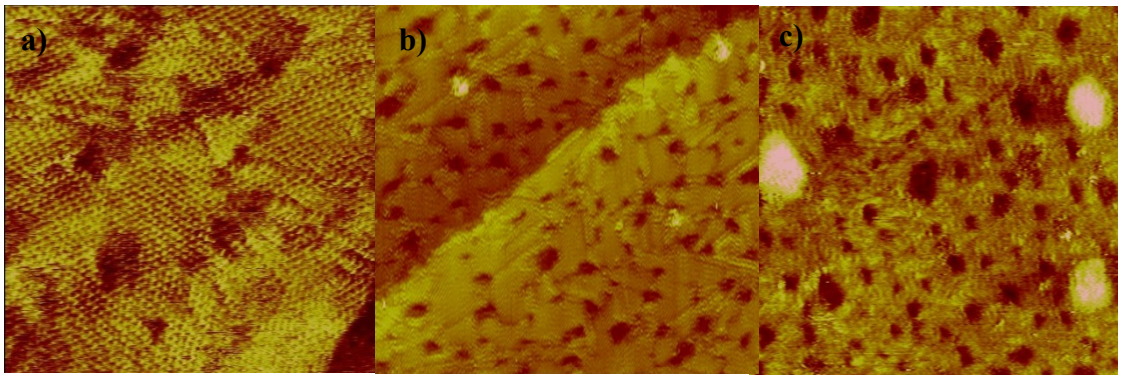

Figure 1.9 STM images of a) an insulating alkanethiol (C11) SAM, b) the C11 SAM containing single molecule wires inserted at various defect sites and c) the SAM containing molecular wires functionalized with gold nanoparticles64. The scale bar for each image is a) 25 by 25 nm^2, b) and c) 75 by 75 nm^2. Reprinted with permission from Blum, A.S. et al, *Appl. Phys. Lett.*, 2003, 82 (19), 3322- 3325. Copyright 2003. American Institute of Physics.

The resulting SAM is then characterized by scanning tunneling microscopy. The molecular junctions appear as bright protrusions in the monolayer[64]. The STM tip can then be precisely positioned over these protrusions[84]. At this point the voltage can be swept over a pre-defined range making it possible to obtain a current-voltage curve (I-V) for the given molecular junction. After amassing an adequate number of I-V curves for multiple junctions containing the same molecular wire, an average can be obtained that is representative of the molecule being studied[64]. This particular method provides the advantage of isolating conducting molecules in a well-defined insulating environment so that they can be characterized electronically[82]. Previous work has shown that while the alkanethiol monolayer may conduct some current it is not enough to contribute to the measured conduction of a π conjugated molecule should some of the alkanethiol molecules mechanically couple to the gold nanoparticle during data collection[83]. One drawback though is that as tunneling is exponentially dependent on tip-sample distance this method fails to work for longer molecules[80].

While this method of electrical characterization does present many advantages there are also several considerations to take into account. Most notably the size of the gold nanoparticle

used to complete the junction plays an important role in the I-V curve[76]. In gold nanoparticles, the energy levels are quantized, and the spacing between energy levels is inversely related to the volume of the nanoparticle (Equation 1.5)[85].

$$\delta E = \frac{2\pi^2 \hbar^2}{m_e k_f V} \qquad \text{Equation 1.5}$$

where δE is the energy gap, h is Planck's constant, m_e is the mass of the electron in kg and k_f is the Fermi wave vector while V is the volume of the nanoparticle in m^3[85]. In smaller nanoparticles (<1.5 nm) this causes a large intrinsic energy gap so the nanoparticle can charge independently of the junction which leads to distortions of the I-V curve[76]. For this reason, the size of nanoparticles being used to complete the junction must be taken into consideration.

Another consideration with this method is the position of the STM tip relative to the sample. Ideally, the tip should be in direct contact with the gold nanoparticle, however this is not so simple. In general, to achieve high resolution imaging the tip is set so that it is not in direct contact with the surface. This is due to the fact that if the tip is in direct contact with the surface there is no information that can be obtained about the surface topography[86]. That contact though is necessary for proper electrical measurements as when there is a small separation between the tip and the nanoparticle it complicates measurement of the conductance[80].

1.5 Molecular Wire Candidates

To date a large number of molecular wire candidates have been studied. The most popular include alkanedithiols[76], oligophenylene vinylenes (OPV)[70,83], and oligophenylene ethylenes (OPE)[87] (Figure 1.10). While alkanes might not seem like a reasonable choice for a molecular wire since they lack many properties of a strong conductor, they have proven to be quite useful in studying a variety of properties that are known to play a role in charge transport including

length of the wire and metal-molecule coupling[56]. This is due to their simple structure which makes it possible to vary the length of the wire without dramatic changes to the HOMO-LUMO gap. While alkanedithiols have been vital to understanding charge transport processes, a better conductor is needed for functional devices. OPEs by comparison are considered much better conductors due to the presence of a π conjugated system. They are also more versatile in that they can be readily modified to contain substituents that could impart interesting functions on the wire[88]. However, due to their ability to rotate freely about the triple bond, and the higher degree of bond-length alteration it is not as good a conductor as OPV[61].

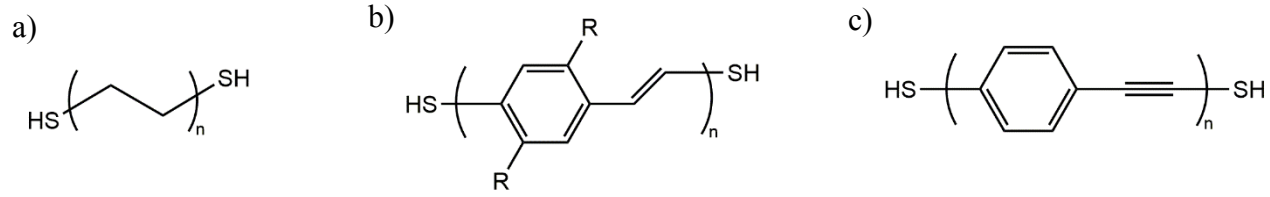

Figure 1.10 Molecular structures of a) alkanedithiols, b) OPVs and c) OPEs.

Oligophenylenevinylene (OPV) molecules are a class of wires frequently studied because they possess many properties of good molecular conductors such as a low degree of bond-length alteration and a pi conjugated, planar structure[30]. All of these properties contribute to a small HOMO-LUMO gap which is ideal for charge transport. The mechanism of charge transport in OPVs tends to be tunneling, however the charge carrier (electrons or holes) can vary depending on the linker group binding it to the metal electrodes[37,89]. In general, if the value of n is less than 5 OPV is expected to tunnel. Above this length, hopping is expected to be the dominant mechanism of charge transport[90].

1.6 Integrating Molecular Wires into Functional Devices

Creating a molecular circuit remains a challenging issue that needs to be addressed. One popular method has been to develop arrays of gold nanoparticles and molecular wires to form a

network capable of conducting electricity[91,92]. Gold nanoparticles offer the advantage of being able to form one-dimensional[93], two dimensional[94] or three dimensional assemblies[73] all of which would be highly desirable in devices thus making them a very attractive candidate. Furthermore, the plasmon of the nanoparticle has been shown to impart interesting electrical properties on the molecular network[95]. Another exciting advantage is the ability to form these assemblies using bottom up techniques[96,97]. A typical network would be a two terminal device with two lithographically-defined gold electrodes and the nanoparticle network lying between it (Figure 1.11). Networks are plated on insulating substrates such as silicon dioxide[98]. In principle measuring the current flow through one of these devices could be readily achieved using a four point probe setup.

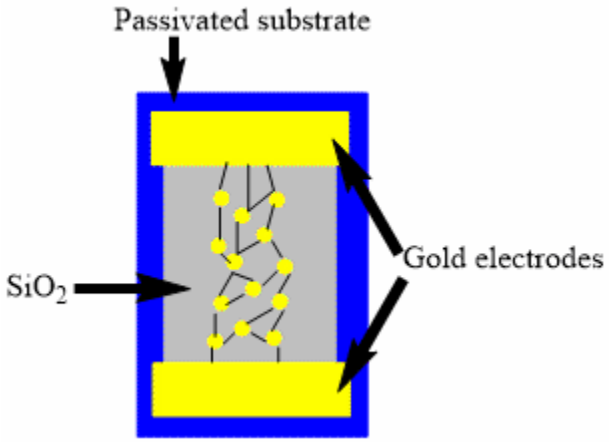

Figure 1.11 Schematic of a metal-molecule network.

One important characteristic of gold nanoparticle networks is that neighbouring nanoparticles must be spaced closely enough so that molecular wires can bridge the gap between neighbouring nanoparticles[99]. Should the nanoparticles be too far apart there will be conductive breaks in the network when molecular wires are unable to bridge between two of them[100]. There are a variety of solutions that have been proposed to achieve this. One of the most popular solutions to manufacture gold nanoparticle networks is to use self-assembly, which will be

discussed in detail in another section[101]. However in order to achieve a nanoparticle assembly on a substrate a suitable method of sample preparation is required. A variety of methods have been developed that achieve this. One popular technique is to deposit the nanoparticles first on the substrate then introduce the conducting molecule into the device[95]. Other groups have also had great success by having the gold nanoparticles assemble in solution[102] or at the liquid-air interface[103]. The resulting assemblies can then be deposited on insulating substrates using a variety of methods such as microcontact printing[94], drop-casting[101], or dip-coating[104] . All these methods provide the advantage of being relatively simple and do not require clean-room facilities.

As the networks involve large numbers of molecular junctions, understanding their charge transport properties is no easy task. As previously mentioned charge transport in single molecules is complex and influenced by many factors. In networks, there exists a series of molecular resistors in parallel and series[105]. At the macroscopic scale, Ohm's Law states that for a parallel circuit and series circuit respectively:

$$\boldsymbol{Parallel\ circuits}: \frac{\mathbf{1}}{\boldsymbol{R}} = \frac{\mathbf{1}}{\boldsymbol{R_1}} + \frac{\mathbf{1}}{\boldsymbol{R_2}} + \cdots + \frac{\mathbf{1}}{\boldsymbol{R_n}} \qquad \text{Equation 1.6}$$

$$\boldsymbol{Series\ circuits}: \boldsymbol{R} = \boldsymbol{R_1} + \boldsymbol{R_2} + \cdots \boldsymbol{R_n} \qquad \text{Equation 1.7}$$

where R represents the resistance in ohms (Ω). This classical equation cannot be applied to molecular systems, as there are cooperative effects between neighbouring wires that cause a deviation from classical behaviour[106]. Such cooperative effects include vibrational coupling between neighbouring molecules[107] as well as non-covalent interactions[68]. Furthermore, other factors such as the nature of the molecular wire being used[108] and various characteristics of the metallic nanoparticle also play a role[109].

Nanoparticle spacing also plays an important role in the electrical properties of networks[102]. The reasoning behind this though extends far beyond the ability of molecular wires to bridge the gap between neighbouring nanoparticles. Studies have found a length dependence on the molecular wire bridging the gap between neighbouring nanoparticles[110]. The conduction through the network seems to decay exponentially with increasing molecular wire length and consequentially, nanoparticle spacing indicating tunneling effects[110]. Equation 1.8 represents the relationship between nanoparticle spacing and the conductivity of the film:

$$\sigma \sim e^{-Bs} \qquad \text{Equation 1.8}$$

σ is the conductivity of the film, B is the tunneling decay constant and s is the nanoparticle separation[110]. If the nanoparticles are close enough to each other than they will couple and display metallic behaviour[102]. However, at larger separations, the Coulomb blockade is observed and the network becomes an insulating film even with molecular wires bridging the gap between neighbouring nanoparticles[109].

Another important characteristic that affects charge transport is whether or not the nanoparticles are in a 1-dimensional, 2-dimensional or 3-dimensional arrangement[103]. It is suspected that the greater the dimensionality, the greater the number of paths for current to flow which as a result leads to higher conductivity[91]. The current measured in weakly coupled gold nanoparticle networks has been found to be related to the dimensionality via the relation in Equation 1.9:

$$I \propto (V - V_T)^{\zeta} \qquad \text{Equation 1.9}$$

I is the current, V is the applied voltage, V_T is a threshold voltage below which no current will flow and ζ is a scaling constant that is dependent on the dimensionality of the network[111]. An early study by Xu et al has confirmed that the scaling constant is lower with decreased

dimensionality[112]. This result has since been reinforced by other studies which demonstrate that with higher dimensionality there is improvement in current flow through the network[103,113].

Lastly, the substrate underlying the gold nanoparticles must also be considered. In order to verify that any electrical properties measured are a result of the metal nanoparticle-molecule junctions it is absolutely necessary that the underlying substrate be insulating in nature. Silicon dioxide has proved to be a popular choice for two terminal devices, as it has it has been shown to be sufficiently insulating, thus contributing negligibly to the measured current[114]. The main consideration that should be taken into account with the underlying oxide layer is the thickness of it. If the oxide is too thin, there will be issues with leakage current from the underlying silicon layer[10]. This will in turn contribute to the measured current thus introducing an error into the results. In general if the oxide is thicker than 200 nm, the substrate will not display conducting behaviour[114].

1.7 Sensing Nitroaromatic Molecules using Molecular Electronic Devices

Due to the sensitivity of charge transport in molecules to the local environment, molecular electronics is thought to have application in fields such as sensing[72,73]. Previous work on using electrical signals in a sensor has demonstrated numerous advantages such as low detection limits[115], rapid detection[116] and specificity[117]. Perhaps one of the greatest advantages though is that a sensor of this sort would be very flexible in the sense that synthetic techniques could be applied to develop a molecular wire capable of detecting all sorts of analytes. These include metal ions[118], biomolecules[73] and nitroaromatic compounds[70]. While there has been significant research into using both organic field effect transistors in sensing[119–122] as well as inorganic materials[123,124] for electrical sensing, there is still limited work on molecular electronic based sensors[73].

Detecting nitroaromatic molecules has long been an important issue in sensing research due to their widespread use in explosives, detrimental environmental effects and toxicity[125]. Developing a sensor for these molecules remains challenging. The ideal sensor should have low detection limits[126], capable of rapid detection[127], and be highly selective for the analyte in question to minimize the risk of false positives[128]. Many of the current detection systems in use today such as mass spectrometry[129], ion mobility spectrometry[130] and gas chromatography[131] are quite sensitive but are impractical for rapid detection, or are very expensive[132]. Optical sensors that rely on measuring the change in fluorescence signal upon analyte exposure are highly desirable as they fulfill the aforementioned criteria[133–135]. Fluorescent polymers have commonly been explored in nitroaromatic sensing device and have been shown to be highly efficient sensors[133,136,137]. However, polymers can adopt random conformations which make them inaccessible to analyte molecules, and in the solid state are less permeable to the analyte which reduces the sensitivity[138]. They are also susceptible to photobleaching and photodegration[139]. For this reason molecular electronic devices where the conducting molecule adopts a more rigid structure would make a much more suitable alternative. An understanding though at the processes driving the sensing capabilities is necessary. For that reason it is necessary to look at fluorescence-based systems where the processes driving the sensing interaction are very well understood.

Fluorescence sensors for nitroaromatics are often based on electron transfer from the sensor molecule to the analyte that in turn leads to a quenching of the fluorescence signal[133,138,140,141]. This is because aromatic analytes with electron-withdrawing substituents such as $-NO_2$ tend to have low energy empty π^* orbitals which are ideal for accepting an excited electron from the sensing molecule[132,133]. This in turn facilitates the electron transfer process.

Figure 1.12 provides a simplified diagram of the electron transfer mechanism often employed in fluorescence-based sensing.

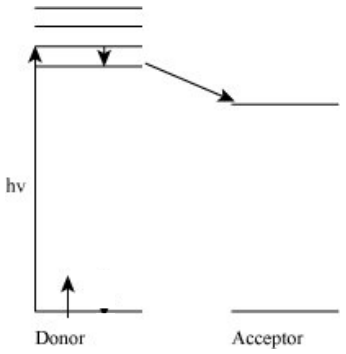

Figure 1.12 Diagram depicting the fluorescence quenching mechanism in fluorescence based-sensors. An electron in the sensing molecule is excited after which it is transferred to the analyte molecule thus quenching the fluorescence intensity.

The sort of electron transfer employed in fluorescence-based sensing systems can serve as a model for understanding energy transfer in systems where two aromatic molecules are undergoing a π donor-acceptor interaction (Figure 1.13). This sort of interaction is noncovalent in nature and occurs when one aromatic molecule is rich in electron-donating groups while the other is rich in electron-withdrawing groups. The electron-withdrawing groups shift electron density away from the aromatic core while the electron donating-groups have the opposite effect thus leading to an interaction between the two that is electrostatic in nature[142].

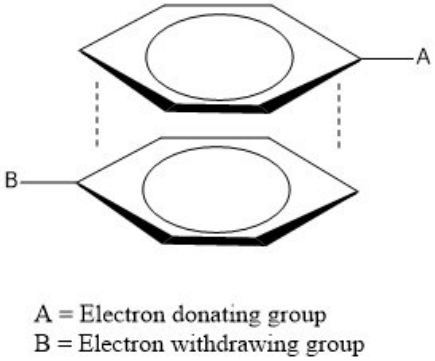

Figure 1.13 Basic representation of a π donor-acceptor interaction which is noncovalent in nature.

The energy transfer that occurs as a result of a π donor-acceptor interaction could also be employed in molecular electronic based systems to design a sensor for nitroaromatic molecules. As previously mentioned, π conjugated structures are frequently studied for their use as molecular wires because of the delocalized electrons along their molecular backbone which makes them good conductors[64,70,71,143]. These same properties could also make them good sensors. With synthetic methods it would be quite simple to incorporate an electron-donating moiety into the molecular wire thus making it a likely target for a π donor-acceptor interaction with a nitroaromatic analyte. One such example would be oligo(phenylene vinylene) (OPV) which has been extensively studied for its use as a molecular wire[64,70,143,144]. OPV is known to conduct through hole transport (Figure 1.14)[144]. It is expected that in the presence of an electron-withdrawing analyte will shift electron density away from the wire thus stabilizing the higher energy electrons and shifting the HOMO downwards[18]. This would in turn increase the tunneling barrier and should cause a measurable decrease in current.

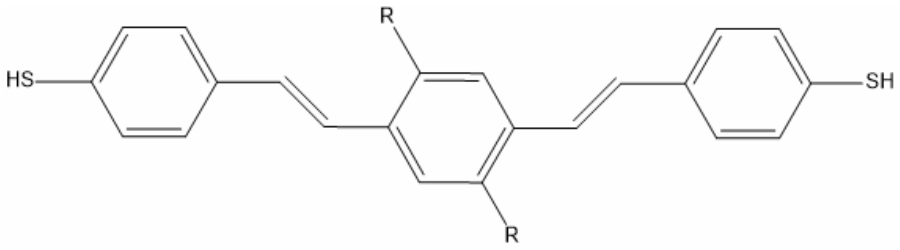

Figure 1.14 Oligo(phenylenevinylene), a frequently studied molecular wire. If the R groups are electron-donating in nature it would make a suitable candidate for use in a sensor for nitroaromatic molecules.

The proposed design for a molecular electronic sensor would be a network consisting of gold nanoparticles and the OPV molecules. This network would lie between two gold electrodes on a silicon dioxide substrate which is selected for its insulating properties. The design is identical to what was proposed in Figure 1.11. The conductivity of this network could be readily measured using four point probe techniques before and after analyte exposure to look for any

measurable changes. For this particular system the conductivity of the OPV network would be expected to drop after exposure to nitroaromatic compounds. Theoretical studies suggest that OPV networks can detect a handful of nitroaromatic molecules however experimental studies are needed to determine the actual limits of detection of the system and whether or not they are low enough to be an improvement over current technologies[72].

1.8 Conclusion

With the costs of chip fabrication rising rapidly a viable replacement is necessary to continue Moore's Law. Molecular electronics is one proposed solution as molecules offer many promising advantages. Understanding their behaviour though is difficult as these systems are complex and many variables affect their charge transport properties. Furthermore, in order for molecules to be applicable there must be a way to integrate them into functional devices. Networks of metallic nanoparticles and molecular wires have been proposed. These networks would be plated on insulating substrates with lithographically-defined metal electrodes to complete the setup.

As previously mentioned molecular electronics offers many exciting advantages with one being the ability to integrate novel functions into molecular wires through well-designed molecular synthesis. Were a molecular wire rich in aromatic rings and electron-donating groups designed it could potentially serve as a sensor for nitroaromatic analytes. Nitroaromatics contain electron-withdrawing nitro groups thus this creates the potential for a π donor-acceptor interaction between the analyte and wire which in turn could create a measurable change in the electrical current.

1.9 References

(1) Tanenbaum, M.; Valdes, L. B.; Buehler, E.; Hannay, N. B. *J. Appl. Phys.* **1955**, *26* (1955), 686–692.
(2) Duhan, S.; Tomer, V. *Advanced Electronics: Looking Beyond Silicon*; 2014.
(3) Radamson, Henry, Thylen, L. *Monolithic Nanoscale Photonics–Electronics Integration in Silicon and Other Group IV Elements*; 2015.
(4) Collaert, N.; Alian, a; Arimura, H.; Boccardi, G.; Eneman, G.; Franco, J.; Ivanov, T.; Lin, D.; Loo, R.; Merckling, C.; Mitard, J.; Pourghaderi, M. a; Rooyackers, R.; Sioncke, S.; Sun, J. W.; Vandooren, a; Veloso, a; Verhulst, a; Waldron, N.; Witters, L.; Zhou, D.; Barla, K.; Thean, a V. *Microelectron. Eng.* **2014**, *132*, 218–225.
(5) Kuhn, K. J. *Microelectron. Eng.* **2011**, *88* (7), 1044–1049.
(6) Radamson, H.; Thylen, L. In *Monolithic Nanoscale Photonics–Electronics Integration in Silicon and Other Group IV Elements*; Elsevier Ltd, 2015; pp 1–61.
(7) Radamson, H.; Thylén, L. *Monolithic Nanoscale Photonics–Electronics Integration in Silicon and Other Group IV Elements*; Elsevier, 2015.
(8) Moore, G. E. *Electronics* **1965**, *38* (1), 114–117.
(9) Dennard, R. H.; Gaensslen, F. H.; Yu, H.-N.; Rideout, V. L.; Bassous, E.; Leblanc, A. R. *IEEE J. Solid-State Circuits* **1974**, *9* (5), 256–268.
(10) Ahmed, K.; Schuegraf, K. *IEEE Spectr.* **2011**, *48*, 50–56.
(11) Wong, H.; Iwai, H. *Microelectron. Eng.* **2015**, *138*, 57–76.
(12) Iwai, H. In *Chip in Curitiba 2013 - SBMicro 2013: 28th Symposium on Microelectronics Technology and Devices*; Elsevier Ltd, 2013; pp 1–12.
(13) Wang, M. C.; Chun, S.; Han, R. S.; Ashraf, A.; Kang, P.; Nam, S. *Nano Lett.* **2015**, *15* (3), 1829–1835.
(14) Tulevski, G. S.; Franklin, A.; Frank, D.; Lobez, J.; Cao, Q.; Park, H.; Afzali, A.; Han, S.; Hannon, J.; Haensch, W. *ACS Nano* **2014**, No. 9, Accepted.
(15) Aviram, A.; Ratner, M. A. *Chem. Phys. Lett.* **1974**, *29* (2), 277–283.
(16) Lörtscher, E. *Nat. Nanotechnol.* **2013**, *8* (6), 381–384.
(17) Mahmoud, A. M.; Bergren, A. J.; Pekas, N.; McCreery, R. L. *Adv. Funct. Mater.* **2011**, *21* (12), 2273–2281.
(18) Song, H.; Reed, M. a; Lee, T. *Adv. Mater.* **2011**, *23* (14), 1583–1608.
(19) Cao, Y.; Steigerwald, M. L.; Nuckolls, C.; Guo, X. *Adv. Mater.* **2010**, *22* (1), 20–32.
(20) Heath, J. R. *Annu. Rev. Mater. Res.* **2009**, *39* (1), 1–23.
(21) Vericat, C.; Vela, M. E.; Benitez, G.; Carro, P.; Salvarezza, R. C. *Chem. Soc. Rev.* **2010**, *39* (5), 1805–1834.
(22) Kay, N. J.; Nichols, R. J.; Higgins, S. J.; Haiss, W.; Sedghi, G.; Schwarzacher, W.; Mao, B.-W. *J. Phys. Chem. C* **2011**, *115* (43), 21402–21408.
(23) Diez-Perez, I.; Li, Z.; Guo, S.; Madden, C.; Huang, H.; Che, Y.; Yang, X.; Zang, L.; Tao, N. *ACS Nano* **2012**, *6* (8), 7044–7052.
(24) Ahn, S.; Aradhya, S. V; Klausen, R. S.; Capozzi, B.; Roy, X.; Steigerwald, M. L.; Nuckolls, C.; Venkataraman, L. *Phys. Chem. Chem. Phys.* **2012**, *14* (40), 13841–13845.
(25) Chen, F.; Li, X.; Hihath, J.; Huang, Z.; Tao, N. *J. Am. Chem. Soc.* **2006**, *128* (49), 15874–15881.
(26) Arroyo, C. R.; Leary, E.; Castellanos-Gómez, A.; Rubio-Bollinger, G.; González, M. T.; Agraït, N. *J. Am. Chem. Soc.* **2011**, *133* (36), 14313–14319.

(27) Venkataraman, L.; Klare, J. E.; Tam, I. W.; Nuckolls, C.; Hybertsen, M. S.; Steigerwald, M. L. *Nano Lett.* **2006**, *6* (3), 458–462.
(28) Pauly, F.; Scheer, E.; Kim, Y.; Hellmuth, T. J.; Marius, B. *ACS Nano* **2011**, *5* (5), 4104–4111.
(29) Häkkinen, H. *Nat. Chem.* **2012**, *4* (6), 443–455.
(30) Kushmerick, J. G.; Holt, D. B.; Pollack, S. K.; Ratner, M. a; Yang, J. C.; Schull, T. L.; Naciri, J.; Moore, M. H.; Shashidhar, R. *J. Am. Chem. Soc.* **2002**, *124* (36), 10654–10655.
(31) Na, J.-S.; Ayres, J.; Chandra, K. L.; Gorman, C. B.; Parsons, G. N. *Nanotechnology* **2007**, *18* (42), 424001.
(32) Weiss, E. a; Wasielewski, M. R.; Ratner, M. a. *Top. Curr. Chem.* **2005**, *257* (July), 103–133.
(33) Peng, G.; Strange, M.; Thygesen, K. S.; Mavrikakis, M. *J. Phys. Chem. C* **2009**, *113* (49), 20967–20973.
(34) Iadonisi, G.; Cantele, G.; Chiofalo, M. L. *Introduction to Solid State Physics and Crystalline Nanostructures*; 2014.
(35) Hines, T.; Diez-Perez, I.; Hihath, J.; Liu, H.; Wang, Z.-S.; Zhao, J.; Zhou, G.; Müllen, K.; Tao, N. *J. Am. Chem. Soc.* **2010**, *132* (33), 11658–11664.
(36) Sayed, S.; Fereiro, J.; Yan, H.; McCreery, R.; Bergren, A. *Proc. Natl. Acad. Sci. U. S. A.* **2012**, *109* (29), 11498–11503.
(37) Zangmeister, C. D.; Beebe, J. M.; Naciri, J.; Kushmerick, J. G.; van Zee, R. D. *Small* **2008**, *4* (8), 1143–1147.
(38) McCreery, R. L.; Yan, H.; Bergren, A. J. *Phys. Chem. Chem. Phys.* **2012**, 1065–1081.
(39) Kocherzhenko, A. a; Grozema, F. C.; Siebbeles, L. D. a. *Phys. Chem. Chem. Phys.* **2011**, *13* (6), 2096–2110.
(40) Reed, M. a. *Mater. Today* **2008**, *11* (11), 46–50.
(41) Ward, D. R.; Corley, D. A.; Tour, J. M.; Natelson, D. *Nat. Nanotechnol.* **2011**, *6* (1), 33–38.
(42) Hihath, J.; Tao, N. *Prog. Surf. Sci.* **2012**, *87* (9-12), 189–208.
(43) Joachim, C.; Ratner, M. a. *Proc. Natl. Acad. Sci. U. S. A.* **2005**, *102* (25), 8801–8808.
(44) Tao, N. J. *Nat. Nanotechnol.* **2006**, *1* (3), 173–181.
(45) Ulman, A. *Chem. Rev.* **1996**, *96* (4), 1533–1554.
(46) Aradhya, S. V.; Venkataraman, L. *Nat. Nanotechnol.* **2013**, *8* (6), 399–410.
(47) Basch, H.; Cohen, R.; Ratner, M. a. *Nano Lett.* **2005**, *5* (9), 1668–1675.
(48) Dhungana, K. B.; Mandal, S.; Pati, R. *J. Phys. Chem. C* **2012**, *116* (32), 17268–17273.
(49) Wirde, M.; Gelius, U.; Nyholm, L. **1999**, No. 26, 6370–6378.
(50) Nozaki, D.; Toher, C.; Cuniberti, G. *J. Phys. Chem. Lett.* **2013**, *4* (23), 4192–4195.
(51) Dell, E. J.; Capozzi, B.; Dubay, K. H.; Berkelbach, T. C.; Moreno, J. R.; Reichman, D. R.; Venkataraman, L.; Campos, L. M. *J. Am. Chem. Soc.* **2013**, *135* (32), 11724–11727.
(52) Malen, J. a; Doak, P.; Baheti, K.; Tilley, T. D.; Majumdar, A.; Segalman, R. a. *Nano Lett.* **2009**, *9* (10), 3406–3412.
(53) Yaliraki, S.; Kemp, M.; Ratner, M. *J. Am. Chem. Soc.* **1999**, *121* (14), 3428–3434.
(54) Beebe, J. M.; Engelkes, V. B.; Miller, L. L.; Frisbie, C. D. *J. Am. Chem. Soc.* **2002**, *124* (38), 11268–11269.
(55) Kim, B.; Choi, S. H.; Zhu, X.-Y.; Frisbie, C. D. *J. Am. Chem. Soc.* **2011**, *133* (49), 19864–19877.
(56) Engelkes, V. B.; Beebe, J. M.; Frisbie, C. D. *J. Am. Chem. Soc.* **2004**, *126* (43), 14287–

14296.
(57) Kiejna, A.; Wojciechowski, Kazimierz, F. *Metal Surface Electron Physics*, 1st ed.; Elsevier Ltd: Tarrytown, NY, 1996.
(58) Chang, S.; Sen, S.; Zhang, P.; Gyarfas, B.; Ashcroft, B.; Lefkowitz, S.; Peng, H.; Lindsay, S. *Nanotechnology* **2012**, *23* (42), 425202.
(59) Kim, T.; Vazquez, H.; Hybertsen, M. S.; Venkataraman, L. *Nano Lett.* **2013**.
(60) Nakazumi, T.; Kaneko, S.; Matsushita, R.; Kiguchi, M. *J. Phys. Chem. C* **2012**, *116* (34), 18250–18255.
(61) Kushmerick, J. J.; Pollack, S. K.; Yang, J. C.; Naciri, J.; Holt, D. B.; Ratner, M. a.; Shashidhar, R. *Ann. N. Y. Acad. Sci.* **2003**, *1006* (1), 277–290.
(62) Peierls, R. E. *Quantum Theory of Solids*, 1st ed.; Oxford University Press: London, UK, 1955.
(63) Vuillaume, D. *Arxiv Prepr. arXiv0902.0213* **2009**, *III*.
(64) Blum, A. S.; Yang, J. C.; Shashidhar, R.; Ratna, B. *Appl. Phys. Lett.* **2003**, *82* (19), 3322.
(65) Long, D. P.; Lazorcik, J. L.; Mantooth, B. a; Moore, M. H.; Ratner, M. a; Troisi, A.; Yao, Y.; Ciszek, J. W.; Tour, J. M.; Shashidhar, R. *Nat. Mater.* **2006**, *5* (11), 901–908.
(66) Selzer, Y.; Cai, L.; Cabassi, M. a; Yao, Y.; Tour, J. M.; Mayer, T. S.; Allara, D. L. *Nano Lett.* **2005**, *5* (1), 61–65.
(67) Reuter, M.; Solomon, G.; Hansen, T.; Seideman, T.; Ratner, M. *J. Phys. Chem. Lett.* **2011**, *2* (14), 1667–1671.
(68) Martín, S.; Grace, I.; Bryce, M. R.; Wang, C.; Jitchati, R.; Batsanov, A. S.; Higgins, S. J.; Lambert, C. J.; Nichols, R. J. *J. Am. Chem. Soc.* **2010**, *132* (26), 9157–9164.
(69) Fatemi, V.; Kamenetska, M.; Neaton, J. B.; Venkataraman, L. *Nano Lett.* **2011**, *11* (5), 1988–1992.
(70) Del Re, J.; Moore, M. H.; Ratna, B. R.; Blum, A. S. *Phys. Chem. Chem. Phys.* **2013**, *15* (21), 8318–8323.
(71) Wu, S.; González, M. T.; Huber, R.; Grunder, S.; Mayor, M.; Schönenberger, C.; Calame, M. *Nat. Nanotechnol.* **2008**, *3* (9), 569–574.
(72) Zimbovskaya, N. a; Pederson, M. R.; Blum, A. S.; Ratna, B. R.; Allen, R. *J. Chem. Phys.* **2009**, *130* (9), 094702.
(73) Blum, A. S.; Soto, C. M.; Sapsford, K. E.; Wilson, C. D.; Moore, M. H.; Ratna, B. R. *Biosens. Bioelectron.* **2011**, *26* (6), 2852–2857.
(74) Xu, B.; Tao, N. J. *Science* **2003**, *301* (5637), 1221–1223.
(75) Natelson, D. *ACS Nano* **2012**, *6* (4), 2871–2876.
(76) Morita, T.; Lindsay, S. *J. Am. Chem. Soc.* **2007**, *129* (23), 7262–7263.
(77) McCreery, R. L.; Bergren, A. J. *Adv. Mater.* **2009**, *21* (43), 4303–4322.
(78) Ochs, R.; Secker, D.; Elbing, M.; Mayor, M.; Weber, H. B. *Faraday Discuss.* **2006**, *131*, 281.
(79) Lee, W.; Reddy, P. *Nanotechnology* **2011**, *22* (48), 485703.
(80) Bumm, L. A. *ACS Nano* **2008**, *2* (3), 403–407.
(81) Bumm, L. A.; Arnold, J. J.; Cygan, M. T.; Dunbar, T. D.; Burgin, T. P.; Jones, L.; Allara, D. L.; Tour, J. M.; Weiss, P. S. *Science (80-.).* **1996**, *271* (5256), 1705–1707.
(82) Cygan, M. T.; Dunbar, T. D.; Arnold, J. J.; Bumm, L. A.; Shedlock, N. F.; Burgin, T. P.; Ii, L. J.; Allara, D. L.; Tour, J. M.; Weiss, P. S.; Uni, V.; Carolina, S.; October, R. V; Re, V.; Recei, M.; December, V. **1998**, *7863* (10), 2721–2732.
(83) Blum, A. S.; Kushmerick, J. G.; Pollack, S. K.; Yang, J. C.; Moore, M.; Naciri, J.;

Shashidhar, R.; Ratna, B. R. *J. Phys. Chem. B* **2004**, *108* (47), 18124–18128.
(84) Seo, K.; Konchenko, A. V; Lee, J.; Bang, G. S.; Lee, H. *J. Am. Chem. Soc.* **2008**, *130* (8), 2553–2559.
(85) Wang, B.; Wang, H.; Li, H.; Zeng, C.; Hou, J.; Xiao, X. *Phys. Rev. B* **2000**, *63* (3), 035403.
(86) Bumm, L.; Arnold, J.; Dunbar, T.; Allara, D.; Weiss, P. *J. Phys. Chem. B* **1999**, *103* (38), 8122–8127.
(87) Huber, R.; González, M. T.; Wu, S.; Langer, M.; Grunder, S.; Horhoiu, V.; Mayor, M.; Bryce, M. R.; Wang, C.; Jitchati, R.; Schönenberger, C.; Calame, M. *J. Am. Chem. Soc.* **2008**, *130* (3), 1080–1084.
(88) Blum, A. S.; Ren, T.; Parish, D. a; Trammell, S. a; Moore, M. H.; Kushmerick, J. G.; Xu, G.-L.; Deschamps, J. R.; Pollack, S. K.; Shashidhar, R. *J. Am. Chem. Soc.* **2005**, *127* (28), 10010–10011.
(89) Sikes, H. D. *Science (80-.).* **2001**, *291* (5508), 1519–1523.
(90) Schuster, S.; Scarpa, G.; Latessa, L.; Lugli, P. *Phys. Status Solidi* **2008**, *5* (1), 390–393.
(91) Noguchi, Y.; Terui, T.; Katayama, T.; Matsushita, M. M.; Sugawara, T. *Appl. Phys. Lett.* **2011**, *98* (26), 263114.
(92) Blum, A. S.; Soto, C. M.; Wilson, C. D.; Amsinck, C.; Franzon, P.; Ratna, B. R. *IEEE Trans. Nanobioscience* **2007**, *6* (4), 270–274.
(93) Acar, H.; Genc, R.; Urel, M.; Erkal, T. S.; Dana, A.; Guler, M. O. *Langmuir* **2012**, *28* (47), 16347–16354.
(94) Guédon, C. M.; Zonneveld, J.; Valkenier, H.; Hummelen, J. C.; van der Molen, S. J. *Nanotechnology* **2011**, *22* (12), 125205.
(95) Conklin, D.; Nanayakkara, S.; Park, T.-H.; Lagadec, M. F.; Stecher, J. T.; Chen, X.; Therien, M. J.; Bonnell, D. a. *ACS Nano* **2013**, *7* (5), 4479–4486.
(96) Hnilova, M.; Karaca, B. T.; Park, J.; Jia, C.; Wilson, B. R.; Sarikaya, M.; Tamerler, C. *Biotechnol. Bioeng.* **2012**, *109* (5), 1120–1130.
(97) Zhou, G.; Liu, Y.; Luo, M.; Li, X.; Xu, Q.; Ji, X.; He, Z. *Langmuir* **2013**, *29* (15), 4697–4702.
(98) Jiang, C.-W.; Ni, I.-C.; Tzeng, S.-D.; Kuo, W. *Appl. Phys. Lett.* **2012**, *101* (8), 083105.
(99) Blum, A. S.; Soto, C. M.; Wilson, C. D.; Cole, J. D.; Kim, M.; Gnade, B.; Chatterji, A.; Ochoa, W. F.; Lin, T.; Johnson, J. E.; others. *Nano Lett.* **2004**, *4* (5), 867–870.
(100) Del Re, J.; Blum, A. S. *Appl. Surf. Sci.* **2014**, *296*, 24–30.
(101) Asbahi, M.; Lim, K. T. P.; Wang, F.; Duan, H.; Thiyagarajah, N.; Ng, V.; Yang, J. K. W. *Langmuir* **2012**, *28* (49), 16782–16787.
(102) Mangold, M. A.; Calame, M.; Mayor, M.; Holleitner, A. W. *ACS Nano* **2012**, *6* (5), 4181–4189.
(103) Wang, Y.; Duan, C.; Peng, L.; Liao, J. *Sci. Rep.* **2014**, 1–6.
(104) Zhou, Y.; Han, S.-T.; Xu, Z.-X.; Roy, V. a L. *Adv. Mater.* **2012**, *24* (9), 1247–1251.
(105) Gschneidtner, T. a.; Diaz Fernandez, Y. a.; Moth-Poulsen, K. *J. Mater. Chem. C* **2013**, *1* (43), 7127.
(106) Reuter, M. G.; Hersam, M. C.; Seideman, T.; Ratner, M. a. *Nano Lett.* **2012**, *12* (5), 2243–2248.
(107) Galperin, M.; Nitzan, A. *J. Phys. Chem. B* **2013**, *117* (16), 4449–4453.
(108) Dayen, J.-F.; Devid, E.; Kamalakar, M. V.; Golubev, D.; Guédon, C.; Faramarzi, V.; Doudin, B.; van der Molen, S. J. *Adv. Mater.* **2013**, *25* (3), 400–404.

(109) Duan, C.; Wang, Y.; Sun, J.; Guan, C.; Grunder, S.; Mayor, M.; Peng, L.; Liao, J. *Nanoscale* **2013**, *5* (21), 10258–10266.
(110) Zabet-Khosousi, A.; Trudeau, P. E.; Suganuma, Y.; Dhirani, A. A.; Statt, B. *Phys. Rev. Lett.* **2006**, *96* (April), 2–5.
(111) Zabet-Khosousi, A.; Dhirani, A.-A. *Chem. Rev.* **2008**, *108* (10), 4072–4124.
(112) Xu, C.; van Zalinge, H.; Pearson, J. L.; Glidle, A.; Cooper, J. M.; Cumming, D. R. S.; Haiss, W.; Yao, J.; Schiffrin, D. J.; Proupín-Pérez, M.; Cosstick, R.; Nichols, R. J. *Nanotechnology* **2006**, *17* (14), 3333–3339.
(113) Noguchi, Y.; Terui, T.; Katayama, T.; Matsushita, M. M.; Sugawara, T. *Appl. Phys. Lett.* **2011**, *98* (26), 263114.
(114) Yao, J.; Zhong, L.; Natelson, D.; Tour, J. M. *J. Am. Chem. Soc.* **2011**, *133* (4), 941–948.
(115) Snow, A. W.; Ancona, M. G.; Park, D. *Langmuir* **2012**, *28* (44), 15438–15443.
(116) Chang, S.; Huang, S.; Liu, H.; Zhang, P.; Liang, F.; Akahori, R.; Li, S.; Gyarfas, B.; Shumway, J.; Ashcroft, B.; He, J.; Lindsay, S. *Nanotechnology* **2012**, *23* (23), 235101.
(117) Weizmann, Y.; Chenoweth, D. M.; Swager, T. M. *J. Am. Chem. Soc.* **2011**, *133* (10), 3238–3241.
(118) Das, B. *J. Phys. Chem. C* **2009**, *113* (36), 16203–16209.
(119) Yang, G.; Di, C. A.; Zhang, G.; Zhang, J.; Xiang, J.; Zhang, D.; Zhu, D. *Adv. Funct. Mater.* **2013**, *23* (13), 1671–1676.
(120) Kong, H.; Jung, B. J.; Sinha, J.; Katz, H. E. *Chem. Mater.* **2012**, *24* (14), 2621–2623.
(121) Dudhe, R. S.; Sinha, J.; Kumar, A.; Rao, V. R. *Sensors Actuators B Chem.* **2010**, *148* (1), 158–165.
(122) Ammu, S.; Dua, V.; Srikanth, R. A.; Surwade, S. P.; Phulgirkar, A.; Patel, S.; Manohar, S. K. *J. Am. Chem. Soc.* **2012**, *134* (10), 4553–4556.
(123) Park, M.; Cella, L. N.; Chen, W.; Myung, N. V; Mulchandani, A. *Biosens. Bioelectron.* **2010**, *26* (4), 1297–1301.
(124) Cho, E. S.; Kim, J.; Tejerina, B.; Hermans, T. M.; Jiang, H.; Nakanishi, H.; Yu, M.; Patashinski, A. Z.; Glotzer, S. C.; Stellacci, F.; Grzybowski, B. a. *Nat. Mater.* **2012**, *11* (9), 1–8.
(125) Salinas, Y.; Martínez-Máñez, R.; Marcos, M. D.; Sancenón, F.; Costero, A. M.; Parra, M.; Gil, S. *Chem. Soc. Rev.* **2012**, *41* (3), 1261–1296.
(126) Bianchi, F.; Bedini, A.; Riboni, N.; Pinalli, R.; Gregori, A.; Sidisky, L.; Dalcanale, E.; Careri, M.; Chimica, D.; Parma, U.; Parma, U.; Area, P.; Carabinieri, R.; Scienti, I.; No, Q. **2014**.
(127) Wang, Y.; La, A.; Ding, Y.; Liu, Y.; Lei, Y. *Adv. Funct. Mater.* **2012**, *22* (17), 3547–3555.
(128) Ma, Y.; Li, H.; Peng, S.; Wang, L. *Anal. Chem.* **2012**, *84* (19), 8415–8421.
(129) Forbes, T. P.; Sisco, E. *Anal. Chem.* **2014**, *86* (15), 7788–7797.
(130) Verkouteren, J. R.; Lawrence, J.; Klouda, G. a; Najarro, M.; Grandner, J.; Verkouteren, R. M.; York, S. J. *Analyst* **2014**, *139* (21), 5488–5498.
(131) Collin, W. R.; Serrano, G.; Wright, L. K.; Chang, H.; Nuñovero, N.; Zellers, E. T. *Anal. Chem.* **2014**, *86* (1), 655–663.
(132) Toal, S. J.; Trogler, W. C. *J. Mater. Chem.* **2006**, *16* (28), 2871.
(133) Balan, B.; Vijayakumar, C.; Tsuji, M.; Saeki, A.; Seki, S. *J. Phys. Chem. B* **2012**, *116* (34), 10371–10378.
(134) Xia, Y.; Song, L.; Zhu, C. *Anal. Chem.* **2011**, *83* (4), 1401–1407.

(135) Ma, H.; Gao, R.; Yan, D.; Zhao, J.; Wei, M. *J. Mater. Chem. C* **2013**, *1* (26), 4128.
(136) Yang, X.; Shen, B.; Jiang, Y.; Zhao, Z.; Wang, C.; Ma, C.; Yang, B.; Lin, Q. *J. Mater. Chem. A* **2013**, *1* (4), 1201.
(137) Rose, A.; Zhu, Z.; Madigan, C. F.; Swager, T.; Bulovic, V. *Nature* **2005**, *434* (7035), 876–879.
(138) Kumar, S.; Venkatramaiah, N.; Patil, S. *J. Phys. Chem. C* **2013**, *117* (14), 7236–7245.
(139) Germain, M. E.; Knapp, M. J. *Chem. Soc. Rev.* **2009**, *38* (9), 2543–2555.
(140) Chen, W.; Zuckerman, N. B.; Konopelski, J. P.; Chen, S. *Anal. Chem.* **2010**, *82* (2), 461–465.
(141) Gopalakrishnan, D.; Dichtel, W. R. *J. Am. Chem. Soc.* **2013**, *135* (22), 8357–8362.
(142) Martinez, C. R.; Iverson, B. L. *Chem. Sci.* **2012**, *3* (7), 2191.
(143) Lu, Q.; Yao, C.; Wang, X.; Wang, F. *J. Phys. Chem. C* **2012**, *116* (33), 17853–17861.
(144) Davis, W. B.; Svec, W. A.; Ratner, M. A. *Nature* **1998**, *396* (6706), 60–63.

2 Forming Structures with Nano-size Dimensions from the Bottom Up

2.1 Preface

Though forming functional devices with molecular-size dimensions is challenging, self-assembly, which forms larger structures from small subunits, is one possibility for the development of molecular electronic devices. Often times templates are used to drive self-assembly and form highly ordered structures. Biomolecules are a popular choice both because nature provides an excellent model for highly ordered self-assembled systems and because they work under mild, aqueous conditions.

2.2 Bottom-Up Self-Assembly of Metallic Nanoparticles for Incorporation in Molecular Electronic Devices

As described in the previous chapter networks of conducting molecules and metallic nanoparticles are a promising solution for forming molecular electronic devices. One major challenge for the development of molecular networks that remains to be addressed is in forming densely-packed assemblies of metallic nanoparticles on surfaces. In order to successfully integrate conducting molecules into functional devices, it is necessary to be able control the assembly and spacing between neighbouring nanoparticles down to the nanometer scale. Failure to do so would cause conductive breaks in the network, thus diminishing device performance. There are two main ways to generate nanoscale features: top-down methods in which the goal is to progressively reduce the dimensions of devices, and bottom-up methods where smaller units are used to assemble larger structures[1]. Lithography has proven to be incredibly useful in patterning surfaces at the nanometer and micron scale[1]. This top-down approach can be used for

generating nanoscale features with remarkable reproducibility[2]. There are two main types of lithography: photolithography and electron-beam lithography.

Photolithography is a technique best suited to patterning large areas of surfaces. It involves spin-coating a light-sensitive polymer resist onto a substrate. The resist is then exposed to light through a mask to chemically alter it wherever the film is exposed. Thus, only areas exposed through the mask are chemically altered. The substrate is then developed using organic solvent that removes the resist, leaving a pattern on the surface which is defined by the mask. There are two types of photoresist: positive and negative. With positive photoresist, the portion exposed to light gets washed away with the resist developer, and with negative photoresist the opposite is the case[3]. Photolithography has remarkable reproducibility, however its main drawback is that the resolution is limited by the wavelength of the light used to alter the resist[4]. At present IBM has been able to use extreme ultraviolet lithography to achieve a 7 nm node however the main drawback though is that this type of lithography causes production costs to increase dramatically[5]. Figure 2.1 represents a diagram of the photolithography process.

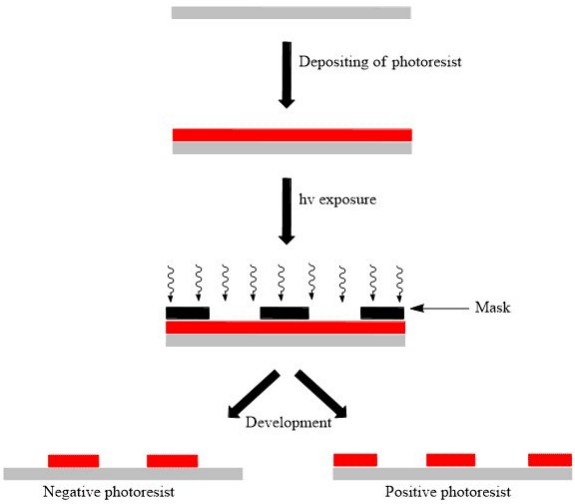

Figure 2.1 The process flow for photolithography.

Electron beam lithography is considered a direct-writing technique. As is the case with photolithography, a polymer layer is first spin-coated on a substrate. A high-energy electron beam is then used to write a pattern on the surface. The areas exposed to the beam are changed chemically. As with photolithography there is positive resist where the exposed parts are washed away with the developer and negative resist where the non-exposed parts are washed away[1]. Figure 2.2 provides a typical process flow for electron beam lithography. Resolutions as low as 2 nm have been achieved with this particular technique[6]. The principle drawback is that because it is a direct writing technique, it is slow, making mass production of high-resolution structures difficult and expensive[1].

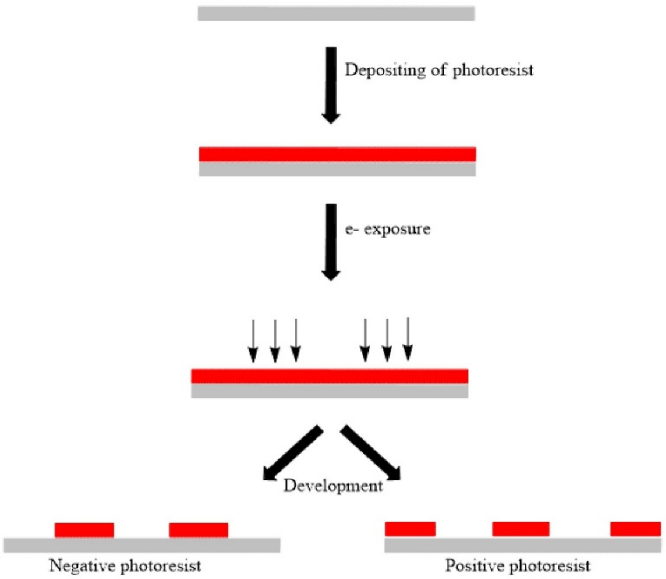

Figure 2.2 Process flow for electron beam lithography

There are also techniques referred to as soft lithography where patterns are printed on a surface using stamps or solutions of a molecule of interest to form an ink[7]. In stamping techniques a pattern is first formed on a substrate using photolithography. This acts as a master so that the pattern can then be formed in a polydimethylsiloxane (PDMS) elastomer making it possible to transfer it to other surfaces[8]. The main issue with this method is that the mechanical

properties of PDMS are only stable down to 500 nm[9]. Another more high-resolution method involves directly writing a pattern using an atomic force microscope tip. In this particular process coined "dip-pen lithography" a solution containing the molecule of interest is deposited on the tip and the pattern is subsequently printed on the substrate. The resolution of dip-pen nanolithography is quite high with sub 100 nm resolution possible however it is incredibly slow thus limiting the throughput[5].

Despite the remarkable achievements made with top-down lithographic techniques, it becomes clear that an alternative is required as the costs associated with the required instrumentation and laboratory facilities are ever rising[10]. Furthermore, in order to achieve very small dimensions the time starts to factor into the equation as the highest resolution techniques tend to have slow throughput[5]. This makes mass production of nanoscale devices impractical from both an economical and experimental standpoint[1]. One proposed alternative is to take a bottom-up approach to fabricate devices featuring nanoarchitectures. This process is known as self-assembly.

Self-assembly is a powerful tool that was popularized by George Whitesides[11]. It draws its inspiration from nature where biomolecules often come together on their own to form highly ordered structures via non-covalent interactions[12]. This is a science of interest in a wide variety of fields. One exciting benefit is that self-assembly allows the development of novel materials with new applications. One such example would be in molecular electronics, where it would be an excellent solution for the nanoparticle assembly problem[13].

The basic definition of self-assembly states that the components of a system such as molecules or nanoparticles form highly ordered structures on their own[14]. The driving force behind this process tends to be interparticle forces, external stimuli or interactions with

templates. Interparticle forces are commonly exploited in self-assembled systems. These interactions tend to be non-covalent in nature[15] and there are a variety of them such as hydrogen bonding, π-π stacking and van der Waals interactions[14]. The strength of these interactions varies significantly. In general stronger interactions are favourable since the final structure will not be easily disturbed while weaker ones offer the advantage of being able to correct defects with minimal energy penalty[15]. There are many examples of self-assembly based on non-covalent interactions[16–18]. Using proper synthetic strategies it is possible to design building blocks of self-assembled systems to be capable of the desired interparticle force[19]. There are a plethora of other strategies though to help drive self-assembly.

External stimuli are also commonly exploited to drive the self-assembly process. These include but are not limited to electric field[20], light[21], temperature[22], and pH[23]. All of these methods are powerful tools in that they provide control over nanoparticle assembly without the need for template molecules[19]. This particular method also provides the advantage that it is incredibly simple to exert control over the assembly process[24]. However, when control over the structure's shape is required there is a more suitable alternative to controlling self-assembly.

In order to achieve a high degree of order in self-assembled systems, a template is often required to bring the system components together[19]. When the process is controlled by a template the structure's shape is defined by it[24]. The template serves to orient and direct the self-assembling components[14]. This allows for the organization of nanomaterials in one dimensional[25], two dimensional[26–29] or even three dimenional[30,31] arrangements. To date a variety of scaffolds have been identified that control the assembly of nanomaterials. They include biomolecules[16,17,32], polymers[33,34] and carbon nanotubes[35,36]. Biomolecules have drawn

significant attention and are an attractive tool for the formation of highly ordered structures for a multitude of reasons.

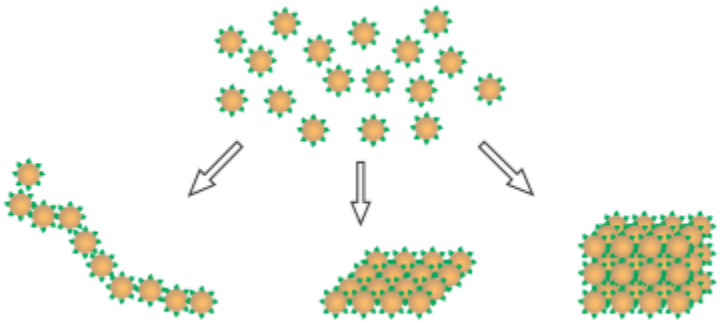

Figure 2.3 Templates offer the advantage of being able to form 1D, 2D and 3D assemblies. Reprinted with permission from Nie, Z. et al., Nature Nanotech., 2010, 5 (1), 15 – 25. Copyright 2010. Nature Publishing Group.

2.3 Using Biological Scaffolds to Control Self-Assembly

Biological scaffolds as a tool to control self-assembly are highly desirable due to their ability to work under mild, aqueous conditions[37]. Furthermore, they allow one to form hierarchical structures by mimicking processes in nature which serves as an excellent model for self-assembly[24]. To date many different biological scaffolds have been shown to control self-assembly to a high degree. These include peptides[25,38], DNA[39,40], proteins[41] and viruses[16,42]. Each offers their own advantages and disadvantages. DNA offers excellent control over structure's architecture on a nanometer scale however it is quite expensive, and for the time being, size control has yet to be achieved over much larger scales[17,19]. The two that are the particular focus of this work are viral scaffolds and peptides. Peptides are relatively simple to work with and commercially available, making them very advantageous. Furthermore, they have been shown to provide excellent control over size and shape of inorganic materials. Viral scaffolds offer the ability to form highly ordered 3-dimensional nanostructures and can easily be

produced in large amounts. The virus work here focuses on the tobacco mosaic virus (TMV), which will be explained in further detail in Section 2.3.2.

2.3.1 Fusion Peptides as Scaffolds for Inorganic Material Synthesis and Assembly

Peptides are an example of a biomaterial that has proved to be a valuable tool in nanotechnology. They consist of a short chain of amino acids whose sequence imparts a certain function on them. A large number of sequences have been identified that can participate in the binding, synthesis and assembly of inorganic materials[43]. To further enhance their function, it is possible to fuse two different peptide domains together creating what is called a fusion peptide that is multifunctional in nature[44]. This could enable the development of hybrid nanomaterials. Many peptide sequences have already been identified for use in the synthesis and binding of metallic nanoparticles[45,46], metal oxides[47,48] and metallic and semiconducting surfaces[49–51]. Furthermore, peptides offer the advantage of being commercially available and relatively simple to work with.

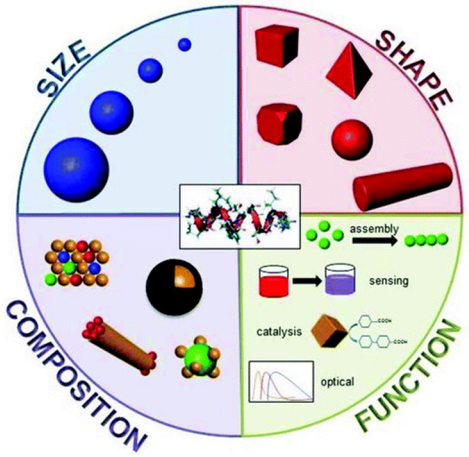

Figure 2.4 Peptides are a material with huge potential in materials science. Reprinted with permission from Briggs, B. et al., J. Phys. Chem. Lett., 2012, 3 (3), 405 – 418. Copyright 2012. American Chemical Society.

Understanding peptides' binding mechanisms to inorganic materials remains a challenge and is largely speculative. The principle challenge hindering advancement in this area is based on the high probability that each peptide has a unique and sequence dependent interaction with its target material making it impossible to make generalizations[52]. Furthermore, there are a large number of variables such as primary structure and secondary structure which are known to affect peptide properties[50,53]. In the case of fusion peptides the order in which each domain is fused together plays a role as well[44]. Despite these limitations they are still a very interesting choice for use in nanomaterial synthesis and binding.

Identifying useful peptide sequences is readily done using phage display techniques (Figure 2.5)[43]. In phage display peptide libraries are constructed from random amino acid sequences on bacteriophages. This enables the selection of peptides with a strong affinity for a given material while also offering the advantage of being able to screen large numbers of potential peptide sequences (~10^6 sequences for any given experiment)[52].

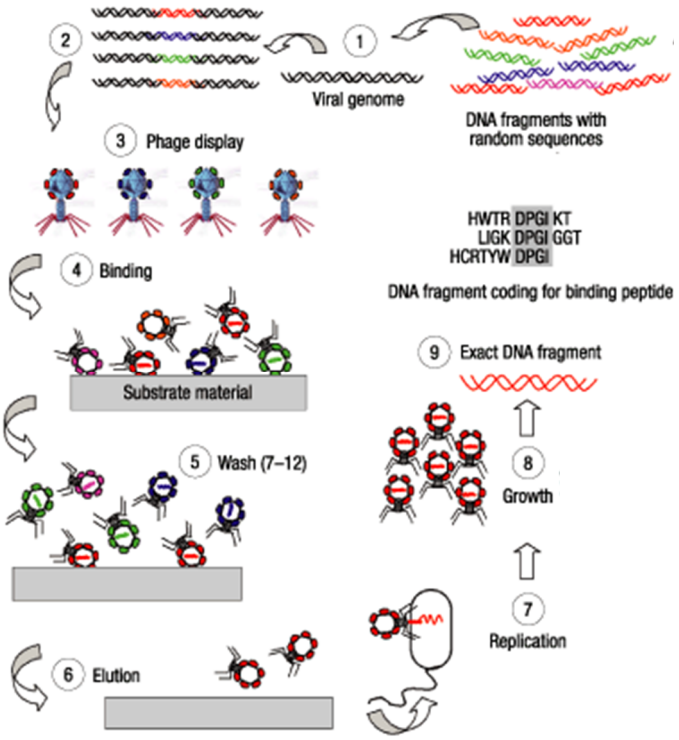

Figure 2.5 Diagram displaying the process for identifying peptide sequences via phage display methods. Reprinted with permission from Sarikaya, M. et al., *Nature Mater.*, **2003**, 2 (9), 577 – 585. Copyright 2003. Nature Publishing Group.

Once a useful sequence has been identified, it can be readily synthesized using modern techniques, since several strategies have been established to make a peptide of choice. In general, the C-terminus (a carboxyl group) is tethered to a solid support such as a polymer bead. The use of a solid resin provides the advantage of being able to readily separate the desired peptide from excess reagents simply by filtration and washing[54]. From there the peptide is synthesized by adding amino acid residues at the N terminus one at a time. Protecting groups are added to the amino acids in solution to keep them from reacting prematurely as the C terminus of the free amino acid is what reacts with the N terminus of the growing peptide chain to form an amide bond. They are removed only once the N terminus is ready for reaction (Figure 2.6)[55]. As some amino acids contain reactive side chains protecting groups are also added to those to prevent unwanted side reactions[54]. After the synthesis, the peptide is cleaved from the support[56].

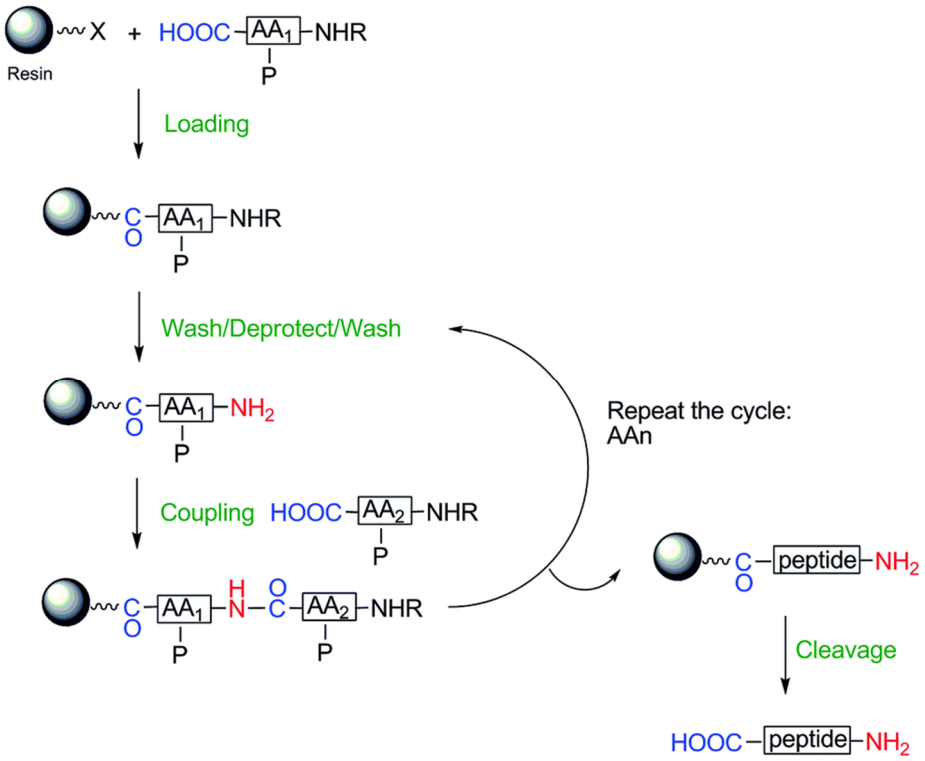

Figure 2.6 General reaction scheme for peptide synthesis. Reprinted with permission from Palomo, J.M., *RSC Adv.*, **2014**, 4, 32 658 - 32672. Copyright 2014. Royal Society of Chemistry.

There are two main protecting groups for the N terminus: tertiary-butyloxycabonyl (Boc) and 9-fluorenylmethoxycarbonyl (Fmoc). The Boc strategy relies on varying acid lability of the Boc group and the protecting groups (generally ether or ester derivatives) that protect reactive side chains to selectively add amino acids at the N-terminus. Trifluoroacetic acid is used to cleave the Boc group, and everything else including the matrix is removed at the end with a strong acid such as hydrofluoric acid[54]. One downside with this synthetic strategy is that harsh acidic conditions are required which some peptide sequences might not survive[56]. The other strategy, which is the Fmoc one, is more frequently employed as it requires milder conditions to cleave the Fmoc group and the other side groups and matrix. The Fmoc is base labile while everything else is acid-labile. Since different protecting groups are removed by different mechanisms, milder reaction conditions can be used. With this particular chemistry side reactions are possible depending on the amino acid being used in the synthesis[54]

The particular area of interest relevant to this work is the use of peptides in gold nanoparticle synthesis and in binding species to silicon dioxide substrates. Gold nanoparticles are of significant interest due to their applications in fields such as molecular electronics[13,57,58] and sensing[59,60]. There are numerous examples of peptides being used to synthesize and stabilize gold nanoparticles[44–46,61]. Understanding the how individual peptides bind to the material, and their role in synthesis is challenging and poorly understood. Peptides are known to adopt multiple conformations when bound to a surface and each different conformation is thought to have slightly different binding energies[62]. Understanding binding energies requires consideration of both enthalpic and entropic effects, and only recent studies have really begun to shed light on the latter[45]. Furthermore individual amino acids and their location in the sequence play a significant role in the binding energy of the peptide[63].

Amino acids like tyrosine, methionine or phenylanaline interact strongly with gold due to the presence of sulfur atoms in their structure or aromatic side groups and as a consequence sequences rich in these amino acids are strong binders[63]. Domains rich in these residues will bind strongly to the surface and have a large enthalpic contribution, however that will reduce the possible number of surface configurations thus diminishing the entropic contribution[62]. On the contrary peptides that lack these strong-binding amino acids will have less of an enthalpic contribution and more of an entropic one due to the increased number of surface configurations[45]. A recent study also discovered that the peptide's concentration plays a significant role in the surface configuration, as at lower concentrations intermolecular interactions, which leads to a variety of conformations, are possible via surface diffusion[64]. At higher concentrations the diffusion which leads to these interactions is not possible hence fewer conformations are formed[64].

Gold binding is an incredibly rapid process. Previous work has demonstrated that the interaction of the peptide and gold surfaces occurs within seconds[65]. This makes them a powerful capping agent in nanoparticle synthesis as they will interact rapidly with reduced Au(0) to form stable nanoparticles with a narrow size distribution[46,66]. Indeed when gold precursor (Au (III)) is incubated with a buffer that has reducing capabilities such as HEPES and a peptide with gold-binding capabilities, AuNP synthesis proceeds readily to form stable dispersions (Figure 2.7)[67,68]. It has been demonstrated with certain gold-binding peptides that a variety of variables influence the rate of reaction and nanoparticle nucleation. These include the concentration of Au(III) and concentration of the reducing agent. Interestingly peptides which can strongly bind gold are thought to inhibit gold nanoparticle growth because they inhibit Au (III) from diffusing to the surface of the nanoparticle and interacting with it to continue increasing nanoparticle size[69].

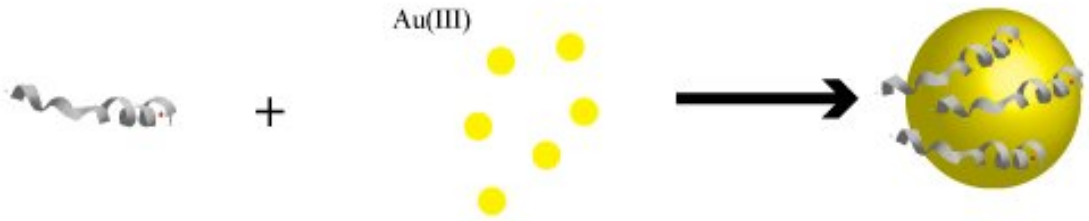

Figure 2.7 Peptides can participate in the reduction of Au(III) to form stable AuNPs.

Another important class of peptides are those that are capable of binding to metal oxides. One important example is peptides with the ability to bind to silicon dioxide surfaces. Numerous studies have identified peptide domains that can bind to these sorts of surfaces[70–72]. As with gold-binding peptides, understanding the peptides' interaction with the silicon dioxide surface is quite tricky[48]. Computational studies have identified sequences rich in hydrophobic amino acids as strong binders to silicon dioxide, however they were unable to identify why these residues

specifically prefer this sort of surface[73]. Furthermore, electrostatic interactions are also known to play a role in the ability of certain peptide domains to bind to silicon dioxide surfaces[74,75]. Understanding the binding process is further complicated by the fact that the surface charge of silicon dioxide varies depending upon pH[75], which may also possibly explain the role of electrostatic interactions[76].

In addition, the peptide's secondary structure when on the silicon dioxide surface is another key factor in identifying sequences that will have strong selectivity for a given material[77]. Theoretical studies have shed some light on possible surface configurations that are energetically favourable, however supporting experimental data is lacking[75,77]. Circular dichroism has provided vital information about the actual conformations that peptides adopt when in solution and when bound to the surface, however such measurements alone do not provide an adsorption mechanism for the peptide[78]. Nuclear magnetic resonance spectroscopy experiments on silicon dioxide nanoparticles have provided some information on peptide structure as well, however they shed little light on the interactions between the peptide and the surface. Furthermore, the results showed some dependence on the nanoparticles' size and shape, making it difficult to extrapolate the data to flat surfaces which are often used with these kinds of peptides[48]. For these reasons it remains unclear as to why certain peptide domains bind strongly to silicon dioxide surfaces and how they bind.

As previously mentioned fusing two different domains together could enable the development of hybrid nanomaterials[44]. To date there are many examples in the literature of two different functional peptide domains being fused together to be used in fields such as sensing[59], catalysis[79] or molecular electronics[80]. One popular example is the binding of gold nanoparticles to silicon dioxide substrates as this would have many exciting applications in fields such as

molecular electronics[81]. Densely packed networks of gold nanoparticles on insulating surfaces would be ideal for integrating conducting molecules into functional devices (Figure 2.8). To date there have been several examples of using peptides to achieve binding of gold nanoparticles to silicon dioxide substrates in the literature[49,80,82]. Fusion peptides make it possible to carry out nanoparticle binding in mild, aqueous conditions and are incredibly simple to use[80]. Many factors affect the properties of fusion peptides including the order in which two domains are fused together[66], secondary structure[83] and so on. The role these parameters play though is poorly understood and more research is needed to rationally develop fusion peptides[32].

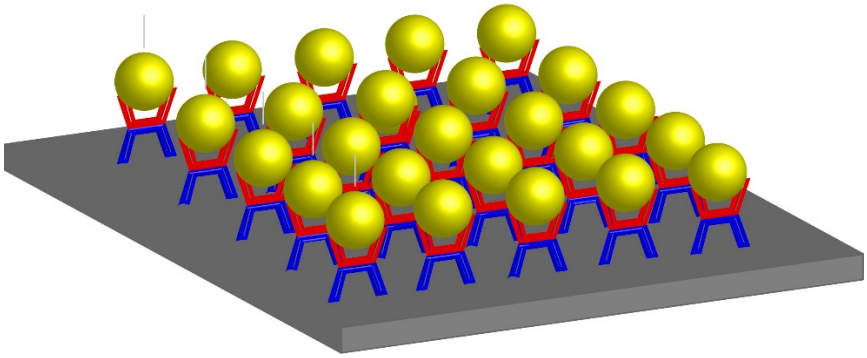

Figure 2.8 One potential application for fusion peptides involves using them to form densely-packed gold nanoparticle networks on surfaces.

2.3.2 Tobacco Mosaic Virus as a Scaffold for Self-Assembly

Achieving complex structures on the nanometer scale remains quite challenging. While lithography and synthetic methods have been used to accomplish this, a simpler and less expensive method remains desirable[84]. Viral scaffolds offer the advantage of being highly monodisperse, relatively low cost and they allow for the formation of three dimensional self-assembled structures[30]. A typical virus consists of a coat protein surrounding its genetic material[84]. The coat protein is a well-defined assembly of multiple subunits and can be readily isolated from the genetic material[85]. Once isolated from their genetic material, some viral coat proteins are capable of forming different assemblies upon changes in parameters like pH and

ionic strength further making them incredibly useful in templating self-assembly[86]. Viruses can easily be modified genetically or chemically so that they can be used as a template for assembling nanomaterials with novel functionalities[87]. Furthermore, since the three dimensional structures of these viruses as determined from X-ray crystallography are good predictors of their solution-phase structures, it becomes possible to gain excellent spatial control over functional motifs[85].

The majority of viruses can be grouped into two main categories with regards to their symmetry: icosahedral and helical symmetry (Figure 2.9). Icosahedral assemblies are named that because they exhibit a structure similar to an icosahedron, which is a 20-sided polyhedron[88]. They exhibit a high volume to surface ratio which in turn does an excellent job of encapsulating the genome[84]. Icosahedral viruses come with a variety of sizes and complexities thus making them versatile tools for self-assembly[89]. To date a number of icosahedral viral coat proteins have been identified as templates for self-assembly including the cowpea mosaic virus[30], cowpea chlorotic mottle virus[90] and the MS2 bacteriophage[91]. Helical assemblies consist of large numbers of the protein subunit wrapped around the virus' genome which in turn gives rise to rod-like structures[86]. Tobacco mosaic virus[92] and MS 13 bacteriophage[93] are two such examples of helical assemblies.

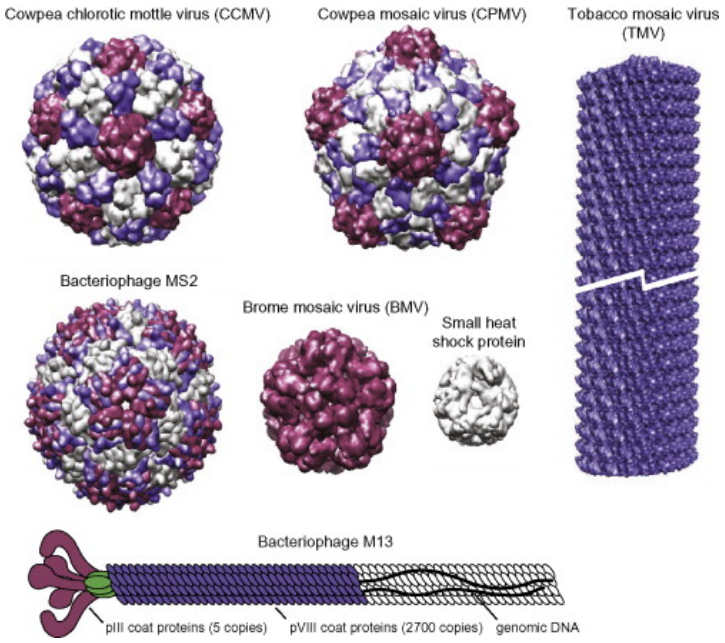

Figure 2.9 Examples of both icosahedral and helical viral coat proteins. Reprinted with permission from Stephanopoulos, N. et al., *Making New Materials from Viral Capsids*, Elsevier B.V., 2012, Vol. 9, 247 - 266. Copyright 2012. Elsevier B. V.

As mentioned in the previous paragraph, one commonly studied virus is the tobacco mosaic virus (TMV). In its native state the tobacco mosaic virus coat protein (TMVcp) forms a rod-like structure around an RNA helix. This structure consists of 2130 subunits of coat protein (Figure 2.10a)[94]. TMV provides the advantage of being stable up to 60 °C and over a pH range of 2 – 9 making it incredibly robust[87]. Another appealing feature of TMVcp is its ability to form various assemblies in the absence of its genome depending on the pH and ionic strength of the solution (Figure 2.10b)[95]. It is important to note that Figure 2.10b is not a true phase diagram in that the boundaries between each different assembly are not phase boundaries. They actually indicate the point at which an assembly becomes detectable and at which point it becomes the predominant one in solution[95]. To date TMV has served as a template for self-assembly of a variety of materials including metallic nanoparticles[16], magnetic nanoparticles[92] and fluorophores[96]. It has also been used for metal ion reduction directly on the surface of the protein[97,98].

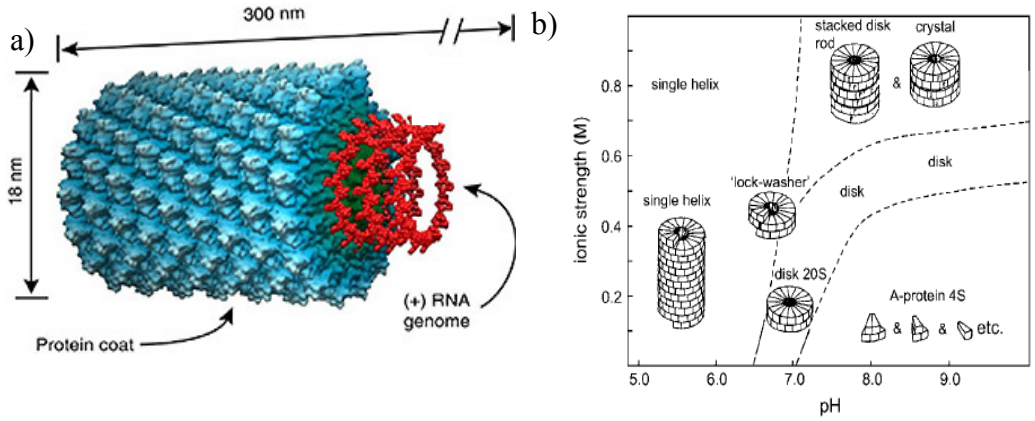

Figure 2.10 a) Tobacco mosaic virus in its native state. b) Phase diagram depicting the various assemblies of the TMVcp depending on the pH and ionic strength. Reprinted with permission from Kegel, W. et al., *J. Biophys.*, **2006**, 91 (4), 1501 – 1512, Copyright 2006. Cell Press.

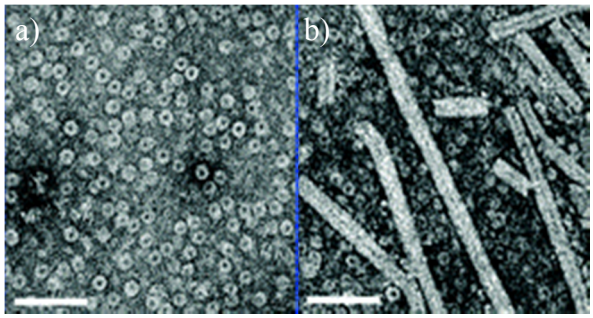

Figure 2.11 TEM micrographs of a) TMV disks and b) TMV rods. Scale bar is 100 nm. Reprinted with permission from Dedeo, M. et al., Nano Lett., 2010, 10 (1), 181 – 186. Copyright 2012. American Chemical Society.

The simplest way to obtain TMVcp is to use *Escherichia coli (E.coli)* bacteria to express the protein. Expression in *E. coli* is highly desirable because *E. coli* has the ability to grow rapidly and at high density. Furthermore, its genetics are well understood which makes it a popular choice for protein expression[99]. A plasmid containing the nucleotide sequence of choice is combined with *E. coli* cells so that the genome of the bacteria is transformed. In order to ensure that only cells that contain the new plasmid are multiplied, a sequence coding for antibiotic resistance is incorporated into the plasmid, and antibiotics are added to growth media[100]. This way only cells that code for the desired protein will grow. Once a desired cell density of transformed cells has been achieved, the cells are induced to get them to produce the

protein of interest[99]. After the cells have produced the desired protein, they are lysed so that the protein can be isolated and purified for usage.

One assembly of particular interest is the 20S disk (Figure 2.12), which is favoured at neutral pH and low ionic strengths. This assembly consists of 34 subunits and two layers, and is 18 nm in diameter with an inner pore of 4 nm[95]. The 20S disk structure is thought to play a vital role in assembly of the virus when it interacts with a specific initiation sequence on the viral RNA that is 1000 units from the 3' end[94]. From this point on the rod grows in a helical-like fashion[101].

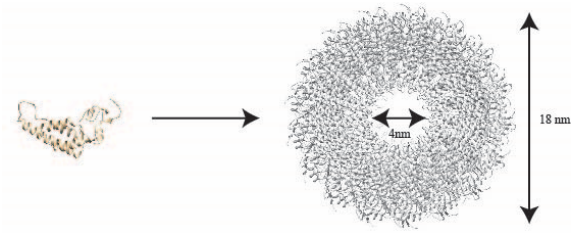

Figure 2.12 The TMVcp disk

TMV assembly is driven by three main factors: 1) hydrophobic interactions, 2) electrostatic interactions and 3) hydrogen bonding[95]. This process is endothermic in nature and as a consequence temperature plays a significant role in driving it[102]. Disk formation is largely the result of hydrophobic interactions which are competing with electrostatic interactions that destabilize the assembly[95]. Increasing the ionic strength of the solution tends to screen these interactions and thus favours the disk assembly[85]. When the pH decreases below the anomalous pKa of 7.2 a larger number of carboxylate groups are protonated thus lowering the number of electrostatic interactions[95]. Lowering the pH further triggers the reversible formation of the chiral lock-washer phase that is helical in nature. This is due to the increase of Caspar pairs which are hydrogen bonding interactions between neighbouring carboxyl groups[103]. The directionality of the hydrogen bond is thought to induce a twist between neighbouring TMVcp

subunits thus leading to the helix formation[95]. The structure of each assembly is summarized in Figure 2.13.

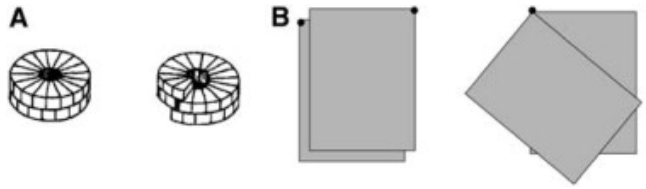

Figure 2.13 a) 20S disk and lock-washer TMVcp assemblies. b) The disk has larger contact area while the lock-washer has a twist in it due to Caspar pairs[95]. Reprinted with permission from Kegel, W. et al., *J. Biophys.*, **2006**, 91 (4), 1501 - 1512. Copyright 2006. Cell Press.

As the N terminus is located on the outer edge of the TMVcp disk it is an ideal target for bioconjugation. This in turn could make it a suitable template for metallic nanoparticle synthesis. Due to the disk's small size dimensions it is likely that if metallic nanoparticles did bind to the exterior of the disk they would be closely spaced together which would make these structures suitable for use in molecular networks.

2.4 Conclusion

One requirement for molecular networks is that the nanoparticles be spaced closely enough so that the molecular wires can bind between two neighbouring ones thus forming a fully functional device. This is quite challenging though as nanoparticles tend to repel each other electrostatically in solution. For this reason a template is needed to control their spacing and binding to insulating substrates. Biomolecules are one such proposed solution. Peptides and TMVcp have showed immense promise for the synthesis and templated self-assembly of inorganic materials and are thought to be useful for forming densely-packed ensembles of gold nanoparticles for use in molecular electronics applications.

2.5 References

(1) Grigorescu, a E.; Hagen, C. W. *Nanotechnology* **2009**, *20* (29), 292001.
(2) Liao, W.-S.; Cheunkar, S.; Cao, H. H.; Bednar, H. R.; Weiss, P. S.; Andrews, A. M. *Science* **2012**, *337* (6101), 1517–1521.
(3) Bandelier, P.; Charley, A.-L.; Lagrange, A. In *Lithography*; Landis, S., Ed.; Wiley, 2010; pp 1–40.
(4) Fourkas, J. T. *J. Phys. Chem. Lett.* **2010**, *1* (8), 1221–1227.
(5) Garcia, R.; Knoll, A. W.; Riedo, E. *Nat. Nanotechnol.* **2014**, *9* (8), 577–587.
(6) Manfrinato, V. R.; Zhang, L.; Su, D.; Duan, H.; Hobbs, R. G.; Stach, E. a.; Berggren, K. K. *Nano Lett.* **2013**, *13* (4), 1555–1558.
(7) Braunschweig, A. B.; Huo, F.; Mirkin, C. a. *Nat. Chem.* **2009**, *1* (5), 353–358.
(8) Delamarche, E.; Donzel, C.; Kamounah, F. S.; Wolf, H.; Geissler, M.; Stutz, R.; Schmidt-Winkel, P.; Michel, B.; Mathieu, H. J.; Schaumburg, K. *Langmuir* **2003**, *19* (21), 8749–8758.
(9) Perl, A.; Reinhoudt, D. N.; Huskens, J. *Adv. Mater.* **2009**, *21* (22), 2257–2268.
(10) Dammel, R. R. *J. Photopolym. Sci. Technol.* **2011**, *24* (1), 33–42.
(11) Whitesides, G. M. *Sci. Am.* **1995**, *273* (September), 146–149.
(12) Whitesides, G. M.; Grzybowski, B. *Science (80-.).* **2002**, *295* (5564), 2418–2421.
(13) Conklin, D.; Nanayakkara, S.; Park, T.-H.; Lagadec, M. F.; Stecher, J. T.; Chen, X.; Therien, M. J.; Bonnell, D. a. *ACS Nano* **2013**, *7* (5), 4479–4486.
(14) Grzybowski, B. a.; Wilmer, C. E.; Kim, J.; Browne, K. P.; Bishop, K. J. M. *Soft Matter* **2009**, *5* (6), 1110.
(15) Philp, D.; Stoddart, J. F. *Angew. Chem. Ed. Engl.* **1996**, *35*, 1154–1196.
(16) Zahr, O. K.; Blum, A. S. *Nano Lett.* **2012**, *12* (2), 629–633.
(17) Wang, R.; Nuckolls, C.; Wind, S. J. *Angew. Chem. Int. Ed. Engl.* **2012**, *51* (45), 11325–11327.
(18) Wang, W.; Yu, L. *Langmuir* **2011**, *27* (6), 2084–2087.
(19) Grzelczak, M.; Vermant, J.; Furst, E. M.; Liz-marza, L. M. *ACS Nano* **2010**, *4* (7), 3591–3605.
(20) Chen, Y.; Cruz-Chu, E. R.; Woodard, J. C.; Gartia, M. R.; Schulten, K.; Liu, L. *ACS Nano* **2012**, *6* (10), 8847–8856.
(21) Shiraishi, Y.; Tanaka, K.; Shirakawa, E.; Sugano, Y.; Ichikawa, S.; Tanaka, S.; Hirai, T. *Angew. Chemie - Int. Ed.* **2013**, *52* (32), 8304–8308.
(22) Yu, Z.-Q.; Sun, J.-T.; Pan, C.-Y.; Hong, C.-Y. *Chem. Commun.* **2012**, *48* (45), 5623.
(23) Ghosh, A.; Dobson, E. T.; Buettner, C. J.; Nicholl, M. J.; Goldberger, J. E. **2014**.
(24) Nie, Z.; Petukhova, A.; Kumacheva, E. *Nat. Nanotechnol.* **2010**, *5* (1), 15–25.
(25) Chen, C.-L.; Rosi, N. L. *J. Am. Chem. Soc.* **2010**, *132* (20), 6902–6903.
(26) Nonoyama, T.; Tanaka, M.; Inai, Y.; Higuchi, M.; Kinoshita, T. *ACS Nano* **2011**, *5* (8), 6174–6183.
(27) Wang, Y.; Duan, C.; Peng, L.; Liao, J. *Sci. Rep.* **2014**, 1–6.
(28) Guédon, C. M.; Zonneveld, J.; Valkenier, H.; Hummelen, J. C.; van der Molen, S. J. *Nanotechnology* **2011**, *22* (12), 125205.
(29) Maune, H. T.; Han, S.-P.; Barish, R. D.; Bockrath, M.; Iii, W. a G.; Rothemund, P. W. K.; Winfree, E. *Nat. Nanotechnol.* **2010**, *5* (1), 61–66.
(30) Fontana, J.; Dressick, W. J.; Phelps, J.; Johnson, J. E.; Rendell, R. W.; Sampson, T.;

Ratna, B. R.; Soto, C. M. *Small* **2014**, 1–6.
(31) Blum, A. S.; Soto, C. M.; Sapsford, K. E.; Wilson, C. D.; Moore, M. H.; Ratna, B. R. *Biosens. Bioelectron.* **2011**, *26* (6), 2852–2857.
(32) Seker, U. O. S.; Sharma, V. K.; Akhavan, S.; Demir, H. V. *Langmuir* **2014**, *30* (8), 2137–2143.
(33) Said-Mohamed, C.; Niskanen, J.; Karesoja, M.; Pulkkinen, P.; Tenhu, H.; Daoud, M.; Lee, L.-T. *Soft Matter* **2011**, *7* (15), 7112.
(34) Wang, H.; Chen, L.; Shen, X.; Zhu, L.; He, J.; Chen, H. *Angew. Chem. Int. Ed. Engl.* **2012**, *51* (32), 8021–8025.
(35) Ko, J. W.; Woo, J.-M.; Jinhong, A.; Cheon, J. H.; Lim, J. H.; Kim, S. H.; Chun, H.; Kim, E.; Park, Y. J. *ACS Nano* **2011**, *5* (6), 4365–4372.
(36) Zhou, C.; Wang, S.; Sun, J.; Wei, N.; Yang, L.; Zhang, Z.; Liao, J.; Peng, L.-M. *Appl. Phys. Lett.* **2013**, *102* (10), 103102.
(37) Sarikaya, M.; Tamerler, C.; Jen, A. *Nat. Mater.* **2003**, *2* (9), 577–585.
(38) Slocik, J. M.; Tam, F.; Halas, N. J.; Naik, R. R. *Nano Lett.* **2007**, *7* (4), 1054–1058.
(39) Endo, M.; Yang, Y.; Emura, T.; Hidaka, K.; Sugiyama, H. *Chem. Commun. (Camb).* **2011**, *47* (38), 10743–10745.
(40) Han, S.; Maune, H. T.; Barish, R. D.; Bockrath, M.; Goddard, W. a. *Nano Lett.* **2012**, *12* (3), 1129–1135.
(41) Slocik, J. M.; Naik, R. R.; Stone, M. O.; Wright, D. W. *J. Mater. Chem.* **2005**, *15* (7), 749.
(42) Blum, A. S.; Soto, C. M.; Wilson, C. D.; Cole, J. D.; Kim, M.; Gnade, B.; Chatterji, A.; Ochoa, W. F.; Lin, T.; Johnson, J. E.; others. *Nano Lett.* **2004**, *4* (5), 867–870.
(43) Briggs, B. D.; Knecht, M. R. *J. Phys. Chem. Lett.* **2012**, *3* (3), 405–418.
(44) Slocik, J. M.; Naik, R. R. *Adv. Mater.* **2006**, *18* (15), 1988–1992.
(45) Li, Y.; Tang, Z.; Prasad, P. N.; Knecht, M. R.; Swihart, M. T. *Nanoscale* **2014**, *6* (6), 3165–3172.
(46) Serizawa, T.; Hirai, Y.; Aizawa, M. *Langmuir* **2009**, *25* (20), 12229–12234.
(47) Eteshola, E.; Brillson, L. J.; Lee, S. C. *Biomol. Eng.* **2005**, *22* (5-6), 201–204.
(48) Mirau, P. a; Naik, R. R.; Gehring, P. *J. Am. Chem. Soc.* **2011**, *133* (45), 18243–18248.
(49) Hnilova, M.; Khatayevich, D.; Carlson, A.; Oren, E. E.; Gresswell, C.; Zheng, S.; Ohuchi, F.; Sarikaya, M.; Tamerler, C. *J. Colloid Interface Sci.* **2011**, *365* (1), 97–102.
(50) Katoch, J.; Kim, S. N.; Kuang, Z.; Farmer, B. L.; Naik, R. R.; Tatulian, S. a; Ishigami, M. *Nano Lett.* **2012**, *12* (5), 2342–2346.
(51) Mao, X.; Guo, Y.; Luo, Y.; Niu, L.; Liu, L.; Ma, X.; Wang, H.; Yang, Y.; Wei, G.; Wang, C. *J. Am. Chem. Soc.* **2013**, *135* (6), 2181–2187.
(52) Slocik, J. M.; Naik, R. R. *Chem. Soc. Rev.* **2010**, *39* (9), 3454–3463.
(53) Coppage, R.; Slocik, J. M.; Briggs, B. D.; Frenkel, A. I.; Naik, R. R.; Knecht, M. R. *ACS Nano* **2012**, *6* (2), 1625–1636.
(54) Amblard, M.; Fehrentz, J.-A.; Martinez, J.; Subra, G. In *Methods in Molecular Biology*; Howl, J., Ed.; Springer: Totowa, NJ, 2005; Vol. 298, pp 209–223.
(55) Palomo, J. M. *RSC Adv.* **2014**, *4*, 32658–32672.
(56) Cudic, M.; Fields, G. B. In *Molecular Biomethods Handbook*; Walker, J. M., Rapley, R., Eds.; Humana Press: Totowa, NJ, 2008; pp 515–546.
(57) Conklin, D.; Nanayakkara, S.; Park, T.-H.; Lagadec, M. F.; Stecher, J. T.; Therien, M. J.; Bonnell, D. a. *Nano Lett.* **2012**, *12* (5), 2414–2419.
(58) Mangold, M. a; Calame, M.; Mayor, M.; Holleitner, A. W. *J. Am. Chem. Soc.* **2011**, *133*

(31), 12185–12191.
(59) Aili, D.; Selegård, R.; Baltzer, L.; Enander, K.; Liedberg, B. *Small* **2009**, *5* (21), 2445–2452.
(60) Yu, Y.; Cao, Q.; Zhou, M.; Cui, H. *Biosens. Bioelectron.* **2013**, *43*, 137–142.
(61) Lévy, R.; Thanh, N. T. K.; Doty, R. C.; Hussain, I.; Nichols, R. J.; Schiffrin, D. J.; Brust, M.; Fernig, D. G. *J. Am. Chem. Soc.* **2004**, *126* (32), 10076–10084.
(62) Tang, Z.; Palafox-Hernandez, J. P.; Law, W.-C.; E Hughes, Z.; Swihart, M. T.; Prasad, P. N.; Knecht, M. R.; Walsh, T. R. *ACS Nano* **2013**, No. Xx.
(63) Yu, J.; Becker, M. L.; Carri, G. a. *Langmuir* **2012**, *28* (2), 1408–1417.
(64) Nergiz, S. Z.; Slocik, J. M.; Naik, R. R.; Singamaneni, S. *Phys. Chem. Chem. Phys.* **2013**, *15* (28), 11629–11633.
(65) Hnilova, M.; Karaca, B. T.; Park, J.; Jia, C.; Wilson, B. R.; Sarikaya, M.; Tamerler, C. *Biotechnol. Bioeng.* **2012**, *109* (5), 1120–1130.
(66) Slocik, J. M.; Stone, M. O.; Naik, R. R. *Small* **2005**, *1* (11), 1048–1052.
(67) Song, C.; Blaber, M. G.; Zhao, G.; Zhang, P.; Fry, H. C.; Schatz, G. C.; Rosi, N. L. *Nano Lett.* **2013**, *13* (7), 3256–3261.
(68) Diamanti, S.; Elsen, A.; Naik, R.; Vaia, R. *J. Phys. Chem. C* **2009**, *113* (23), 9993–9997.
(69) Stanley, S. K.; Becker, M. L.; Lin, E. K.; Wu, W. L. *Langmuir* **2009**, *25* (18), 10886–10892.
(70) Kacar, T.; Ray, J.; Gungormus, M.; Oren, E. E.; Tamerler, C.; Sarikaya, M. *Adv. Mater.* **2009**, *21* (3), 295–299.
(71) Puddu, V.; Perry, C. C. *ACS Nano* **2012**, *6* (7), 6356–6363.
(72) Seker, U. O. S.; Demir, H. V. *Molecules* **2011**, *16* (2), 1426–1451.
(73) Oren, E. E.; Tamerler, C.; Sahin, D.; Hnilova, M.; Seker, U. O. S.; Sarikaya, M.; Samudrala, R. *Bioinformatics* **2007**, *23* (21), 2816–2822.
(74) Chen, H.; Su, X.; Neoh, K.-G.; Choe, W.-S. *Langmuir* **2009**, *25* (3), 1588–1593.
(75) Wright, L. B.; Walsh, T. R. *J. Phys. Chem. C* **2012**, *116* (4), 2933–2945.
(76) Vallee, A.; Humblot, V.; Pradier, C.-M. *Acc. Chem. Res.* **2010**, *43* (10), 1297–1306.
(77) Wright, L. B.; Walsh, T. R. *Phys. Chem. Chem. Phys.* **2013**, *15* (13), 4715–4726.
(78) Fears, K. P.; Petrovykh, D. Y.; Photiadis, S. J.; Clark, T. D. *Langmuir* **2013**, *29* (32), 10095–10101.
(79) SLOCIK, J. M.; GOVOROV, A. O.; NAIK, R. R. *Supramol. Chem.* **2006**, *18* (5), 415–421.
(80) Del Re, J.; Blum, A. S. *Appl. Surf. Sci.* **2014**, *296*, 24–30.
(81) Del Re, J.; Moore, M. H.; Ratna, B. R.; Blum, A. S. *Phys. Chem. Chem. Phys.* **2013**, *15* (21), 8318–8323.
(82) Nochomovitz, R.; Amit, M.; Matmor, M.; Ashkenasy, N. *Nanotechnology* **2010**, *21* (14), 145305.
(83) Slocik, J. M.; Govorov, A. O.; Naik, R. R. *Nano Lett.* **2011**, *11* (2), 701–705.
(84) Dedeo, M. T.; Finley, D. T.; Francis, M. B. *Viral capsids as self-assembling templates for new materials*, 1st ed.; Elsevier Inc., 2011; Vol. 103.
(85) Liu, Z.; Qiao, J.; Niu, Z.; Wang, Q. *Chem. Soc. Rev.* **2012**, *41* (18), 6178.
(86) Stephanopoulos, N.; Francis, M. B. In *Polymer Science: A Comprehensive Reference, 10 Volume Set*; Elsevier B.V., 2012; Vol. 9, pp 247–266.
(87) Brown, A. D.; Naves, L.; Wang, X.; Ghodssi, R.; Culver, J. N. *Biomacromolecules* **2013**, *14* (9), 3123–3129.

(88) Bergkvist, M.; Cohen, B. A. *The Nanobiotechnology Handbook*; Xie, Y., Ed.; CRC Press, 2012.
(89) Nguyen, H. D.; Reddy, V. S.; Brooks, C. L. *J. Am. Chem. Soc.* **2009**, *131* (7), 2606–2614.
(90) Mikkilä, J.; Eskelinen, A. P.; Niemelä, E. H.; Linko, V.; Frilander, M. J.; Törmä, P.; Kostiainen, M. a. *Nano Lett.* **2014**, *14* (4), 2196–2200.
(91) Capehart, S. L.; Coyle, M. P.; Glasgow, J. E.; Francis, M. B. *J. Am. Chem. Soc.* **2013**, *135* (8), 3011–3016.
(92) Khan, A. a; Fox, E. K.; Górzny, M. Ł.; Nikulina, E.; Brougham, D. F.; Wege, C.; Bittner, A. M. *Langmuir* **2013**, *29* (7), 2094–2098.
(93) Moradi, M.; Li, Z.; Qi, J.; Xing, W.; Xiang, K.; Chiang, Y.-M.; Belcher, A. M. *Nano Lett.* **2015**, 150406094951004.
(94) Klug, a. *Philos. Trans. R. Soc. Lond. B. Biol. Sci.* **1999**, *354* (1383), 531–535.
(95) Kegel, W. K.; van der Schoot, P. *Biophys. J.* **2006**, *91* (4), 1501–1512.
(96) Miller, R. a; Stephanopoulos, N.; McFarland, J. M.; Rosko, A. S.; Geissler, P. L.; Francis, M. B. *J. Am. Chem. Soc.* **2010**, *132* (17), 6068–6074.
(97) Shah, S. N.; Shah, S. S.; Ito, E.; Heddle, J. G. *RSC Adv.* **2014**, *4* (74), 39305.
(98) Liu, Y.; Zhang, W.; Zhu, Y.; Luo, Y.; Xu, Y.; Brown, A.; Culver, J. N.; Lundgren, C. a.; Xu, K.; Wang, Y.; Wang, C. *Nano Lett.* **2013**, *13* (1), 293–300.
(99) Baneyx, F. *Curr. Opin. Biotechnol.* **1999**, *10* (5), 411–421.
(100) Bernhard, F.; Klammt, C.; Ruterjans, H. In *Reference Module in Chemistry, Molecular Sciences and Chemical Engineering Comprehensive Medicinal Chemistry II*; Taylor, J. ., Triggle, D. B., Eds.; Elsevier Ltd, 2007; Vol. 107 - 128, pp 1–2.
(101) Butler, P.J.G., Finch, J.T., Zimmern, D. *Nature* **1977**, *265* (5591), 217–219.
(102) Sturtevant, J. M.; Velicelebi, G.; Jaenicke, R.; Lauffer, M. a. *Biochemistry* **1981**, *20* (13), 3792–3800.
(103) Bruckman, M. a; Soto, C. M.; Mcdowell, H.; Liu, J. L.; Ratna, B. R.; Korpany, K. V; Zahr, O. K.; Blum, A. S. *ACS Nano* **2011**, No. 3, 1–8.

3. Modulating the Conduction of Oligophenylene Vinylene through Intramolecular Interactions

The following chapter is adapted from 'Molecular Sensing: Modulating Molecular Conduction Through Intermolecular Interactions', Julia Del Re, Martin H. Moore, Banahalli R. Ratna and Amy Szuchmacher Blum, Phys. Chem. Chem. Phys., 15, 8318 (2013).

3.1 Preface

In this particular work, we study the influence of the local environment on the conduction of oligophenylene vinylene (OPV) to determine whether or not it would be useful for sensing applications. The particular OPV analog studied has an electron-donating tert-butoxy group on the central aromatic ring. We therefore hypothesize that these groups would make OPV capable of undergoing π-π stacking interactions with aromatic analytes containing electron-withdrawing groups. Electrical experiments confirm that the conduction of OPV decreases upon exposure to nitroaromatic analytes while analytes containing electron-donating groups have no effect. The results were also correlated with fluorescence experiments where nitroaromatic analytes were found to quench the fluorescence intensity of OPV. This indicates that the observed changes in conduction are likely a result of π donor-acceptor interactions.

3.2 Introduction

Molecular electronics has attracted a significant amount of interest ever since Aviram and Ratner's revolutionary paper launched the field[1]. Using molecules in circuits offers several key advantages such as high device densities, the ability to synthesize a large number of transistors simultaneously and the integration of new functionalities into electronic devices[2]. One application of the utility of such new functionality is in chemical sensing. Previous work has demonstrated that the conduction of single molecules is incredibly sensitive to its local

environment[3,4]. This property makes them a desirable candidate for novel sensing devices. Using molecular wires would also provide the added advantage of excellent detection limits[5].

As detailed in Chapter 1 nitroaromatic compounds are frequently studied in sensing research because of their toxicity, environmental effects and frequent use in explosives[6]. Ideally a suitable sensor is cost-effective and sensitive[7]. While fluorescence-based sensing has proven to be rapid and sensitive[8–11], they are susceptible to detrimental effects such as photobleaching and photodegradation[12]. One alternative that has not been well-explored though is the use of molecular wire-based sensors, which are expected to be sensitive, selective and capable of rapid detection[5]. In principle, it should also be possible to construct a molecular electronic device that is high density owing to the size of a molecular wire. Furthermore, the cost of device fabrication is expected to be low[13]. Molecular recognition studies have already looked at the potential use of molecular electronics for detecting species such as biomolecules[14,15] or metal ions[16], however there has been limited work on their use in detecting nitroaromatic compounds[5].

The particular molecular wire candidate studied in this work is oligophenylene vinylene (OPV). OPV has several important properties that make it a desirable conductor including its rigid planar structure, low degree of bond-length alteration and small HOMO-LUMO gap[17–19]. The particular OPV analog studied in this work (Scheme 3.1) contains electron-donating tert-butoxy groups around the central aromatic ring. The presence of these groups would likely mean that OPV could potentially form π donor-acceptor interactions with aromatic molecules containing electron-withdrawing groups which in turn could be detected by a change in conduction.

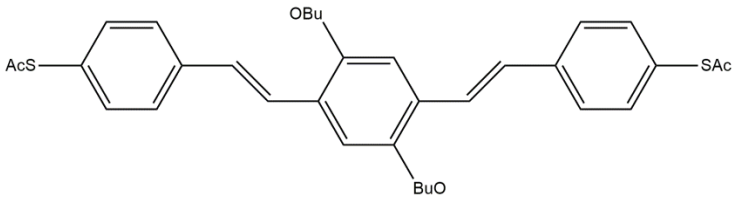

1

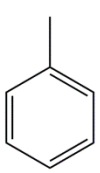

2

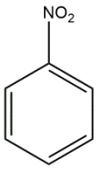

3

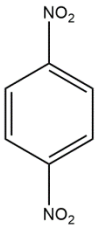

4

Scheme 3.1 The conductance of **1** was measured to see how interactions with **2**, **3** or **4** would affect it.

In this chapter we examine the effect of nitroaromatic analytes on the conduction properties of **1**. Nitro groups are electron-withdrawing in nature and it is therefore expected that they will cause a measurable decrease in the conduction of **1**. To confirm this we used nitrobenzene (**3**) and 1,4-dinitrobenzene as our nitroaromatic analytes (**4**). To confirm that any changes in conduction are coming from a π donor-acceptor interaction we also used an analyte that contains electron-donating groups (**2**). It is expected that **2** will cause no change in the conduction of **1**. We further correlated results of electrical measurements with solution-phase fluorescence experiments where we tested the effect of each analyte studied on the fluorescence intensity of **1**. It is well known that fluorescence quenching can be caused by π donor-acceptor interactions, therefore fluorescence experiments would confirm that any observed changes in conduction would likely be linked to the same effect, thus providing a greater understanding of the system.

3.3 Experimental

3.3.1 Chemicals and Materials

All compounds were purchased from Sigma Aldrich (Ontario, Canada) unless otherwise specified. 5 nm gold colloids and gold (111) on mica were purchased from SPI Supplies (Westchester, PA). OPV was synthesized according to procedures described elsewhere[18].

3.3.2 Fluorescence Measurements

A solution of OPV was made by dissolving 1 mg of OPV in 10 ml of THF and diluting the solution by a factor of 0.1 for fluorescence measurements. A UV/VIS spectrum was collected to determine the optimal excitation wavelength. The solution was then spiked with pre-determined amounts of analytes (toluene, nitrobenzene or 1,4-dinitrobenzene) and left to sit for half an hour before collecting the absorbance and fluorescence spectra at a constant temperature of 23 ˚C. Absorbance spectra were collected with a Cary 100 Bio UV/VIS spectrophotometer (Agilent, Missisauga, ON) equipped with a Cary Dual Cell Peltier Accessory (Agilent, Missisauga, ON). Fluorescence spectra were collected with a Cary Eclipse fluorimeter (Agilent, Missisauga, ON) equipped with a Cary Single Cell Peltier Accessory (Agilent, Missisauga, ON). All measurements were performed in quartz cuvettes with a pathlength of 1 cm (Spectrocell, Oreland, PA).

3.3.3 Self-Assembled Monolayer Preparation

Gold (111) on mica was immersed in a solution of 1 mM 1-decanethiol in ethanol for 18 hours, after which it was removed and washed with ethanol to form a C10 self-assembled monolayer (SAM). 1 mg of acetyl-protected OPV was dissolved in 4 ml of anhydrous THF in an inert atmosphere. 20 µL of concentrated ammonium hydroxide was added, followed by excess amount of analyte (**2**, **3**, **4**) of which the amounts are listed in Table 3.1. The solution was left to

sit for 15 minutes after which the C10 SAM was immersed in it for an hour. Upon removal from the OPV solution, the SAM was washed with THF and ethanol. It was then immersed in a solution of 5 nm colloidal gold nanoparticles used as received for 3 hours, after which it was washed with deionized water and dried with a gentle stream of nitrogen gas. Figure 3.1 represents a scheme of the experimental procedure followed.

Table 3.1. Quantities of Analyte Added to OPV Solution Prior to Insertion into the SAM

Analyte	Ratio Analyte to OPV	Moles of analyte (mol)	Mass Added (mg)
2	3	$5*10^{-6}$	0.5
3	3	$5*10^{-6}$	0.6
4	3	$5*10^{-6}$	0.9

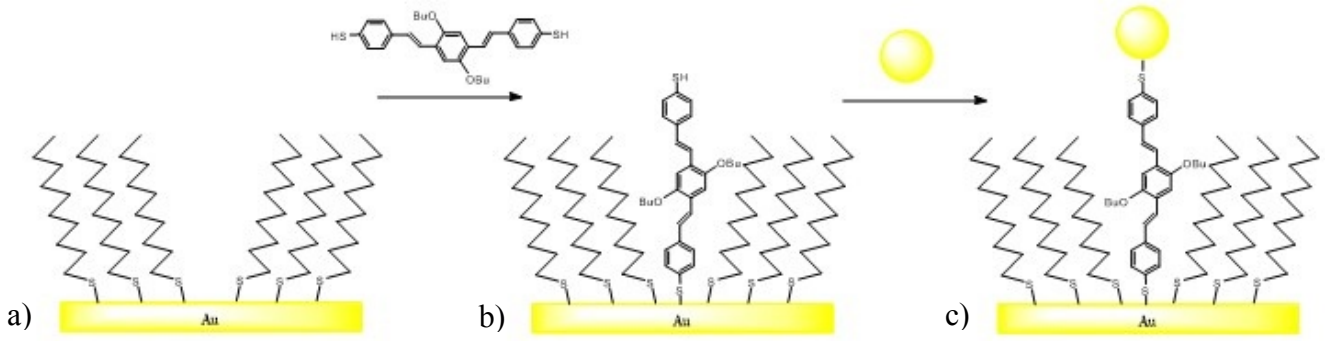

Figure 3.1 Schematic showing the formation of samples used for STM conduction measurements. a) C10 thiol self-assembled monolayer on the gold on mica substrate. b) OPV dithiol molecules insert into defects in the C10 SAM. c) Gold nanoparticles bind to the exposed thiol on inserted OPV dithiol molecules, creating targets for measurement.

3.3.4 Conductance Measurements

The SAMs were characterized by scanning tunnelling microscopy using an Asylum Research Scanning Probe Microscope (Asylum Research, Santa Barbara, CA). STM tips were freshly cut from platinum iridium wire (80 % platinum, 20 % iridium) 0.25 mm in diameter (Nanoscience Instruments, Phoenix, AZ) before each experiment.

3.4 Results

Prior to obtaining fluorescence measurements, a UV/VIS spectrum was collected for a solution of **1** in THF (Figure 3.2). Examination of Figure 3.2 reveals a strong absorbance at 405 nm. As this was the wavelength at which the maximum absorption occurred, this was used as the excitation wavelength for subsequent experiments.

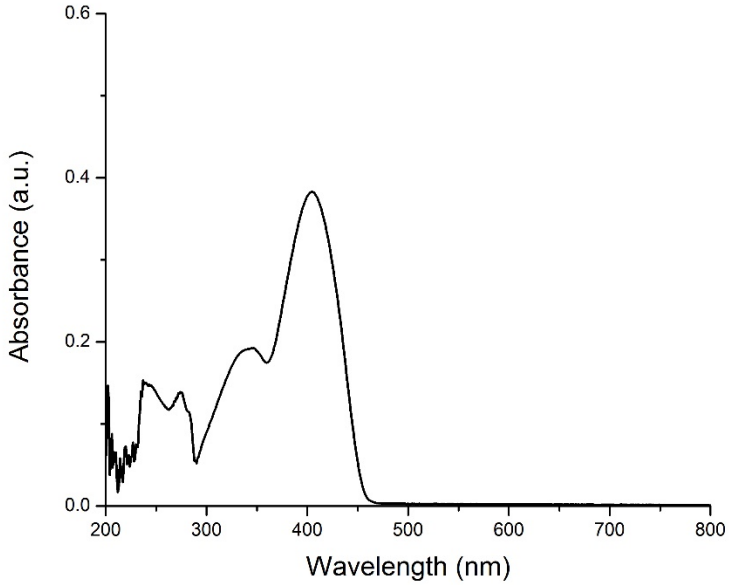

Figure 3.2 UV/VIS spectrum of OPV.

Fluorescence measurements performed to see if the analytes being studied would cause quenching of **1** (Figure 3.3). An emission peak was observed at 455 nm and its intensity was observed as a function of analyte concentration to see if any quenching would be observed (Figure 3.3). It is well known that electron-deficient analytes such as nitroaromatic molecules quench a molecule's fluorescence intensity through π donor-acceptor interactions. Therefore if these same analytes cause a drop in the conductance of OPV it may likely be due to the same type of non-covalent interactions.

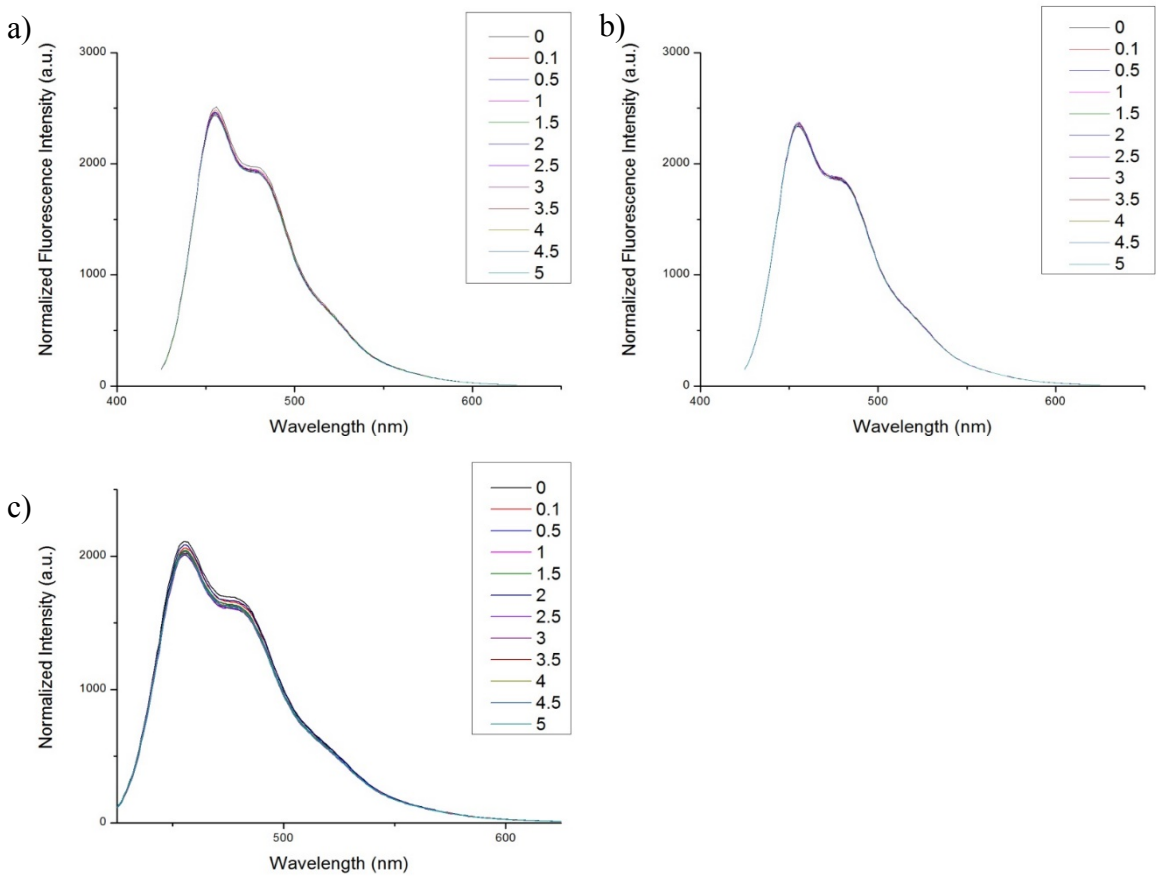

Figure 3.3 Fluorescence spectra for 1 exposed to increasing amounts of a) **2**, b) **3** and d) **4**. The legend denotes the molecular ratio of analyte to **1**.

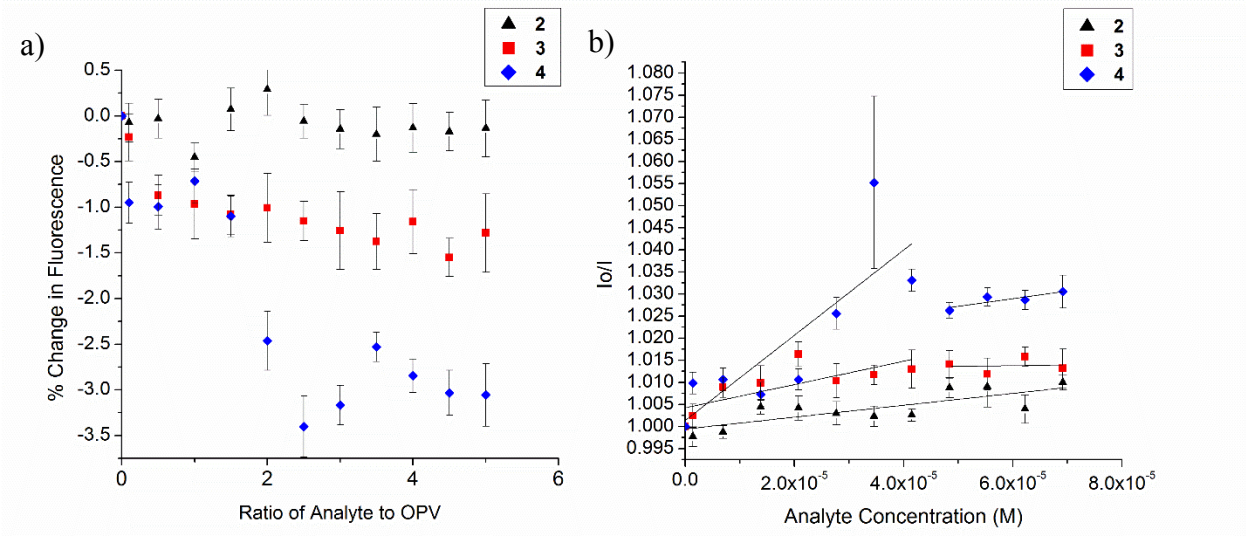

Figure 3.4 a) Plot showing the effect of analyte amount on the fluorescence of OPV and b) Stern-Volmer plots for each analyte. The concentration of OPV was 14 μM in all cases.

Examination of Figure 3.3 reveals that upon exposure to nitroaromatic targets, the fluorescence intensity of OPV drops. Furthermore, the larger the number of electron-withdrawing nitro groups, the greater the quenching effect, as was evidenced when **4** had a greater effect than **3**. Analyte **2** on the other hand had only a minimal effect, which is expected due to the presence of the electron-donating methyl group. Figure 3.4a displays the percent quenching observed which was determined by calculating the signal observed relative to that of solutions of OPV of identical concentration and no analyte. In all cases, the quenching effect seems to plateau at a ratio of 3 analyte molecules to one OPV molecule. This suggests that at this particular ratio, all binding sites are saturated and no further interactions of **1** with the analyte are possible. Examination of the Stern-Volmer plots (Figure 3.4b) also shows this same trend, and confirms a static quenching model for analytes **3** and **4** with K_{sv} with a saturation point of around 40 μM in both cases. Analyte **2** on the other hand is best fit with a collisional quenching model with a K_{sv} of 130 ± 70.

Having determined that the analytes under investigation can cause fluorescence quenching via π donor-acceptor interactions, they were then studied for their effect on the conductivity of OPV. Self-assembled monolayers were characterized using scanning tunnelling microscopy (STM). For this study 5 nm gold nanoparticles were used to complete the junction, since previous work by Morita et al. has demonstrated that this particular size does not seem to cause distortions of the current-voltage curves due to Coulomb blockade[20]. Molecular junctions appeared as bright protusions in the insulating C10 layer (Figure 3.5). They most commonly were found around gold vacancy islands. Once identified, the STM tip was positioned over these junctions and I-V curves were collected by sweeping the tip voltage from -0.5 V to 0.5 V.

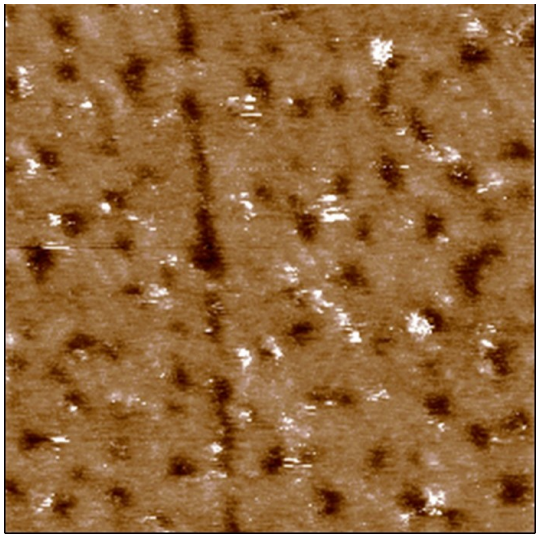

Figure 3.5 A 55 x 55 nm^2 image of a C10/1 monolayer where 4 is the analyte. V_{bias} = 500 mV, I = 1 nA

OPV is known to be a hole conductor, which mean that conduction occurs through the highest occupied molecular orbital (HOMO)[21]. Therefore, non-covalent interactions that shift electron density away from the HOMO and decrease its alignment with the electrode's Fermi level are expected to diminish the conduction of **1** while molecules which do not are expected to cause no measurable effect. In order to test this hypothesis we examined the effect that nitroaromatic analytes, which are electron with-drawing in nature, had on the conduction of OPV by collecting the I-V curves. It is expected that these sorts of analytes will withdraw electron density away from the molecule thus causing a drop in conduction.

Mean I-V curves were collected for OPV and OPV interaction with all the analytes studied (Figure 3.6). In all cases, an excess amount of analyte was used such that the ratio of analyte was 3 to 1. This was determined to be the ratio at which the effect the analyte has on fluorescence intensity plateaued which was likely an indication of saturation of binding sites. The resistances were determined by taking the slope of these curves in the Ohmic region (-0.1 V to 0.1 V) (Table 3.2). Approximately 100 I-V curves were collected for the final data analysis.

To ensure reproducible measurements of the same junction, 5 to 10 I-V curves were collected for each junction. The STM tip was in all likelihood in contact with the gold nanoparticle as has been in other experiments with similar molecules[22]. This was determined from tip-height displacement, which indicates that the tip did not retract far enough to avoid collision with the nanoparticle. Furthermore, according to Fan et al. only noise is observed in the I-V curves when the tip and sample are not in contact[23]. The resistance of OPV was in good agreement with previously published literature values (Table 3.2)[22]. Interaction of OPV with **2** seems to have no significant effect on the conductance of the molecule which is expected given that it is an electron-rich analyte. However, upon addition of nitroaromatic analyte the conductivity decreases. This is most evident for the case of **4** which has two nitro groups on it indicating that the greater the degree of nitroaromatic substitution the greater the effect on conductivity. To further look at what was going on histograms of the individual measured resistances were constructed for each junction (Figure 3.7).

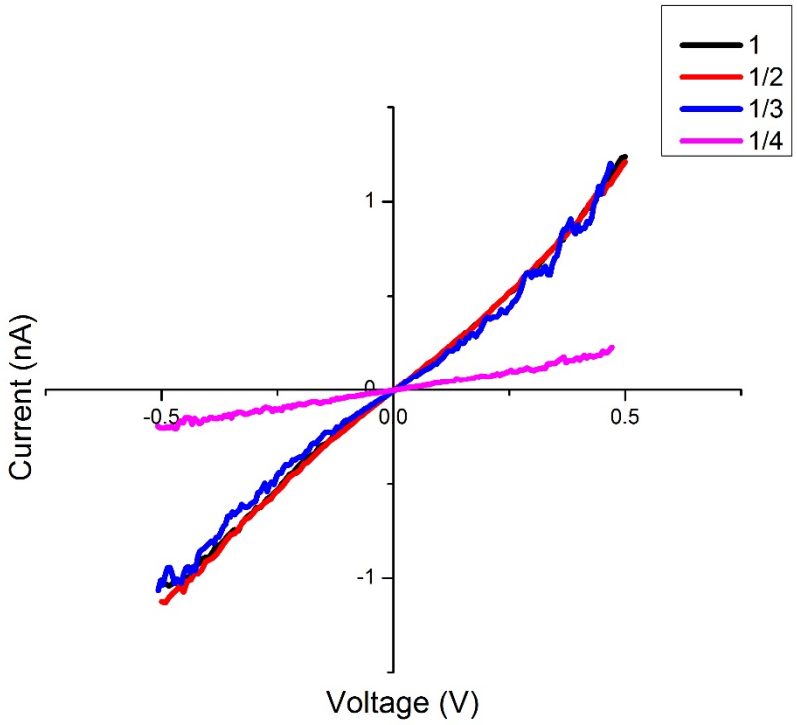

Figure 3.6 Mean I-V curves for the various junctions studied.

Table 3.2. Mean Resistance of the OPV Junction Before and After Exposure to Analyte

Junction Type	**Resistance (GΩ)[a]**	**Corrected Resistance (GΩ)[b]**
1	0.54 ± 0.01	
1/2	0.51 ± 0.01	
1/3	0.62 ± 0.02	2.48 ± 0.03
1/4	2.53 ± 0.07	10.4 ± 0.5

[a] Resistance calculated from the slope of the Ohmic region (-0.1 V to 0.1 V). [b]The corrected resistance was calculated by considering only junctions where the measured resistance was greater than 1 GΩ.

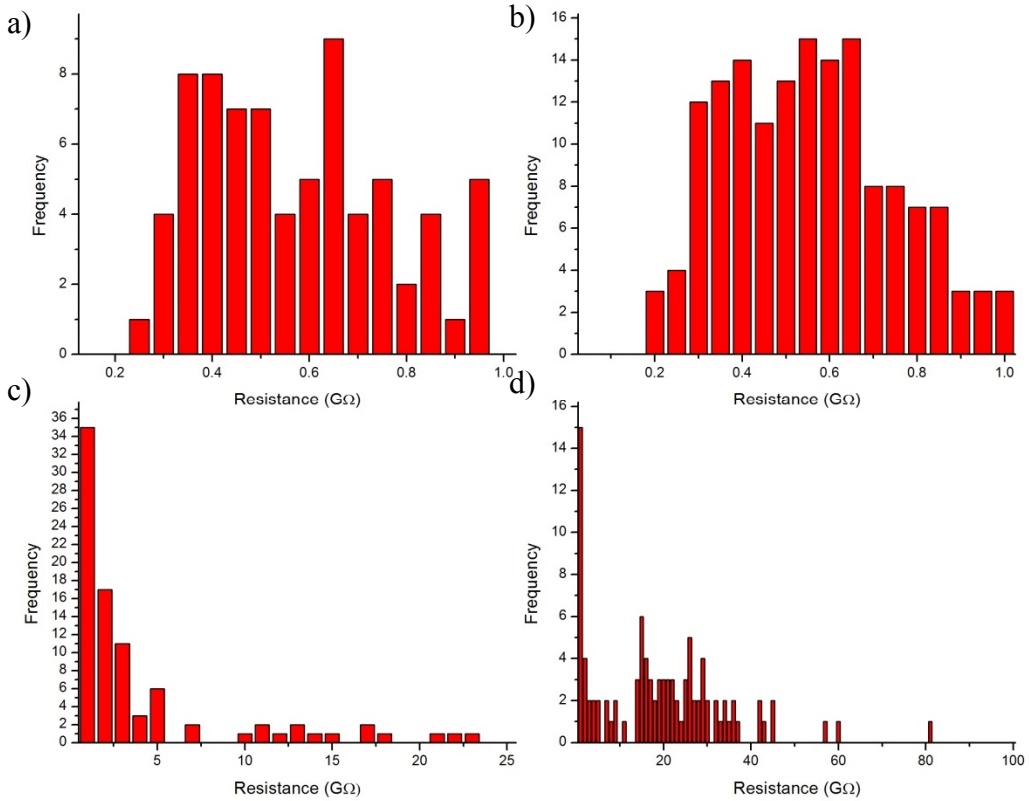

Figure 3.7 Histogram of measured resistances for a) **1**, b) **1/2**, c) **1/3** and d) **1/4**.

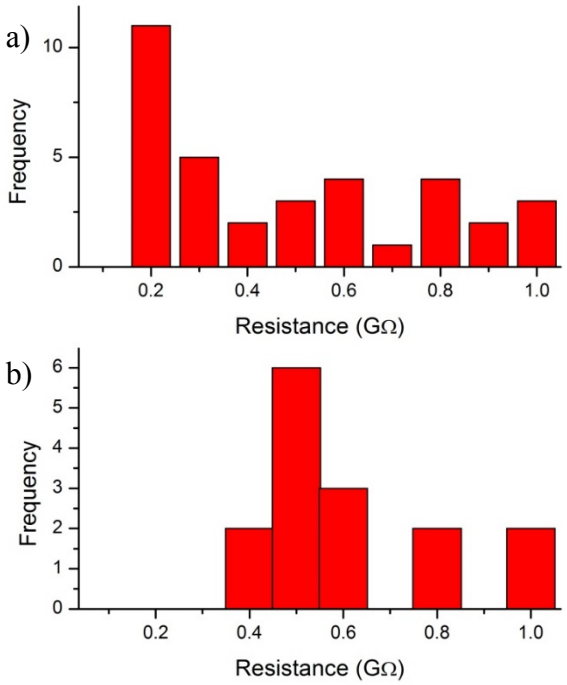

Figure 3.8 Histogram representing the measured resistances for a) 1/3 and b) 1/4 that were between 0 and 1 GΩ.

In order to better distinguish between the different I-V curves histograms were plotted that looked at the individual measured resistances for each junction studied. Examination of the histogram for **1** (Figure 3.7a) reveals that the measured resistances all fall between 0 and 1 GΩ. This also applies for the case where **2** is the analyte which agrees with the fact that the resistivity remains unchanged upon addition of **2** (Figure 3.7b). However, addition of **3** and **4** seems to lead to a spread of resistances over multiple orders of magnitude (Figure 3.7 c and d). What is interesting to note though is that in both cases, there is a large bin representing resistances that fall between 0 and 1 GΩ. Expanding this bin for both analytes (Figure 3.8) reveals histograms similar to the one measured for **1**. This leads us to conclude that a certain number of **1** molecules insert into the monolayer without interacting with either **3** or **4**. It was also observed that the number of unbound molecules of **1** was greater for experiments using **3** when compared to those using **4** as the analyte. This is in good agreement with the fluorescence experiments and is expected given the extra nitro group present on **4**.

Building on the histogram data, we removed the resistances that fell below 1 GΩ and used only those greater than this particular value to calculate a corrected resistance for **1/3** and **1/4** (Table 3.2). In doing so the larger effect of additional electron withdrawing groups is observed again. **4** which has the extra nitro group seems to produce a larger corrected resistance than is the case when **3** is used as the analyte. Furthermore, **4** also produced a larger number of measured resistances greater than 1 GΩ. 85% of all measured resistances for **1/4** were greater than 1 GΩ and used to calculate the measured resistance as opposed to only 60 % of those for **1/3**.

It is well established that molecules with electron-withdrawing moieties have low empty π^* orbitals which facilitates electron transfer from the sensing molecule to the analyte[24]. This

phenomenon is frequently exploited in fluorescence-based sensing methods[25,26]. It is also believed that this donor-acceptor interaction is responsible for the observed conductance effects. **1** is known to be a hole conductor[21] which means its charge transport properties are dominated by the position of the HOMO relative to the Fermi level of the metal. Indeed when electron-withdrawing analytes complex with a molecule such as **1,** it is highly probable that this causes the HOMO to shift away from the Fermi level of the metal, thus causing the measured decrease in conductance. The results are consistent with similar work by Venkataraman et al that found that when they functionalized hole carriers with electron-withdrawing groups the HOMO shifted away from the Fermi level causing a decrease in conductivity[27]. Despite the fact that this in turn leads to the LUMO being much better aligned with the Fermi level of the gold, we do not believe that analytes like **2** which contain electron-donating groups would increase the conductivity. This could only happen if tunneling could occur through the LUMO, since a new conduction channel would open up through which electrons could tunnel. This does not happen though in this particular case. That is because in molecules like **1** where the wire is connected to the metal through thiol groups, the p orbital on the sulfur is degenerate with the HOMO of the molecular wire while the LUMO is isolated at the Au-S interface[19,28]. For this reason only electron-deficient analytes will have an effect on the conductivity.

3.5 Conclusion

The proof-of-concept experiments carried out in this work have demonstrated the potential of molecular wire for detecting nitroaromatic compounds. Exposure to electron-withdrawing analytes such as **3** and **4** produced a measurable change in conductance of **1**. The largest effect was observed with **4** which was expected due to the additional nitro group on the molecule. On the other hand exposure to electron-donating **2** produced no measurable effect on

the conductance. The correlation between conductance experiments and fluorescence measurements carried out in solution using the same analytes indicate that the observed drops in conductance are most likely the result of π donor-acceptor interactions. The results of this work demonstrate that molecular wires may be very useful as sensors for nitroaromatic compounds.

3.6 References

(1) Aviram, A.; Ratner, M. A. *Chem. Phys. Lett.* **1974**, *29*, 277–283.
(2) McCreery, R. L.; Bergren, A. J. *Adv. Mater.* **2009**, *21*, 4303–4322.
(3) Fatemi, V.; Kamenetska, M.; Neaton, J. B.; Venkataraman, L. *Nano Lett.* **2011**, *11*, 1988–1992.
(4) Selzer, Y.; Cai, L.; Cabassi, M. a; Yao, Y.; Tour, J. M.; Mayer, T. S.; Allara, D. L. *Nano Lett.* **2005**, *5*, 61–65.
(5) Zimbovskaya, N. a; Pederson, M. R.; Blum, A. S.; Ratna, B. R.; Allen, R. *J. Chem. Phys.* **2009**, *130*, 094702.
(6) Services, U. S. D. of H. and H. **1995**.
(7) Toal, S. J.; Trogler, W. C. *J. Mater. Chem.* **2006**, *16*, 2871.
(8) Ma, Y.; Li, H.; Peng, S.; Wang, L. *Anal. Chem.* **2012**, *84*, 8415–8421.
(9) Xia, Y.; Song, L.; Zhu, C. *Anal. Chem.* **2011**, *83*, 1401–1407.
(10) Balan, B.; Vijayakumar, C.; Tsuji, M.; Saeki, A.; Seki, S. *J. Phys. Chem. B* **2012**, *116*, 10371–10378.
(11) Ma, H.; Gao, R.; Yan, D.; Zhao, J.; Wei, M. *J. Mater. Chem. C* **2013**, *1*, 4128.
(12) Germain, M. E.; Knapp, M. J. *Chem. Soc. Rev.* **2009**, *38*, 2543–2555.
(13) Angione, M. D.; Marinelli, F.; Aquila, A. D.; Pignataro, B.; Torsi, L. *Springer Proc. Phys.* **2009**, *129*, 217–224.
(14) Blum, A. S.; Soto, C. M.; Sapsford, K. E.; Wilson, C. D.; Moore, M. H.; Ratna, B. R. *Biosens. Bioelectron.* **2011**, *26*, 2852–2857.
(15) Chang, S.; Huang, S.; Liu, H.; Zhang, P.; Liang, F.; Akahori, R.; Li, S.; Gyarfas, B.; Shumway, J.; Ashcroft, B.; He, J.; Lindsay, S. *Nanotechnology* **2012**, *23*, 235101.
(16) Das, B. *J. Phys. Chem. C* **2009**, *113*, 16203–16209.
(17) Blum, A. S.; Yang, J. C.; Shashidhar, R.; Ratna, B. *Appl. Phys. Lett.* **2003**, *82*, 3322.
(18) Kushmerick, J. G.; Holt, D. B.; Pollack, S. K.; Ratner, M. a; Yang, J. C.; Schull, T. L.; Naciri, J.; Moore, M. H.; Shashidhar, R. *J. Am. Chem. Soc.* **2002**, *124*, 10654–10655.
(19) Kushmerick, J. J.; Pollack, S. K.; Yang, J. C.; Naciri, J.; Holt, D. B.; Ratner, M. a.; Shashidhar, R. *Ann. N. Y. Acad. Sci.* **2003**, *1006*, 277–290.
(20) Morita, T.; Lindsay, S. *J. Am. Chem. Soc.* **2007**, *129*, 7262–7263.
(21) Davis, W. B.; Svec, W. A.; Ratner, M. A.; Wasielewski, M. R. *Nature* **1998**, *396*, 60–63.
(22) Blum, A. S.; Kushmerick, J. G.; Pollack, S. K.; Yang, J. C.; Moore, M.; Naciri, J.; Shashidhar, R.; Ratna, B. R. *J. Phys. Chem. B* **2004**, *108*, 18124–18128.
(23) Fan, F.-R. F.; Yang, J.; Cai, L.; Price, D. W.; Dirk, S. M.; Kosynkin, D. V; Yao, Y.; Rawlett, A. M.; Tour, J. M.; Bard, A. J. *J. Am. Chem. Soc.* **2002**, *124*, 5550–5560.
(24) Xiao, X.; Xu, B.; Tao, N. *Angew. Chem. Int. Ed. Engl.* **2004**, *43*, 6148–6152.

(25) Dudhe, R. S.; Sinha, J.; Kumar, A.; Rao, V. R. *Sensors Actuators B Chem.* **2010**, *148*, 158–165.
(26) Che, Y.; Gross, D. E.; Huang, H.; Yang, D.; Yang, X.; Discekici, E.; Xue, Z.; Zhao, H.; Moore, J. S.; Zang, L. *J. Am. Chem. Soc.* **2012**, *134*, 4978–4982.
(27) Venkataraman, L.; Park, Y. S.; Whalley, A. C.; Nuckolls, C.; Hybertsen, M. S.; Steigerwald, M. L. *Nano Lett.* **2007**, *7*, 502–506.
(28) Yaliraki, S.; Kemp, M.; Ratner, M. *J. Am. Chem. Soc.* **1999**, *121*, 3428–3434.

4 Fusion Peptides to Generate Dense Surface Coverages of Gold Nanoparticles

The following chapter is adapted from 'Dual-Affinity Peptides to Generate Dense Surface Coverage of Nanoparticles', Julia Del Re and Amy Szuchmacher Blum, Appl. Surf. Sci., 296, 24(2014)

4.1 Preface

In order to take advantage of the exciting properties of molecular wires it is necessary to develop a method to integrate them into functional circuits. The following chapter looks at the preliminary steps taken to develop a device based on molecular wires. The desired design looks at using densely packed gold nanoparticles on insulating silicon dioxide surfaces. Using fusion peptides gold nanoparticles were synthesized and pre-aggregated in solution via interactions with metal ions. These aggregates were then bound to silicon dioxide substrates using another fusion peptide to accomplish this. The results demonstrated that when divalent metal ions like Zn^{2+} and Ni^{2+} are used large areas of densely packed gold nanoparticle networks are formed on the surface. Eventually these networks could be assembled between lithographically-defined gold electrodes on the silicon dioxide surface thus enabling current to flow between the electrodes.

4.2 Introduction

Nature serves as an inspiration for forming highly-ordered self-assembled structures. Biomolecules are known to bind, synthesize and assemble materials with a high degree of order under mild, aqueous conditions[1]. Peptides are a highly desirable scaffold to control nanoparticle aggregation and substrate binding because they are commercially available and simple to use[2]. Furthermore, they have been shown to participate in the synthesis and binding of a wide variety of inorganic materials including metal surfaces[3], metallic nanoparticles[4–6] and metal oxides[7–9]. The functionality of peptides is further enhanced when two different domains, each with an

affinity towards a different material, are fused together creating what is called a fusion peptide that is multifunctional in nature[10]. This property makes them capable of participating in the synthesis and assembly of hybrid nanomaterials and makes them powerful tools in nanotechnology[11,12].

Densely packed networks of gold nanoparticle on surfaces like silicon dioxide are highly desirable for their use in fields such as molecular electronics[13]. These systems require that the nanoparticles be spaced closely enough together to minimize conductive breaks in the network, and that their surface coverage be quite high. This is difficult to achieve though, as similarly charged gold nanoparticles experience electrostatic repulsion in solution. As such, a material is needed that will help provide control over nanoparticle spacing and density. It is first necessary to synthesize stable gold nanoparticles and then gain control over their interactions. The next step would be to bind them in high density on silicon dioxide surfaces.

Early work by Rajesh Naik and colleagues has demonstrated that fusion peptides can be successfully used to synthesize gold nanoparticles that can form stable solution-phase aggregates via metal ion interactions[2,10,14]. These aggregates are closely spaced and, were it possible to bind them to a silicon dioxide substrate, they would be ideal candidates for forming densely packed nanoparticle networks on insulating surfaces. In order to achieve binding of the aggregates to a silicon dioxide surface another peptide is required. Previous work has shown that the QPB1 peptide does an excellent job of binding to silicon dioxide substrates[15–17]. It may be therefore possible to take advantage of this domain and fuse it to a gold binding one, hence creating a peptide that binds both the substrate and the gold nanoparticle network.

In this work, two different peptides whose sequences are listed in Table 4.1 are used to form densely packed gold nanoparticle networks on silicon dioxide surfaces: the Flg-A3 peptide

and the A3-QBP1 peptide. Gold nanoparticles were synthesized using the Flg-A3 peptide (Table 3.1). The A3 domain stabilizes the resulting nanoparticle while the Flg domain gives control over nanoparticle spacing via interactions with metal ions[2,14]. These metal ion interactions lead to stable solution-phase aggregates[18]. The AuNPs are then bound to the silicon dioxide substrate using the A3-QBP1 peptide (Table 4.1). The QBP1 domain is known to bind to silicon dioxide substrates, so it is expected that this domain will bind to the silicon dioxide while the A3 domain binds the gold nanoparticle aggregates[15–17,19]. The binding experiment was also done with citrate stabilized gold nanoparticles to see if any effects from the A3-QBP1 peptide applied to other kinds of gold nanoparticles.

Table 4.1. Sequences of Peptides Studied

Peptide	Sequence
Flg-A3	DYKDDDDK WYSSWAPPMPPF
A3-QBP1	WYSSWAPPMPPFPPPWLYMPPWS

4.3 Experimental

4.3.1 Materials

Flg-A3 and A3-QBP1 peptides (≥ 75% purity) were purchased from the McGill Peptide Synthesis Facility (Montreal, Canada). All other reagents were purchased from Sigma Aldrich (Oakville, ON). Silicon wafers were obtained from Siltronic (Munich, Germany).

4.3.2 Gold Nanoparticle Synthesis

Gold nanoparticles were synthesized by adding 10 μL of Flg-A3 peptide solution (10 mg/ml) to 500 μL of HEPES buffer (100 mM, pH 7). After vortexing the mixture, 5 μL of $HAuCl_4$ (0.1 M) was added, and the solution was left to incubate for 1 hour. The resulting gold nanoparticles were purified by centrifuging them at 13 000 rpms for 10 minutes and redispersing them in 500 μL HEPES buffer (100 mM, pH 7). For experiments involving transition metal

ions, 2.5 - 10 μL of 0.1 M metal ion solution (Ag^{+}, Mg^{2+}, Ni^{2+} or Zn^{2+}) was added to the nanoparticle solution which as then left to incubate for 1 hour.

Citrate stabilized nanoparticles were synthesized according to a procedure developed by Jana et al[20].

4.3.3 Effect of Ionic Strength on Gold Nanoparticle Aggregation

500 μL of Flg-A3 AuNPs was spiked with 1 μL aliquots of 5 M NaCl. The solution was then left to incubate for 10 minutes before a UV/VIS spectrum was collected.

4.3.4 Gold Nanoparticle Binding

Silicon wafers were cleaned using the RCA-1 and RCA-2 cleaning procedures, rinsed with deionized water and dried with a gentle stream of nitrogen gas. They were then immersed in a solution of A3-QBP1 peptide (0.37 mM) overnight. Following removal from this solution, the wafers were rinsed with deionized water and dried with a gentle stream of nitrogen gas. They were then immersed in the gold nanoparticle solution overnight, after which they were rinsed with deionized water and dried with nitrogen gas. A second type of binding experiment was done repeating all of the above steps except peptide deposition.

4.3.5 Instrumentation

Gold nanoparticles were characterized using a Cary 100 Bio UV/VIS (Agilent Technologies, Mississauga, Canada) using quartz cuvettes that had a pathlength of 0.3 cm (Spectrocell, Oreland, PA). The nanoparticle size and spacing was characterized using a Philips CM200 200 kV transmission electron microscope (TEM). Dynamic light scattering (DLS) was done using a 90Plus Particle Size Analyser (Brookhaven Instruments, Holtsville, NY). Peptide and nanoparticle binding to the substrates was characterized using a Hitachi S-4700 field

emission scanning electron microscope (SEM) and an Asylum Cypher Scanning Probe Microscope (Asylum Research, Santa Barbara, CA).

4.4 Results

Gold nanoparticles were synthesized and characterized with UV/VIS spectroscopy and TEM. In this synthesis, the HEPES buffer serves as the reducing agent to form Au(0) from Au (III)[21]. Synthesis proceeded rapidly, and after a matter of minutes a purplish red solution had formed (Figure 4.1a). Addition of metal ion caused a visible colour change in all cases except when Mg^{2+} was added (Figure 4.1). In cases where a colour change was observed, the colour was dependent on the ion used. Both Ni^{2+} and Zn^{2+} caused the AuNP solution to turn purple, whereas Ag^{+} caused it to turn a blue colour. Citrate-stabilized nanoparticles were synthesized with a diameter of 3.5 nm[20].

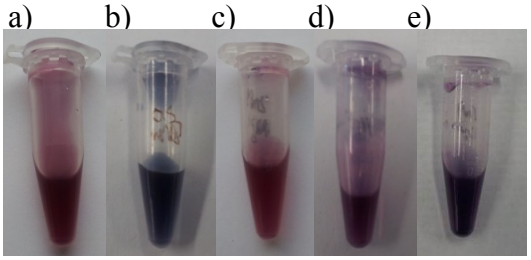

Figure 4.1 Images of AuNP solutions for a) Flg-A3 AuNPs, b) Flg-A3 and 0.5 mM Ag^{+}, c) Flg-A3 AuNPs and 2 mM Mg^{2+}, d) Flg-A3 AuNPs and 1 mM Ni^{2+}, e) Flg-A3 AuNPs and 1 mM Zn^{2+}.

Knowing that the colour of nanoparticle solutions derives from a collective oscillation of surface electrons known as surface plasmon resonance (SPR), which can be observed in the ultraviolet visible spectrum, UV/VIS spectra were collected for all samples (Figure 4.2). Changes in the location of the SPR band can be indicative of changes in size or spacing of nanoparticles. Addition of the metal ions produced red-shifts and broadening of the SPR band (Figure 4.2). The degree of red-shift and broadening though was strongly dependent on the

metal ion used (Table 4.2). Ag^{+} produced the largest red-shift and most significant amount of peak broadening while Mg^{2+} produced the smallest. The minimal effect that Mg^{2+} had on the position of the SPR band was expected as there was no apparent change in the colour of the AuNP solution once it was added. Interestingly the other two divalent ions studied, Ni^{2+} and Zn^{2+} caused larger red-shifts than Mg^{2+} but smaller ones than Ag^{+}. The UV/VIS data suggests that there are likely changes in nanoparticle spacing, as it is well known that when nanoparticles are sufficiently close together plasmonic coupling takes place and the SPR band red-shifts[22].

s

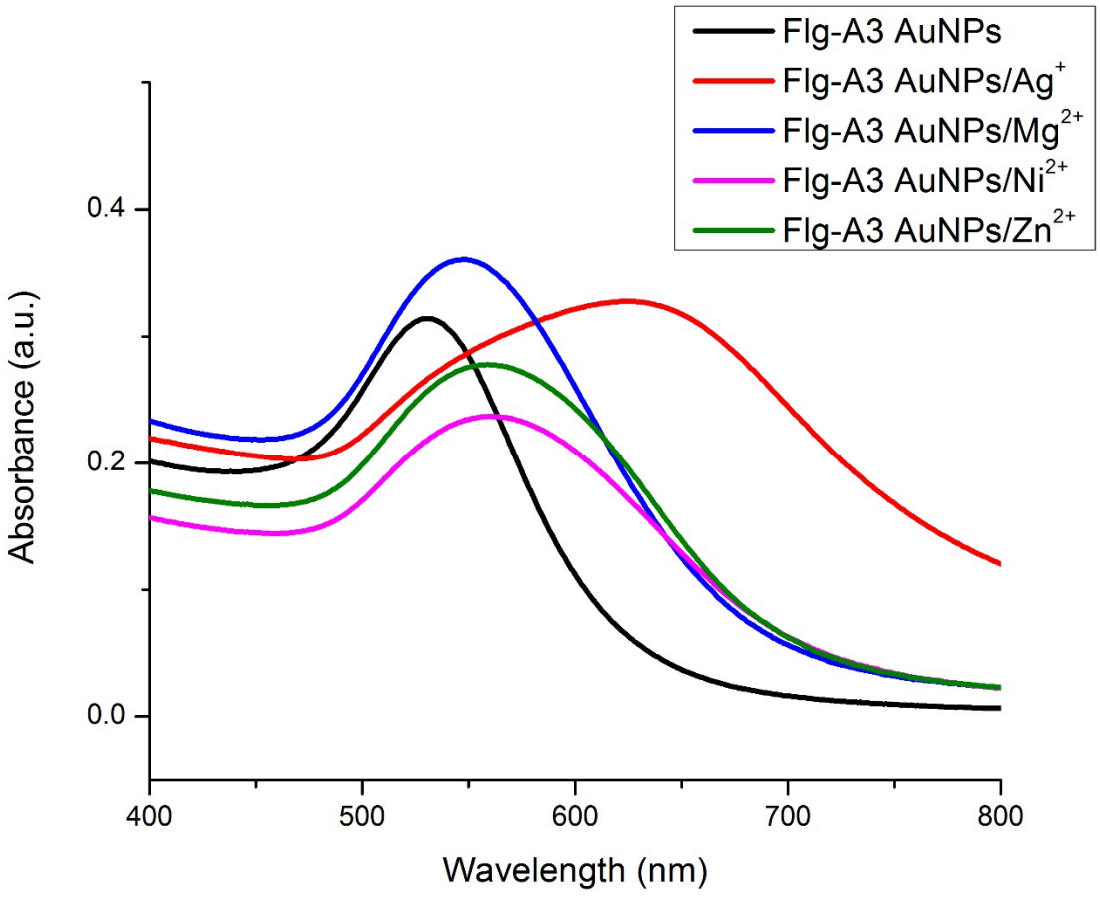

Figure 4.2 UV/VIS spectra for Flg-A3 AuNPs, Flg-A3 AuNPs and Ag^{+}, Flg-A3 AuNPs and Mg^{2+}, Flg-A3 AuNPs and Ni^{2+} and Flg-A3 AuNPs and Zn^{2+} .

Table 4.2. SPR Band for Flg-A3 AuNPs as Determined from UV/VIS spectroscopy

Nanoparticle Type	SPR Band (nm)
Flg-A3	531
Flg-A3/Ag^{+}	623
Flg-A3/Mg^{2+}	548
Flg-A3/Ni^{2+}	560
Flg-A3/Zn^{2+}	556

To confirm that the observed red-shifts of the SPR were caused by AuNP aggregation, TEM was used to characterize the size and spacing of the gold nanoparticles (Figure 4.3, Table 4.3). The spacing was determined by measuring the nearest neighbour edge to edge separation. In the absence of metal ion nanoparticles which are 9.9 ± 2.1 nm in diameter are produced, which is in good agreement with previously published literature[10]. Furthermore, the nanoparticle size distribution is Gaussian in nature (Figure 4.4). Metal ion addition does not seem to affect the size of the nanoparticle with the exception of Ag^{+}, where the size of the nanoparticle nearly doubles. We believe that this significant change in size is likely the result of Ag^{+} reduction on the surface of the gold nanoparticle. In this particular nanoparticle synthesis, HEPES is used to reduce the Au (III) ion. Previous work by other groups has shown that HEPES can be used to reduce Ag^{+} as well[23,24]. Indeed, once Ag^{+} is added to the AuNP solution the nanoparticles crash out after only a few hours which is likely due to the fact that there are no capping agents present to bind and stabilize Ag(0) once it is formed on the surface of the nanoparticle.

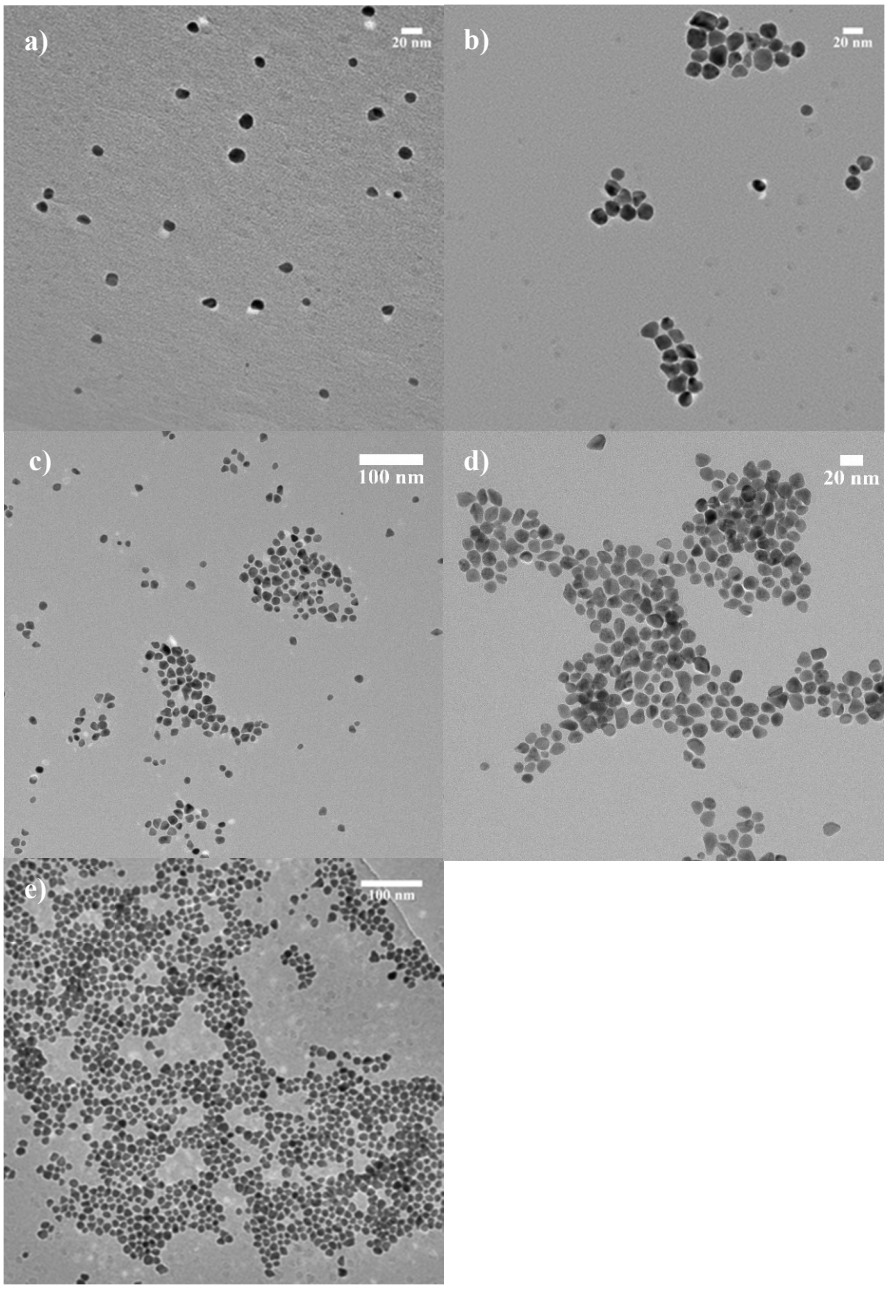

Figure 4.3 TEM images for a) Flg-A3 AuNPs, b) Flg-A3 AuNPs and Ag^{+}, c) Flg-A3 AuNPs and Mg^{2+} d) Flg-A3 AuNPs and Ni^{2+} and e) Flg-A3 AuNPs and Zn^{2+}.

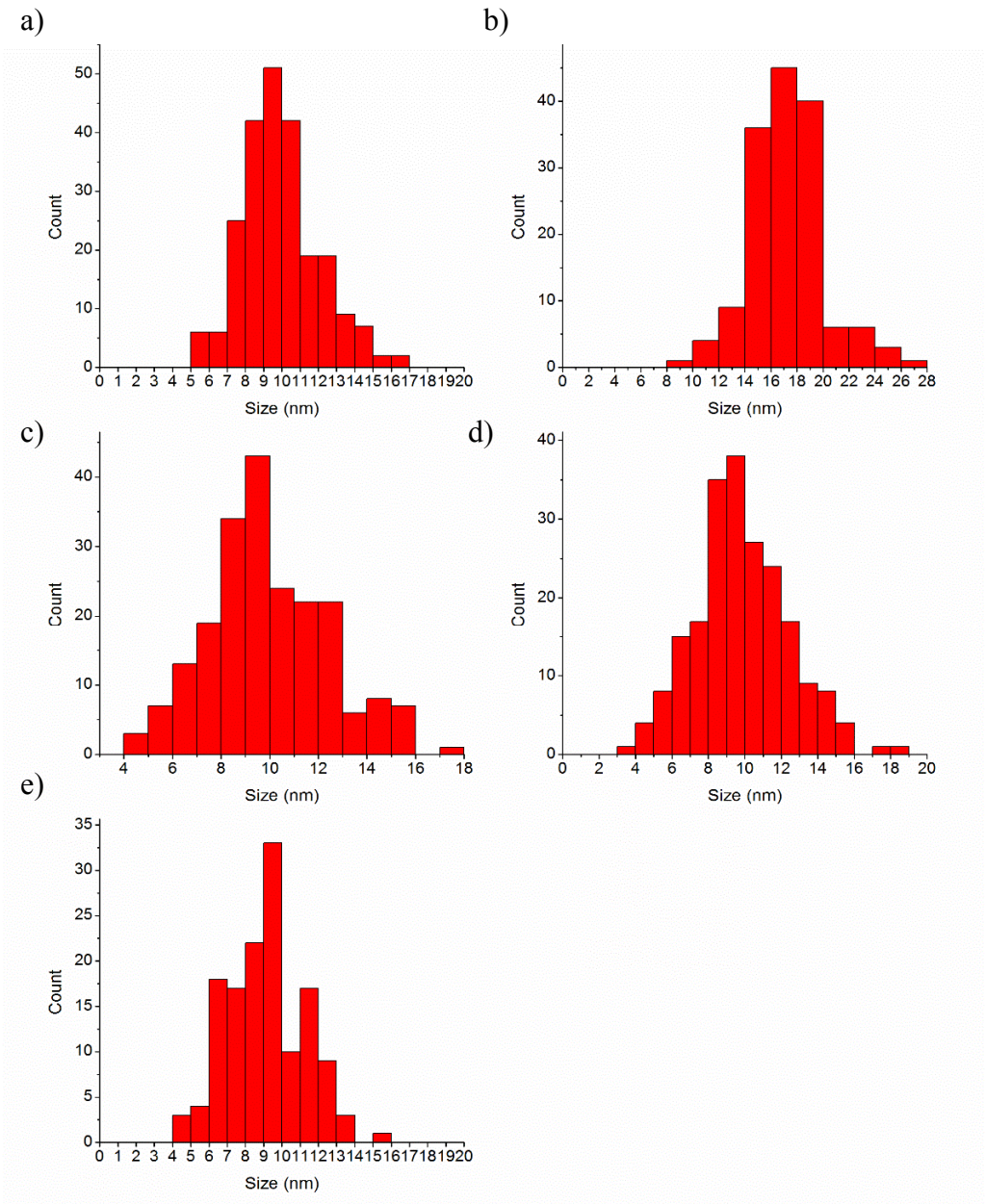

Figure 4.4 Size distribution data for a) Flg-A3 AuNPs, b) Flg-A3 AuNPs and Ag^{+}, c) Flg-A3 AuNPs and Mg^{2+}, d) Flg-A3 AuNPs and Ni^{2+} and e) Flg-A3 AuNPs and Zn^{2+}.

Table 4.3 Size and Spacing Data for Flg-A3 Gold Nanoparticles as Determined from TEM

Nanoparticle Type	**Size (nm)**	**Interparticle Distance (nm)**
Flg-A3	9.9 ± 2.1	73.4 ± 69.7
Flg-A3/Ag^{+}	17.2 ± 2.8	1.8 ± 0.7
Flg-A3/Mg^{2+}	9.6 ± 2.6	2.1 ± 0.9
Flg-A3/Ni^{2+}	9.9 ± 2.4	2.3 ± 1.0
Flg-A3/Zn^{2+}	9.1 ± 2.1	2.1 ± 1.1

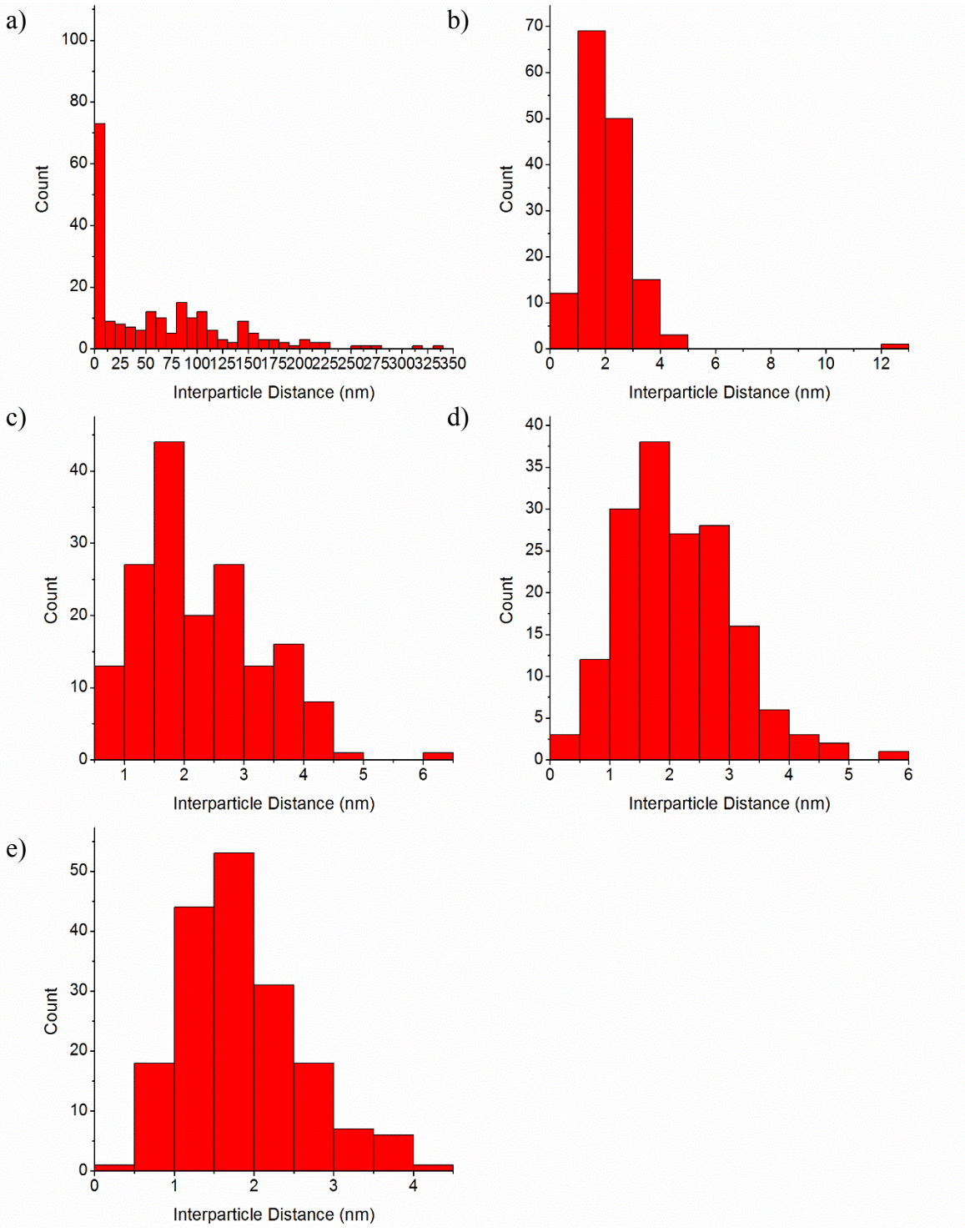

Figure 4.5 Interparticle spacing distributions for a) Flg-A3 AuNPs, b) Flg-A3 AuNPs with Ag^{+} and c) Flg-A3 AuNPs with Mg^{2+}, d) Flg-A3 AuNPs and Ni^{2+} and e) Flg-A3 AuNPs with Zn^{2+}.

The spacing and size of aggregation of the nanoparticles was also studied with the TEM by measuring the separation between two neighbouring nanoparticles (Figure 4.3, 4.5, Table

4.3). As with the UV/VIS experiments the degree of aggregation depended on the metal ion used. In the absence of any metal ion, the Flg-A3 AuNPs are spaced very far apart and there is no real trend in spacing. Even upon drying for TEM imaging, the AuNPs remain very far apart. This is likely due to the fact that the Flg-A3 peptide is rich in negatively-charged aspartic acid residues, thus producing large amounts of electrostatic repulsion between neighbouring AuNPs. When a metal ion is introduced into the AuNP solution, the spacing is reduced dramatically to around 2 nm in all cases. The lack in variation of the nanoparticle spacing suggests that the ligand shell plays a vital role in controlling spacing, which has previously been observed for monolayer-stabilized gold nanoparticles.

The size of the nanoparticle networks varies greatly depending on the metal ion used. Ag^{+} and Mg^{2+} produce only very small nanoparticle aggregates, whereas Ni^{2+} and Zn^{2+} produce much larger ones. These results lead us to believe that the observed aggregation is caused by much more than simply electrostatic interactions since Mg^{2+}, a divalent ion, behaves quite differently from the other divalent ions studied.

Table 4.4 Summary of Dynamic Light Scattering Data for Flg-A3 Gold Nanoparticle Systems

Nanoparticle Type	**Hydrodynamic Radius (nm)**
Flg-A3	42
Flg-A3/Ag^{+}	234
Flg-A3/Mg^{2+}	55
Flg-A3/Ni^{2+}	250
Flg-A3/Zn^{2+}	219

Dynamic light scattering (DLS) was done to confirm the metal-ion induced aggregation of Flg-A3 AuNPs in solution (Table 4.4). In the absence of any metal ion the hydrodynamic radius of the nanoparticles is 42 nm. As evidenced by the data presented in Table 4.4 addition of various metal ions to solutions of Flg-A3 AuNPs causes aggregation that is largely dependent on

the ion used. Mg^{2+} causes minimal amounts of AuNP assembly while the others cause it on a larger scale. Ag^{+}, Ni^{2+} and Zn^{2+} have a much larger effect on aggregation. One interesting observation to note is that the difference in hydrodynamic radii for these ions is quite similar which was not observed with the TEM data. The TEM data suggests that aggregation occurs over a much larger scale for Ni^{2+} and Zn^{2+}. We believe that this is a result of the 0.45 μm filters used to treat the samples to remove dust and other potential impurities prior to DLS measurements, which in turn skews the data towards smaller aggregates.

The characteristic interparticle distance was similar in all cases for the various metal ions tested. However as previously stated each different ion produced differences in nanoparticle distance and surface area of the aggregates. Zn^{2+} and Ni^{2+} both displayed significantly more aggregation over a larger surface area than Mg^{2+} or Ag^{+}. This indicates that the observed aggregation in the TEM is not likely a drying effect. DLS measurements on the AuNP solutions further solidified the conclusion that the aggregation is likely the result of a specific interaction between transition metal ions and the peptide. This also supports the notion that the observed effects are a result of more than just electrostatic attraction between the metal cation and negatively charged AuNP. Were the aggregation a result of solely electrostatic interactions, all metal ions tested would produce similar effects however that is not the case observed here. Previous studies that looked at the interaction between Flg-A3 and metal cations like Ag^{+} and Pd^{4+} used circular dichroism measurements to show that binding of these ions to the peptide induced a conformational change from an unordered structure to a more helical one[25]. Therefore it is highly probable that this is the explanation for the observed effects when Zn^{2+} and Ni^{2+} are added to the system. Furthermore, since Mg^{2+} produces no significant SPR shift or aggregation it is highly likely that it is not inducing a conformational change in the Flg-A3 peptide.

To confirm that the observed results are due to specific metal ion interactions with the peptide and not changes in ionic strength a solution of Flg-A3 AuNPs was spiked with 1 µL aliquots of 5 M NaCl to see if that would produce a shift in the SPR band of the nanoparticles (Figure 4.6). Each aliquot increased the ionic strength by approximately 10 mM which was much larger than the increase in ionic strength brought about by the transition metal ions (which never increased the ionic strength more than 3 mM). Despite the fact that significantly larger ionic strengths were tested when compared to those experiments run with transition metal ions there is no observable red shift in the SPR band. In fact there was no visible colour change or shift of the SPR band observed until the final concentration of NaCl was approximately 0.4 M and the total ionic strength was 0.43 M. This further supports the hypothesis that the observed aggregation is the result of specific metal ion-peptide interactions and not salt-induced aggregation.

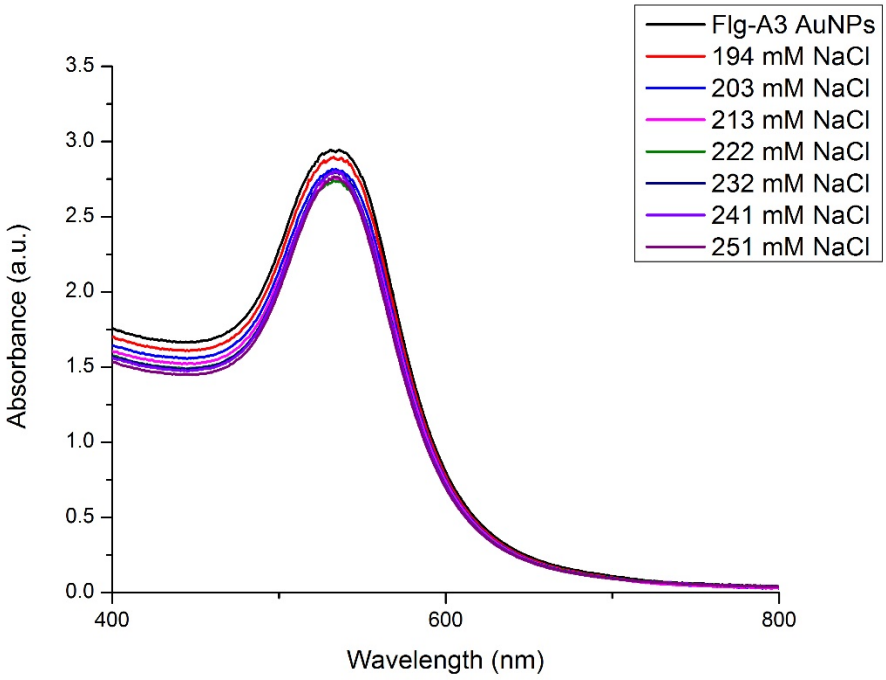

Figure 4.6 UV/VIS data for Flg-A3 AuNPs in solutions with increasing ionic strength.

Having established that metal ions can be used to control AuNP assembly, the binding properties of both the A3-QBP1 peptide and the AuNPs was examined on silicon dioxide substrates. The QBP1 is expected to bind to the silicon dioxide while the A3 will bind the gold nanoparticles[14,15,17]. Prior to AuNP deposition atomic force microscopy (AFM) was used to determine the optimal pH at which to carry out A3-QBP1 binding (Figure 4.7). Peptide deposition was studied over a pH range of 7 to 8.

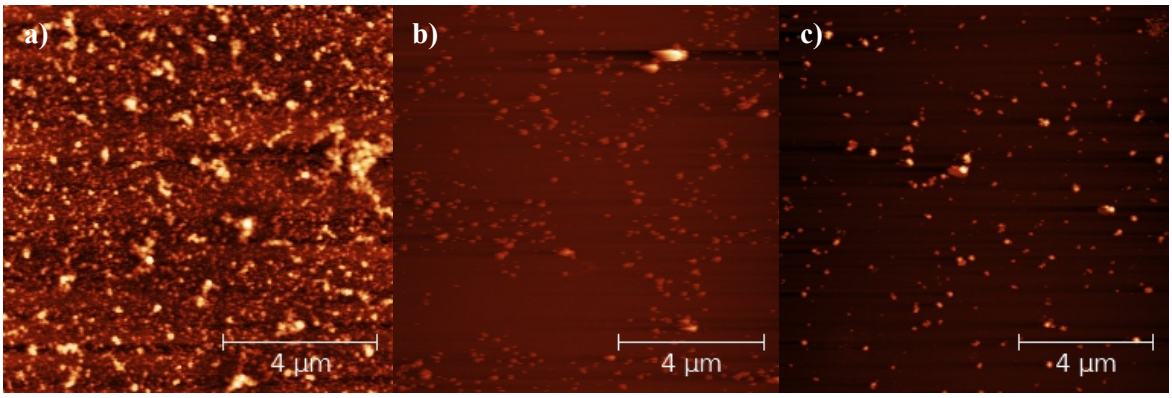

Figure 4.7 Tapping mode AFM images for the binding of A3-QBP1 to silicon dioxide at a) pH 7, b) pH 7.5 and c) pH 8.

AFM reveals that at lower pH the A3-QBP1 peptide seems to spread itself over the substrate whereas at higher ones it self-assembles in islands. This is likely caused by the acidity of the surface silanol groups as none of the pK_as of the amino acid side groups fall in this pH range. It is highly likely that at lower pH, a greater number of silanol groups are protonated, leaving more of them available for hydrogen bonding interactions. Hydrogen bonding interactions are thought to be one of the mechanisms through which the peptide binds to the surface[15].

After establishing pH 7 as the ideal pH for binding of the A3-QBP1 peptide, AuNP binding experiments were carried out. AuNPs were deposited on either bare silicon dioxide substrates or A3-QBP1 coated silicon dioxide substrates. The following systems were studied

for their surface binding properties: Flg-A3 AuNPs, Flg-A3 AuNPs/Ag^{+}, Flg-A3 AuNPs/Mg^{2+}, Flg-A3 AuNPs/Zn^{2+} and Flg-A3 AuNPs/Ni^{2+}. AuNP self-assembly was examined to see if they would bind to the surface with the same density observed in solution. Binding was characterized using scanning electron microscopy (SEM) (Figure 4.8).

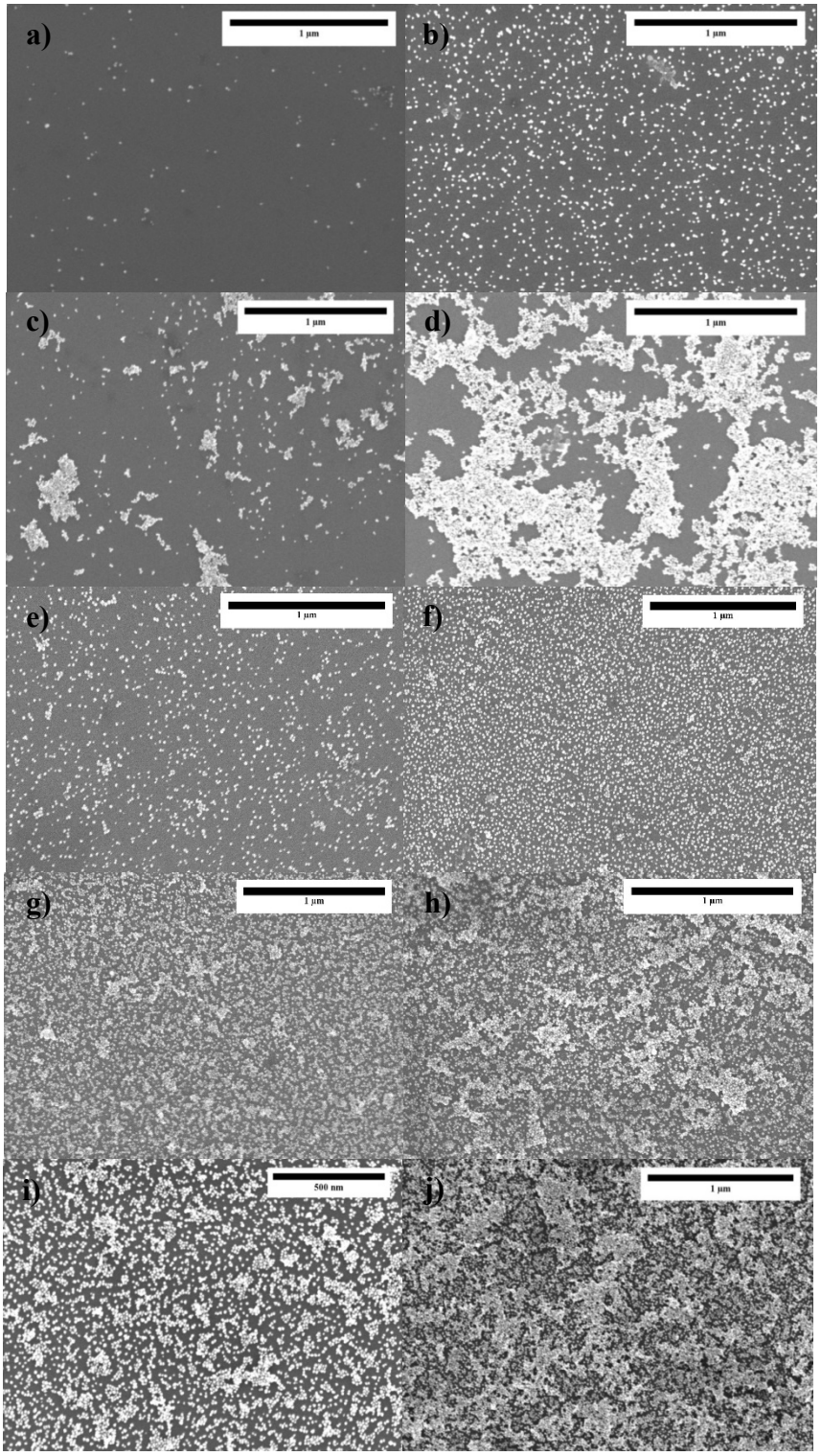

Figure 4.8 SEM images of a) Flg-A3 AuNPs on silicon dioxide and b) A3-QBP1 coated silicon dioxide. c) Flg-A3 AuNPs/Ag^{+} on silicon dioxide and d) A3-QBP1 coated silicon dioxide. e) Flg-A3 AuNPs/Mg^{2+} on bare silicon dioxide and f) A3-QBP1 coated silicon dioxide. g) Flg-A3 AuNPs/Ni^{2+} on silicon dioxide and h) on A3-QBP1 coated silicon dioxide. i) Flg-A3 AuNPs/Zn^{2+} on silicon dioxide and on A3-QBP1 coated silicon dioxide.

In all cases, there is some non-specific binding of the nanoparticles to the bare substrate, however surface coverage increases dramatically when A3-QBP1 is deposited on the surface prior to AuNP deposition. This is most noticeable for the Flg-A3 AuNPS and the Flg-A3 AuNPs with Ag^{+}. As with the experiments done in solution, each metal ion had a unique effect. Ag^{+} did decrease AuNP spacing but there were large areas of the substrate that were left bare which would be unsuitable for many applications like molecular electronics where this would create conductive breaks in the network. Meanwhile Mg^{2+} had almost no effect on the spacing and Ni^{2+} and Zn^{2+} seemed to form what appeared to be large areas of densely packed networks. Closer examination of these areas in the Flg-A3 AuNPs/Zn^{2+} experiment (Figure 4.9) reveals large areas of densely packed AuNPs.

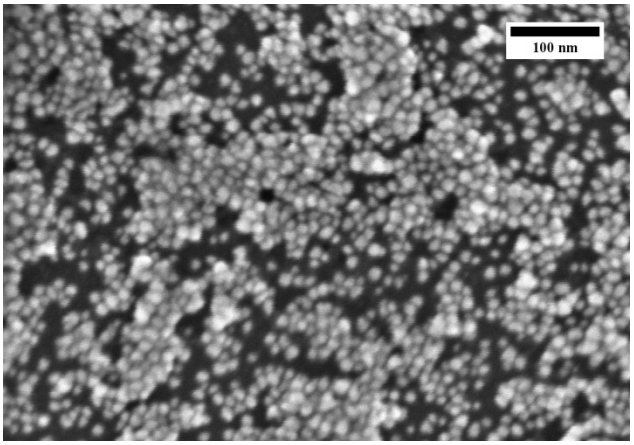

Figure 4.9 A close up SEM image of Flg-A3 AuNPs/Zn^{2+} on a silicon dioxide surface coated with A3-QBP1.

To confirm that the densely packed networks were the result of the Flg-A3 peptide's interactions with metal ions, experiments with citrate-stabilized gold nanoparticles were also done. The experiments were also used to determine if A3-QBP1 could bind different types of AuNPs to the silicon dioxide substrate. As with the previous binding experiments they were

deposited on bare silicon dioxide substrates or A3-QBP1 coated substrates and characterized with SEM (Figure 4.10).

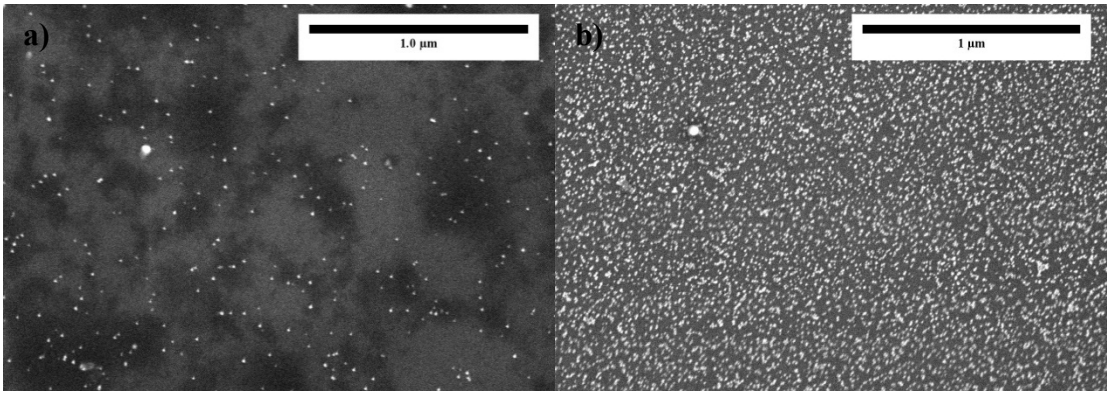

Figure 4.10 SEM images of a) Citrate-stabilized AuNPs on bare silicon dioxide and b) citrate-stabilized AuNPs on A3-QBP1 coated silicon dioxide.

Examination of the SEM reveals that as with the other AuNPs, there is some non-specific binding to the substrate. When the A3-QBP1 peptide is deposited onto the substrate prior to AuNP binding, the surface coverage significantly increases. The nanoparticle spacing however is quite poor indicating that the Flg-A3 interaction with metal ions is necessary to achieve areas of densely-packed gold nanoparticles that would be useful for molecular electronics applications. The increased surface coverage though indicates that the A3-QBP1 can work on different types of AuNPs regardless of the stabilizing ligand and that it is necessary to achieve the high surface coverage observed in this work.

4.5 Conclusions

Dual-affinity peptides have been used to form densely packed gold nanoparticle networks on silicon dioxide substrates. Gold nanoparticles were first synthesized using the Flg-A3 peptide as a stabilizing ligand. Transition metal ion interactions with the Flg domain enable control over the nanoparticle spacing. The resulting networks were then tethered to silicon dioxide substrates using A3-QBP1 peptides. We have thus demonstrated that fusion peptides can be used to form

targeted structures through self-assembly. This method is relatively quick and simple which makes fusion peptides a powerful tool for the development of hybrid nanostructures. These networks are expected to be useful in molecular electronics for integration of conducting molecules into circuits.

4.6 References

(1) Sarikaya, M.; Tamerler, C.; Jen, A. *Nat. Mater.* **2003**, *2* (9), 577–585.
(2) Slocik, J. M.; Zabinski, J. S.; Phillips, D. M.; Naik, R. R. *Small* **2008**, *4* (5), 548–551.
(3) Seker, U. O. S.; Wilson, B.; Sahin, D.; Tamerler, C.; Sarikaya, M. *Biomacromolecules* **2009**, *10* (2), 250–257.
(4) Nam, K. T.; Lee, Y. J.; Krauland, E. M.; Kottmann, S. T.; Belcher, A. M. *ACS Nano* **2008**, *2* (7), 1480–1486.
(5) Aili, D.; Gryko, P.; Sepulveda, B.; Dick, J. a G.; Kirby, N.; Heenan, R.; Baltzer, L.; Liedberg, B.; Ryan, M. P.; Stevens, M. M. *Nano Lett.* **2011**, *11* (12), 5564–5573.
(6) Coppage, R.; Slocik, J. M.; Sethi, M.; Pacardo, D. B.; Naik, R. R.; Knecht, M. R. *Angew. Chem. Int. Ed. Engl.* **2010**, *49* (22), 3767–3770.
(7) Chen, H.; Su, X.; Neoh, K.-G.; Choe, W.-S. *Langmuir* **2009**, *25* (3), 1588–1593.
(8) Eteshola, E.; Brillson, L. J.; Lee, S. C. *Biomol. Eng.* **2005**, *22* (5-6), 201–204.
(9) Yokoo, N.; Togashi, T.; Umetsu, M.; Tsumoto, K.; Hattori, T.; Nakanishi, T.; Ohara, S.; Takami, S.; Naka, T.; Abe, H.; Kumagai, I.; Adschiri, T. *J. Phys. Chem. B* **2010**, *114* (1), 480–486.
(10) Slocik, J. M.; Naik, R. R. *Adv. Mater.* **2006**, *18* (15), 1988–1992.
(11) Hnilova, M.; Khatayevich, D.; Carlson, A.; Oren, E. E.; Gresswell, C.; Zheng, S.; Ohuchi, F.; Sarikaya, M.; Tamerler, C. *J. Colloid Interface Sci.* **2011**, *365* (1), 97–102.
(12) Nochomovitz, R.; Amit, M.; Matmor, M.; Ashkenasy, N. *Nanotechnology* **2010**, *21* (14), 145305.
(13) Conklin, D.; Nanayakkara, S.; Park, T.-H.; Lagadec, M. F.; Stecher, J. T.; Therien, M. J.; Bonnell, D. a. *Nano Lett.* **2012**, *12* (5), 2414–2419.
(14) Slocik, J. M.; Stone, M. O.; Naik, R. R. *Small* **2005**, *1* (11), 1048–1052.
(15) Oren, E. E.; Notman, R.; Kim, I. W.; Evans, J. S.; Walsh, T. R.; Samudrala, R.; Tamerler, C.; Sarikaya, M. *Langmuir* **2010**, *26* (18), 11003–11009.
(16) Wei, J. H.; Kacar, T.; Tamerler, C.; Sarikaya, M.; Ginger, D. S. *Small* **2009**, *5* (6), 689–693.
(17) Kacar, T.; Ray, J.; Gungormus, M.; Oren, E. E.; Tamerler, C.; Sarikaya, M. *Adv. Mater.* **2009**, *21* (3), 295–299.
(18) Del Re, J.; Blum, A. S. *Appl. Surf. Sci.* **2014**, *296*, 24–30.
(19) Notman, R.; Oren, E. E.; Tamerler, C.; Sarikaya, M.; Samudrala, R.; Walsh, T. R. *Biomacromolecules* **2010**, *11* (12), 3266–3274.
(20) Jana, N.; Gearheart, L. *Langmuir* **2001**, *17* (37), 6782–6786.
(21) Diamanti, S.; Elsen, A.; Naik, R.; Vaia, R. *J. Phys. Chem. C* **2009**, *113* (23), 9993–9997.
(22) Su, K.-H.; Wei, Q.-H.; Zhang, X.; Mock, J. J.; Smith, D. R.; Schultz, S. *Nano Lett.* **2003**, *3* (8), 1087–1090.

(23) Tan, S.; Erol, M.; Attygalle, A.; Du, H. *Langmuir* **2007**, *23* (18), 9836–9843.
(24) Sun, R. W.-Y.; Chen, R.; Chung, N. P.-Y.; Ho, C.-M.; Lin, C.-L. S.; Che, C.-M. *Chem. Commun. (Camb).* **2005**, No. 40, 5059–5061.
;(25) Slocik, J. M.; Govorov, A. O.; Naik, R. R. *Nano Lett.* **2011**, *11* (2), 701–705.

5 Development of a Conjugation Strategy for the Tobacco Mosaic Virus Disk for their Use in Formation of Gold Nanoparticle Assemblies

5.1 Preface

Tobacco mosaic virus coat protein (TMVcp) disks were studied for their ability to template the self-assembly of Flg-A3 gold nanoparticles. The N terminus, which lies at the circumference of the disk, was modified using bioconjugation strategies so that gold nanoparticles would covalently bind it. The conjugation process was studied on two mutants of the TMVcp. It was found that in order to achieve efficient conjugation, it is necessary to mutate the protein so that the N terminus is more accessible in solution. Following mutation and bioconjugation, it was possible to covalently bind Flg-A3 gold nanoparticles to the exterior of the disk, forming gold nanorings which can eventually be studied further.

5.2 Introduction

Ensembles of metallic nanoparticles are thought to be of use in a variety of fields such as molecular electronics[1–3]. Controlling nanoparticle spacing remains quite challenging, as does forming large-scale assemblies. Repulsive interactions between similarly charged nanoparticles often leads to large separations that would render nanoparticles ineffective for molecular electronics applications where small separations are necessary in order for the molecular wire to bridge the gap between neighbouring nanoparticles. Top-down lithographic techniques have proven to be capable of patterning surfaces to form high density metallic nanoparticle arrays with a high degree of reproducibility[4,5]. However in order to generate features small enough to enable that dense packing, electron beam lithography is required, which is time-consuming and does not allow for a high-throughout[6]. Biomolecule-templated self-assembly has been proposed as one

possible alternative to form highly ordered structures on the nanometer scale. Biomolecules have been shown to control the size and shape of the final structure to a high degree and can be used under mild, aqueous conditions[7]. One class of commonly-studied biomolecules is virus coat proteins.

Viral scaffolds are highly desirable templates due to their high degree of monodispersity and well-defined shape[8]. Tobacco mosaic virus is one common example. In its native state, the viral coat protein forms a rod structure 300 nm long with a diameter of 18 nm that consists of 2130 protein subunits around the RNA genome[9]. In the absence of the RNA, the coat protein is capable of forming disk-like and rod structures depending on the pH and ionic strength[10]. The disk, which consists of 34 subunits, is also 18 nm in diameter with an inner pore of 4 nm (Figure 5.1)[11]. Both structures have been shown to template the assembly of a variety of materials such as fluorophores[12,13] and inorganic nanoparticles[11,14], as well serve as scaffolds for the in situ reduction of metal salts[15]. The disk however has not been studied as frequently since it is stable over a narrower pH range[10].

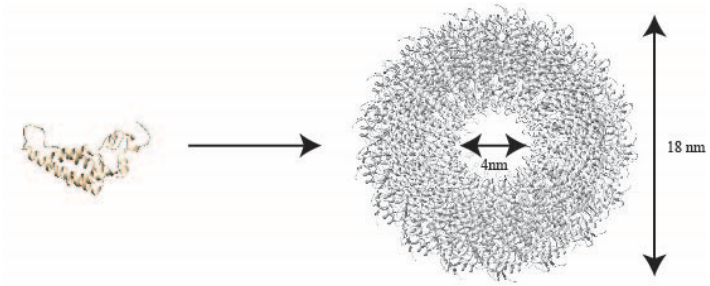

Figure 5.1 The disk assembly of the TMVcp protein

In TMVcp, the N terminus of the protein is on the circumference of the disk, which makes it a desirable target for modification via bioconjugation strategies. However, modification of the N terminus presents many challenges, as a variety of factors influence the success of the reaction

including pH, protein structure, amino acid sequence, and concentration of reagents and protein. Furthermore, amino acids other than the N-terminus target may be susceptible to reaction, which could reduce yield and cause undesirable effects such as protein unfolding. Nevertheless a variety of strategies have been developed for successful modification of the primary amine group such as reactions with N-hydroxy succinimide esters (NHS)[16]. Reactions with these particular reagents are simple and proceed rapidly.

Due to its small size, the disk phase (Figure 5.1) could serve as a suitable template for the assembly of materials to form structures with nanoscale dimensions that would be difficult to achieve with conventional lithography. One example would be to bind gold nanoparticles to the outer edge[11,14]. The Flg-A3 nanoparticles described in the previous chapter would be a suitable candidate for this because the nanoparticles could potentially enable the aggregation of the gold nanorings to form large scale assemblies which could be used in molecular electronics. Figure 5.2 presents a simplified scheme of the desired nanoparticle binding process.

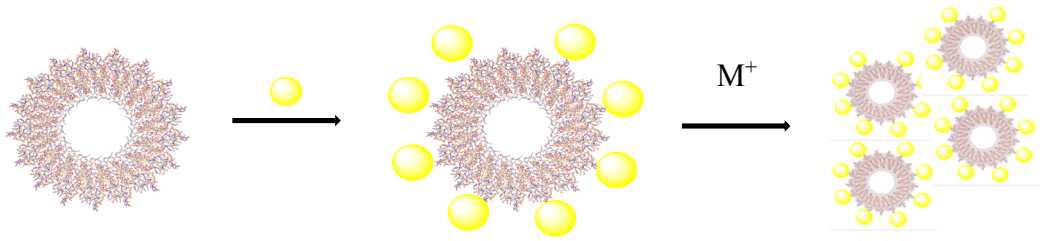

Figure 5.2 Proposed scheme for binding Flg-A3 AuNPs to the outer edge of the TMVcp disk.

This chapter focuses on the conjugation of TMVcp disks using N-lipoyloxy succinimide. Initially, attempts at modifying the N-terminus of the TMVcp were examined. Initially a mutant of wild-type TMVcp was selected for study. In this particular mutant referred to as S123C TMVcp, a serine at the 123 position is swapped for a cysteine residue[11]. For reasons that are not quite well understood the S123C TMVcp tends to prefer the disk phase even under conditions

that normally favour other assemblies hence why it was chosen for this work[17]. Unfortunately in this particular mutant the N terminus is sterically hindered leading to poor conjugation yields. To overcome this an additional mutation was carried out to add amino acids to the N terminus of S123C TMVcp. This mutant referred to as the SAG mutant contains three extra amino acid residues (serine, alanine and glycine) at the N-terminus, which makes the terminal amine more accessible in solution. A conjugation study was carried out that compared the efficiency of N-terminus modification in the two mutants. The N-terminus was modified with an α-lipoic acid moiety according to the reaction presented in Scheme 5.1. The choice of α-lipoic acid is due to the disulfide groups present in the molecule. Sulfur is known to strongly bind to gold, so the disulfides present in α-lipoic acid provide a chemical handle for attachment in preliminary work examining Flg-A3 AuNPs binding to conjugated TMV.

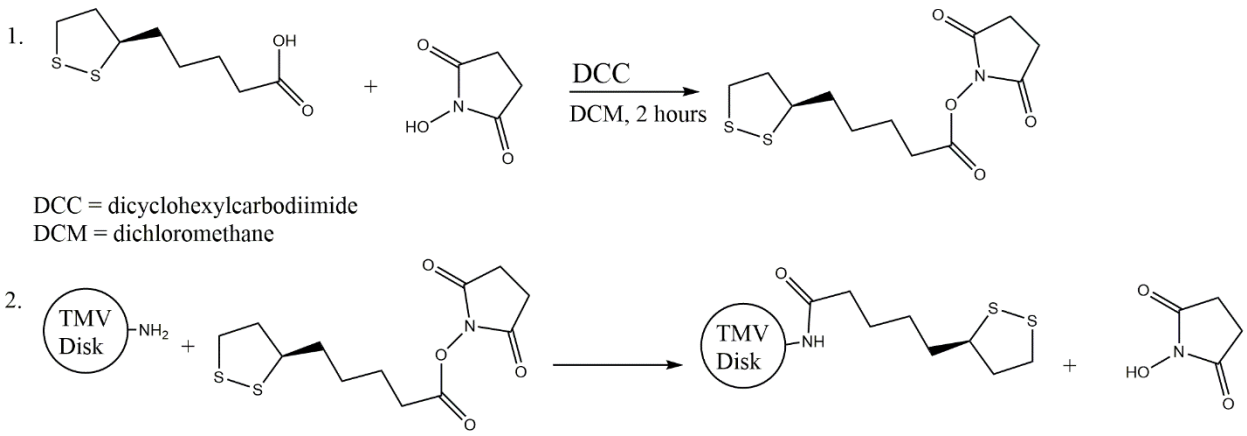

Scheme 5.1 Reaction scheme for the modification of the N-terminus of TMVcp with an α-lipoic acid moiety.

5.3 Experimental Methods

5.3.1 Materials

Flg-A3 peptide (≥ 90% purity) was purchased from BioBasic Canada (Ontario, Canada). All other materials were purchased from Sigma Aldrich (Ontario, Canada).

5.3.2 N-Lipoyloxy succinimide

2.4 mmol (0.5 g) of N,N'-dicyclohexylcarbodiimide (DCC) was dissolved in 3 mL of ice-cold anhydrous dichloromethane (DCM) under nitrogen. Meanwhile, 2.4 mmol (0.5g) of α-lipoic acid and 2 mmol (0.23 g) of N-hydroxy succinimide (NHS) were dissolved in 4 ml of ice cold, anhydrous DCM under nitrogen. The DCC solution was added dropwise to the NHS/α-lipoic acid solution and the reaction was stirred for two hours at room temperature under nitrogen until a pale yellow precipitate had formed. The reaction flask was then left at 4 °C overnight in order to precipitate the dicyclohexyl urea (DCU) side product. A white precipitate was removed via vacuum filtration and a transparent yellow solution was recovered. The solvent was removed by rotary evaporation at room temperature and a yellow solid was obtained. This solid was washed with several portions of ice cold diethyl ether before being collected via vacuum filtration. At this point the precipitate was pale-yellow in colour.

5.3.3 TMV Expression

All mutants of the TMVcp were expressed according to a procedure previously described by Zahr et al.[11].

5.3.4 TMV Conjugation

Tobacco mosaic virus was dialysed into the appropriate buffer for conjugation (Table 5.1) at 4 °C overnight. Once dialysis was completed the resulting solution was passed through a 0.2 μm sterile syringe filter and a UV/VIS spectrum was collected in order to determine the protein concentration using a disposable plastic cuvette with pathlength 1 cm. The resulting TMV solution was then spiked with a 10 mM α-lipoic acid NHS ester so that the ratio of ester to TMV was 20 to 1 and left to incubate overnight at room temperature. For the SAG TMVcp mutant

two other additions of ester were performed maintaining the same ester to TMV ratio. The second addition was performed after the overnight incubation and left to react for 8 hours. The last ester addition was then added and the SAG TMVcp was left to incubate overnight. Following this dithiothreitol (DTT) was added to the conjugated protein so that the final concentration was 10 mM and left to incubate overnight. The conjugated TMV was then passed through a 7 kDa MWCO spin filtration column via centrifugation at 2 000 rpm for 2 minutes in order to remove impurities. The reaction yield was characterized by electrospray ionisation mass spectroscopy (ESI-MS).

Table 5.1 Conditions Tested for TMVcp Conjugation

pH	Buffer type	Concentration (mM)	NaCl Concentration (mM)
7	Phosphate	24	N/A
8.3	Carbonate	100	N/A
8.3	Carbonate	100	400

5.3.5 Gold Nanoparticle Binding Experiments

Flg-A3 gold nanoparticles were synthesized according to protocols described elsewhere[18,19]. The resulting nanoparticles were transferred to the respective buffer for AuNP binding (Table 5.2) via centrifugation. 5 ml of the nanoparticle suspension was concentrated to approximately 250 μL via centrifugation using a Sorvall SC6 Plus centrifuge and the SH-3000 swinging bucket rotor for 30 minutes at 3 000 Gs. The nanoparticles were concentrated with 3.5 kDa MWCO centrifugal filters (Pall Life Sciences, Port Washington, NY). The resulting concentrate was washed three times with 5 ml portions of buffer used for gold nanoparticle binding (Table 5.2) via centrifugation at 3 000 Gs for 30 minutes each time. After the washing step, the nanoparticles had been concentrated to approximately 250 μL. The volume was adjusted to 500 μL using the buffer being used for binding conditions (Table 5.2).

Table 5.2 AuNP Binding Conditions Tested

pH	Buffer type	Concentration (mM)	NaCl Concentration (mM)	Ionic strength (mM)
7	Phosphate	24	N/A	50
7	Phosphate	24	150	200
7	Phosphate	24	200	250
7	Phosphate	24	250	300

The concentrated nanoparticle suspension was spiked with the conjugated SAG TMV mutant so that the ratio of AuNP to TMV was 2 to 1. The mixture was then left to incubate three days at room temperature. The AuNPs were characterized by transmission electron microscopy (TEM) in a Tecnai T12 120 kV TEM using 400 mesh copper grids (Canemco, Gore, QC).

The rings in phosphate buffer (pH 7, 24 mM, 250 mM NaCl) were purified by sonication for 1 minute to break up aggregates. This was followed by passing them through a 0.2 μm spin filter (Pall Life Sciences, Port Washington, NY) and centrifuging them for 1 minute at 6 000 rpms to further remove AuNP aggregates. The resulting solution was then passed through a 300 k MWCO membrane (Pall Life Sciences, Port Washington, NY) by centrifuging it for 1 minute at 6 000 rpms. This reduced the volume to approximately 250 μL. This step was repeated and the rings were washed with 250 μL portions of phosphate buffer (24 mM, pH 7, 250 mM NaCl) until the resulting solution was colourless. This required about 5 washings. The volume was adjusted to 500 μL with phosphate buffer (24 mM, pH 7, 250 mM NaCl). The AuNPs were characterized by transmission electron microscopy (TEM) in a Tecnai T12 120 kV TEM using 400 mesh copper grids (Canemco, Gore, QC).

5.4 Results and Discussion

α-lipoic acid was chosen to modify the N terminus because of the ability of the sulfur atoms in the molecule to bind covalently to gold, which is necessary to modify the N terminus of

TMVcp disk with gold nanoparticles. DCC coupling was used to synthesize α-lipoyloxy succinimide which would in turn be used to react with the N terminus of the protein. Since this reaction is typically done in organic solvents due to DCC being water insoluble, the risk of hydrolysis of the α-lipoyloxy succinimide is minimal[16]. The dicyclohexyl urea, which is a side product, is readily removed from the reaction by vacuum filtration, as it is insoluble in dichloromethane, the solvent chosen for the DCC coupling step. Furthermore, the resulting ester is relatively stable long term if it is stored under proper conditions. ^{1}H and ^{13}C nuclear magnetic resonance spectroscopy data (NMR) for the DCC coupling step was in good agreement with previously published reports for the same compound and confirmed that the reaction was successful[20,21].

The ester is expected to react with primary amines because of their nucleophilic character to form a stable amide linkage. Primary amines are found both at the N-terminus and in lysine residues (which are present in TMVcp) [22]. There are two main lysine residues that are of concern which are at the 53 and 68 positions (Figure 5.3). Of these two, Lys 68 is known to be more reactive. However when TMVcp is in its assembled rod state, this lysine is not as reactive as the N terminus, which is a serine residue[23,24]. This is because the lysine is buried deep within the rod and consequently it is sterically hindered[23]. The relative conjugation efficiencies for the 20S disk is not as well understood though it is expected that these two lysine residues are also sterically hindered in this particular configuration.

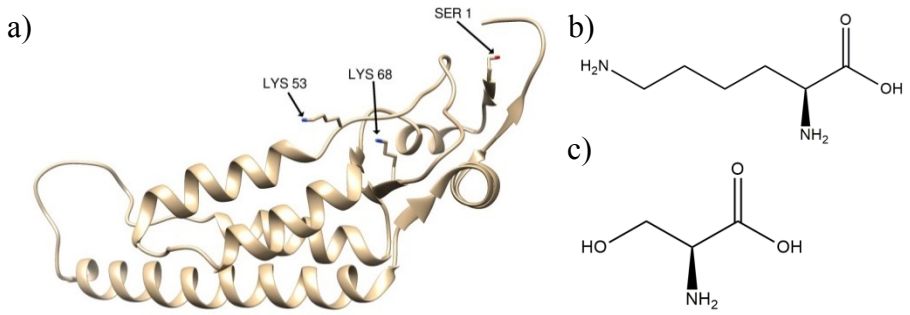

Figure 5.3 a) Structure of TMVcp displaying the amino acid residues with primary amines available for reaction with an NHS ester. Structures of b) lysine and c) serine.

Initially, an attempt was made to conjugate the S123C TMV, as it favours the disk phase which is the desired assembly for this work. Despite changes in pH and ionic strength that are known to cause wild type TMVcp (WT-TMVcp) to form various assemblies, S123C TMV is known to prefer the disk phase. Typically the conjugation reaction with the α-lipoyloxy succinimide is favoured at higher pH, however, the ester also hydrolyzes faster under these conditions[16]. Nevertheless, the conjugation was studied as a function of pH to determine the optimal pH to carry out the conjugation. In all cases, a ratio of 20 esters to 1 TMV was used for the conjugation. Liquid chromatography-mass spectroscopy (LC-MS) was used to quantify the success of the reaction (Figure 5.4). Both the high performance liquid chromatogram (HPLC) and electrospray ionisation mass spectra are presented.

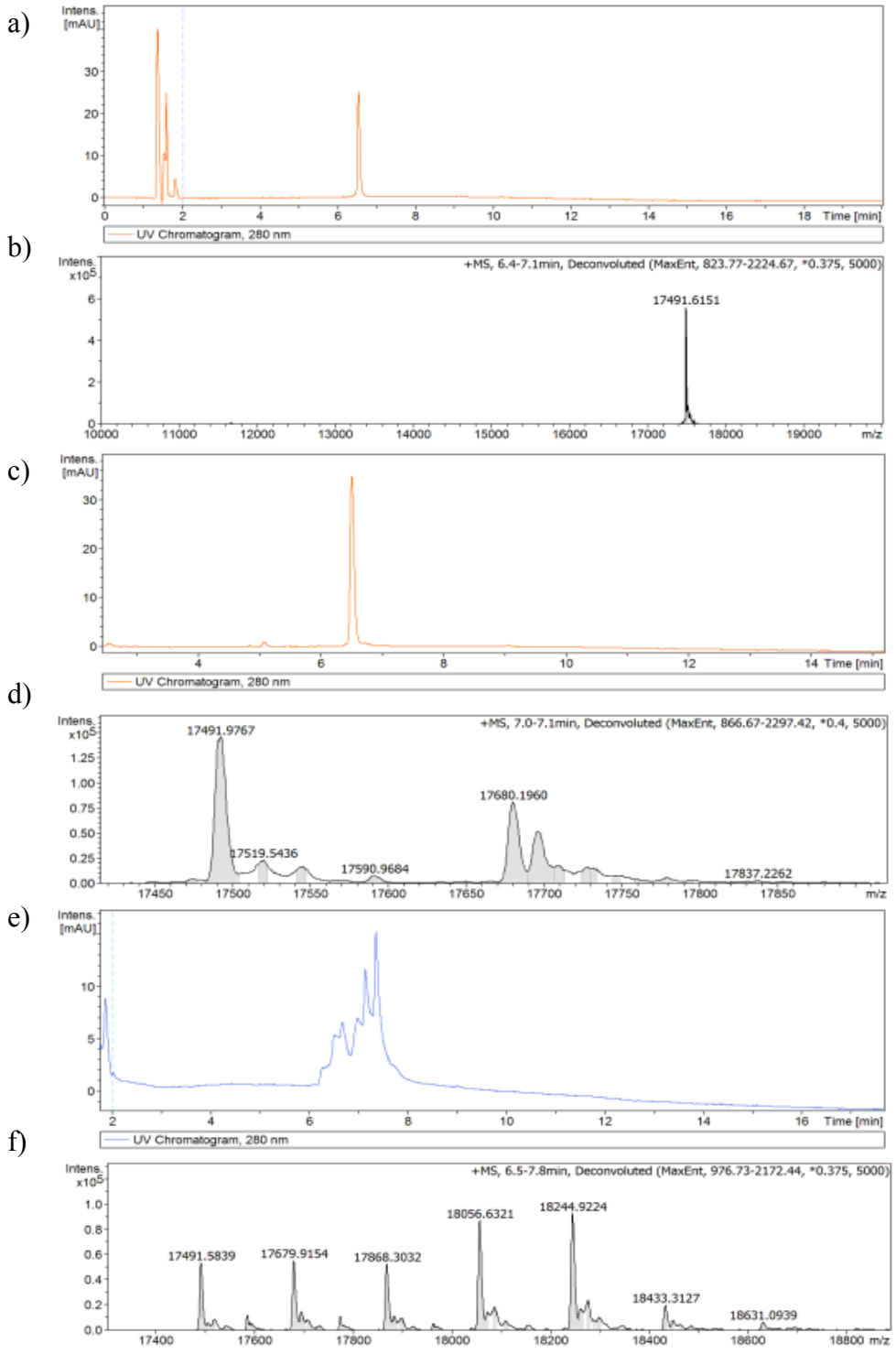

Figure 5.4 a) HPLC and b) ESI-MS for unconjugated S123C TMVcp. c) HPLC and ESI-MS for the conjugation of S123C TMVcp carried out in phosphate buffer (24 mM, pH 7). e) HPLC and f) ESI-MS for the conjugation of S123C TMVcp in carbonate buffer (0.1 M, pH 8.3).

In the HPLC, S123C TMV typically elutes between 6 and 7 minutes (Figure 5.4a). Correlating this peak with the ESI-MS data reveals that the protein has a molar mass of 17 492 g/mol (Figure 5.4b). If the conjugation is successful, it is expected that this should increase by 188 g/mol, which correlates with the molar mass of the α-lipoic acid moiety when bound to the disk. Examining the data for the conjugation run at pH 7, the TMVcp appears to elute at the same point as it does when it is not conjugated (Figure 5.4c). There are two peaks present in mass spectrum, one at 17 492 g/mol, which corresponds to unreacted TMVcp, and one at 17 680 g/mol (Figure 5.4d). The latter is larger than the peak for unconjugated TMVcp by 188 g/mol, which suggests that this peak can be attributed to conjugated TMVcp. The intensity of this peak, though, is much smaller than that of the unconjugated one. This suggests that the conjugation efficiency at pH 7 is quite poor.

The conjugation was also studied at pH 8.3. At this particular pH, the reaction is expected to proceed readily due to the increased nucleophilic character of the N terminus. Above the pK_a of the N terminus, which is 8.0, it is expected that the primary amine exists mainly in its unprotonated form, which is highly desirable for a reaction with α-lipoyloxy succinimide. Furthermore, the pH is still low enough that it favours the reaction of the N terminus over that of the primary amine side group present in lysines which have a pK_a of 10.5[25]. In the HPLC, the TMVcp (Figure 5.4e) eluted at a similar position when compared to that of unconjugated TMVcp (Figure 5.4a). However, there were multiple peaks present. Examination of the ESI-MS data (Figure 5.4f) suggests that multiple residues on the protein had been modified with the α-lipoic acid moiety.

The peak that had been previously attributed to unconjugated TMVcp (17 492 g/mol) is present, as is one for the conjugated form (17 680 g/mol). However, there are also several peaks

with higher molecular weight. The difference between these peaks and that of unconjugated protein are multiples of 188 g/mol, indicating that multiple sites on the TMVcp were conjugated with the α-lipoic acid moiety. The data suggests that as many as 6 sites were modified.

Above the anomalous pKa of the carboxylic acids present in TMVcp, which is 7.2, there is an increase in electrostatic repulsion which destabilizes TMV assemblies[10]. We therefore hypothesize that at the higher pH, the disk may be disassembled into the subunit, thus making the Lys 53 and Lys 68 residues more available for reaction. As the Lys 68 is the most reactive residue, it is believed that the α-lipoyloxy succinimide first reacts with this particular amino acid, which induces a change in the folding of the protein. It has been previously demonstrated that if this residue is modified it is difficult for the TMV to assemble back into the rod state[23]. This unfolding in turn makes the Lys 53 more reactive. If these two residues react in addition to the N terminus, then that makes for a triple conjugate which is observed. Furthermore, at this pH the thiol residue present in the cysteine is significantly more nucleophilic in nature as its pK_a is 8.00 thus making it capable of reaction with α-lipoyloxy succinimide to form a thioester. The additional conjugates may be due to the conjugation of hydroxyl groups in the protein which are also known to react with NHS esters to form ester linkages[22].

At pH 8.3, the conjugated forms of TMVcp are in higher yield than the unconjugated form indicating that while there were many unwanted forms of TMVcp where multiple sites were conjugated, the reaction is much more efficient here. One possible solution to minimize the reaction of the lysines that in turn lead to unfolding of the protein is to run the conjugation at higher ionic strength. This is to minimize the effect of the electrostatic repulsions that destabilize the TMV assemblies and likely leave the Lys 68 residue more exposed.

Consequently the conjugation was also run in carbonate buffer (0.1 M, pH 8.3, 0.4 M NaCl). The reaction was characterized by LC-MS (Figure 5.5)

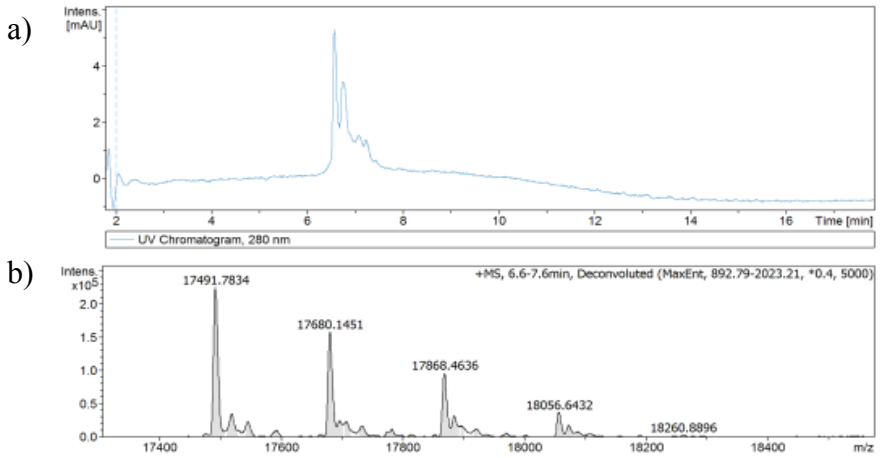

Figure 5.5 a) HPLC and b) ESI-MS for the conjugation of TMVcp in carbonate buffer (0.1 M, pH 8.3, 0.4 M NaCl)

Examination of Figure 5.5b reveals a significant reduction in the amount of multiple conjugates present. Under these particular conditions, the singly-conjugated form is in the highest yield compared to the others. However there is still a significant amount of double and triple-conjugated TMVcp present, indicating that raising the ionic strength is not enough to prevent unwanted conjugation of the lysine residues. Furthermore, there is still a significant amount of unconjugated TMVcp present which is highly undesirable.

The α-lipoyloxy succinimide is known to be quite reactive under the reaction conditions studied, so it seems that there are other factors contributing to the poor conjugation efficiency. One possible explanation is in the structure of the 20S disk, which is the preferred conformation of the S123C mutant being studied. Examination of this particular assembly using protein modeling software (Figure 5.6) reveals that the N terminus is sterically hindered by the C

terminus, thus explaining the low conjugation yields. One potential solution to this problem is to mutate the protein to make the N terminus more accessible.

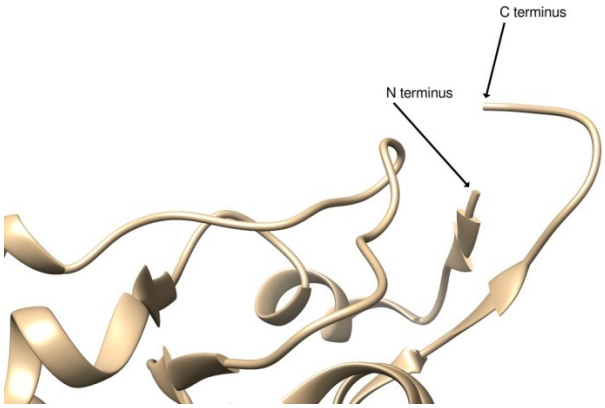

Figure 5.6 The N terminus in the S123C TMVcp mutant is sterically hindered by the C terminus thus reducing the conjugation efficiency.

In order to make the N terminus more reactive, three amino acid residues were added via genetic engineering of the TMVcp encoding plasmid. These were a serine, alanine and glycine residues. This mutant is referred to as the SAG TMV mutant. The alanine and glycine residues were selected because previous work has demonstrated that by adding them to the N terminus of TMVcp, the N terminus became more solvent accessible and was highly reactive in other bioconjugation schemes[26]. The serine was added as it is supposed to be more selective for N terminus conjugation[25]. With the addition of three extra amino acid residues, the N terminus is sticking out more in solution thus eliminating the steric hindrance. The conjugation of this new mutant was carried out according to the same protocols used for the S123C. The reaction was characterized by LC-MS (Figure 5.7). Owing to the fact that attempting to conjugate the S123C mutant at high pH resulted in a probable unfolding of the protein, only pH 7 was studied for conjugation in this instance.

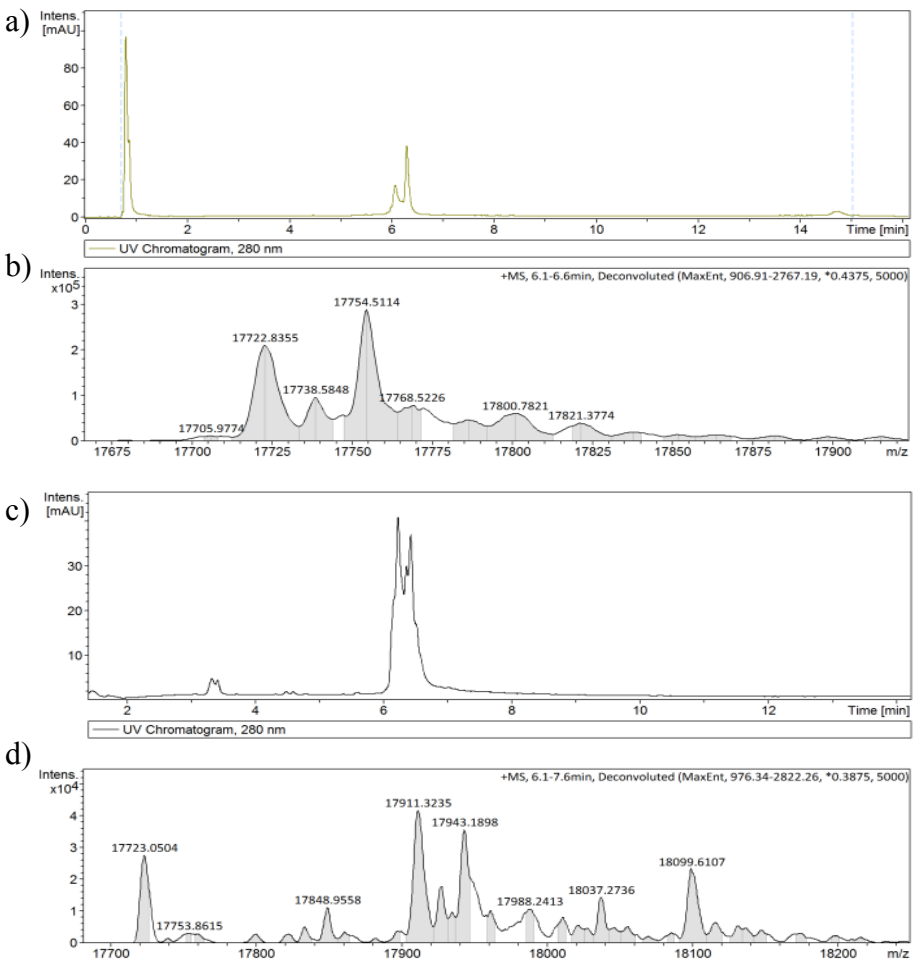

Figure 5.7 a) HPLC for SAG TMV in phosphate (pH 7, 24 mM) and b) ESI-MS for the same sample. c) HPLC for SAG TMVcp after one conjugation cycle in phosphate buffer (24 mM, pH 7) and d) ESI-MS for the same sample.

In Figure 5.7a the protein appears to elute between 6 and 6.5 minutes, which is similar to what was observed for S123C TMVcp. Further analysis of this peak reveals that unconjugated SAG TMV appears to have a molar mass of 17 723 g/mol which is in excellent agreement with the expected mass, indicating that the expressed protein is indeed the SAG TMVcp. The peak at 17 755 g/mol which is 32 units larger is likely the result of oxygen adduct formation in the MS. Upon addition of the α-lipoyloxy succinimide, we observe significant changes to the LC-MS. While the peak still elutes at approximately the same time, it appears to be broadened and contains two maxima. Further analysis of the mass spectrum reveals peaks at 17 723 g/mol and

17 754 g/mol, which accounts for the unconjugated TMVcp. There are two significant peaks, though, at 17 911 g/mol and 17 943 g/mol, which can be attributed to the conjugated TMVcp with and without oxygen bound to it. These peaks are 188 g/mol larger than the unconjugated peaks, indicating successful modification of the protein. These two peaks have a higher intensity than those attributed to unconjugated protein indicating a respectable reaction yield. There is also a peak at 18 099 g/mol. The difference between this peak and native SAG TMV (17 723 g/mol) is 376 g/mol which indicates that the protein might have been modified at two sites with α-lipoic acid moieties. Since the ester is known to hydrolyze in aqueous conditions[16] an additional two additions of α-lipoyloxy succinimide were done to increase the yield of conjugated TMVcp (Figure 5.8).

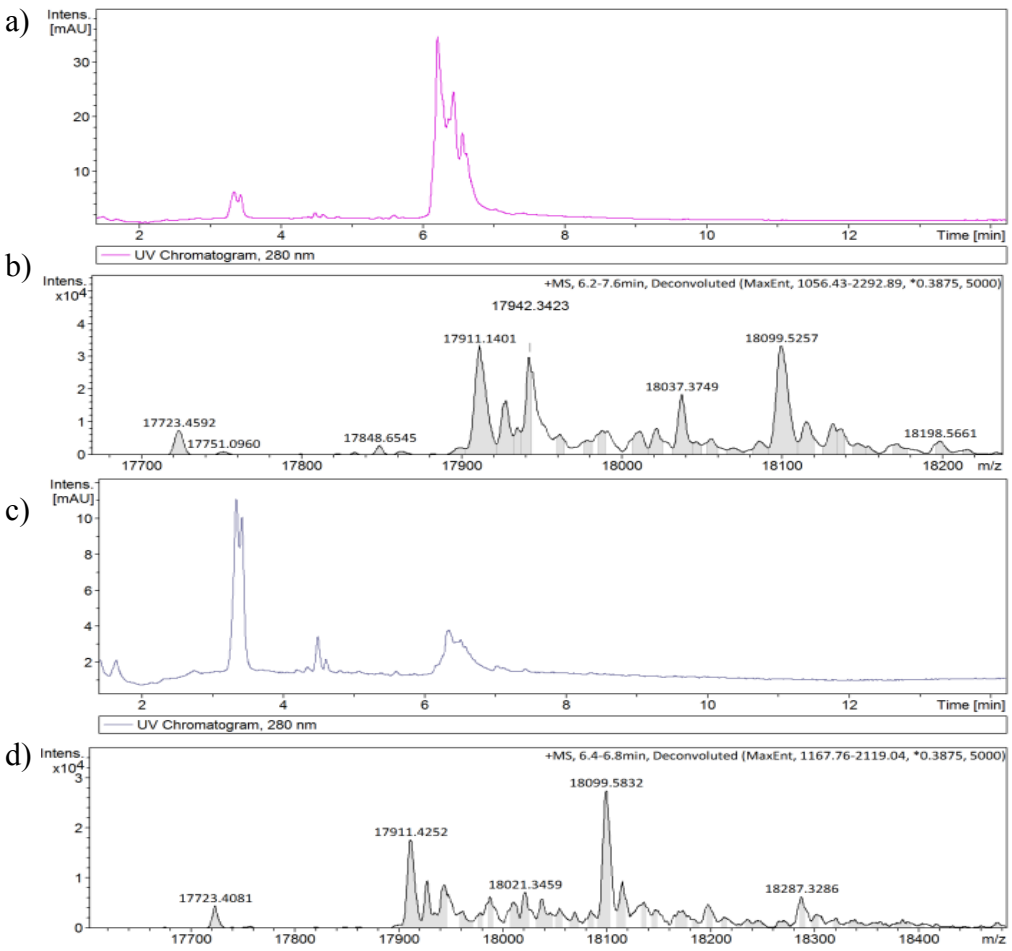

Figure 5.8 HPLC data for conjugated SAG TMVcp after a) a second and c) third ester addition. ESI-MS data for conjugated SAG TMVcp after b) a second ester addtion and d) third ester addition.

In the HPLC data (Figure 5.8a and c), the peak attributed to the protein appears to broaden with multiple ester additions. Examination of the ESI-MS data (Figure 5.8b and d) reveals that the peaks attributed to conjugated TMVcp (17 911 g/mol and 17 943 g/mol) appear to increase in intensity with multiple ester additions, while the peaks for unconjugated protein (17 723 g/mol and 17 755 g/mol) seem to diminish in intensity. After the third addition (Figure 5.8d) there seems to be almost no unmodified TMVcp present, indicating that with this particular mutant of the protein it is possible to completely conjugate all the protein within the limits of detection via MS.

One issue with the data in Figures 5.8b and d is that the double conjugate peak (18 099 g/mol) seems to be present in high yield in both cases. While it is possible that there may have been a reaction of the lysine residues it is also possible that the α-lipoyloxy succinimide reacted with a cysteine residue to form a thioester linkage. If the latter case is true than it should be possible to reduce the thioester with a reducing agent such as dithiothreitol (DTT) yielding only single conjugated TMVcp. The conjugated TMVcp was spiked with DTT so that its concentration was 10 mM and left to incubate overnight. Following this it was characterized with LC-MS (Figure 5.9).

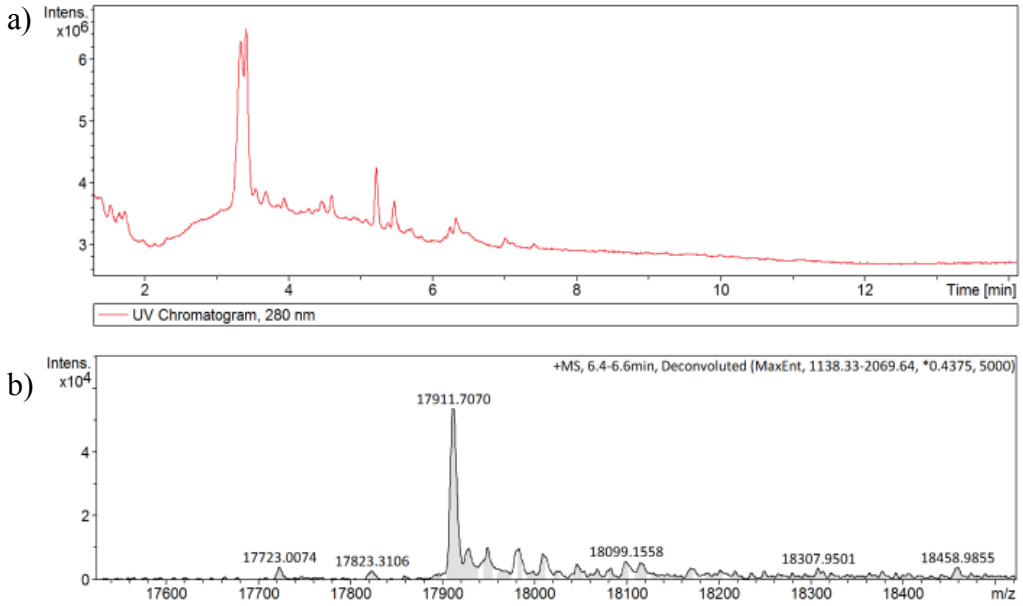

Figure 5.9 a) HPLC data for conjugated SAG TMVcp after treatment with DTT. b) ESI-MS data for conjugated SAG TMVcp after treatment with DTT.

In Figure 5.9a it is evident that the protein still elutes at approximately 6.5 minutes in the HPLC which is expected. Examination of the ESI-MS data (Figure 5.9b) reveals a peak at 17 911 g/mol which is the only significant one present. This suggests that the double conjugate was a result of the α-lipoyloxy succinimide forming a thioester linkage with cysteine. Treatment with DTT removed this giving only single conjugated TMVcp in high yield.

With the α-lipoic acid conjugated TMVcp now available, an attempt was made to use this viral protein template to bind gold nanoparticles for possible use in molecular electronic applications. In Chapter 3, Flg-A3 AuNPs were shown to be capable of forming high-density aggregates on silicon dioxide surfaces. The size of these networks, though, was only a few hundred nanometres by a few hundred nanometres. Therefore Flg-A3 AuNPs were examined for their ability of forming Flg-A3 AuNP rings using conjugated TMVcp disks with the hopes of eventually being able to form large-scale aggregates with the rings akin to what was made in Chapter 4. It is suspected that since the Flg-A3 gold nanoparticles are overall negatively charged that they will experience a great deal of electrostatic repulsion with the TMVcp that is also negatively charged. For this reason, the gold nanoparticle binding was studied as a function of ionic strength. In order to accomplish this, concentrated solutions of Flg-A3 AuNPs were spiked with conjugated TMVcp and left to incubate for 3 days. After synthesis, the nanoparticles were transferred to phosphate buffer (24 mM, pH 7) and sodium chloride was added if necessary to control the ionic strength. The gold nanorings were characterized by transmission electron microscopy (TEM) (Figure 5.10).

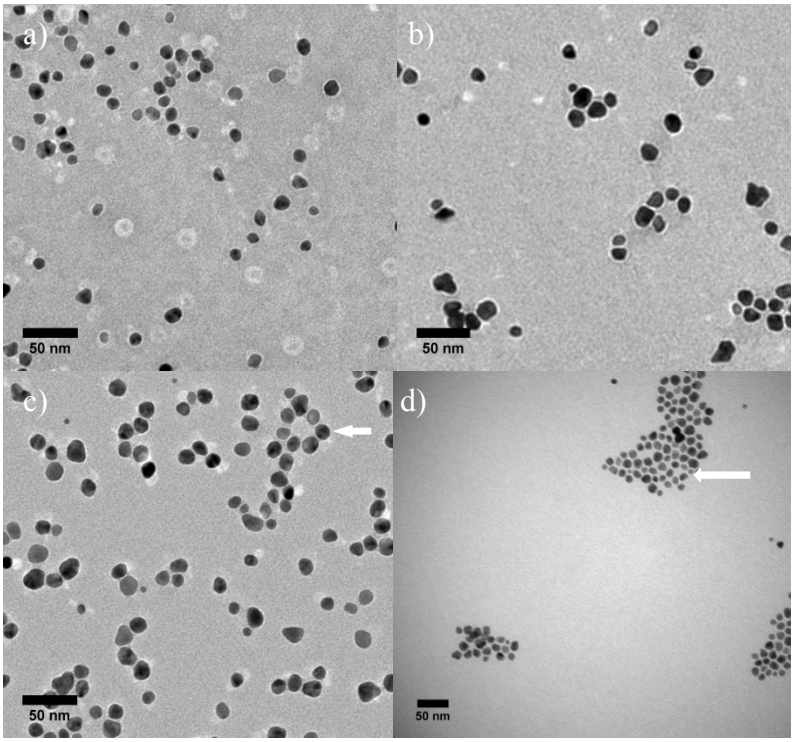

Figure 5.10 TEM micrographs of Flg-A3 AuNPS and TMVcp in a) phosphate buffer (24 mM, pH 7, $[I^-]$ = 50 mM), b) phosphate buffer (24 mM, pH 7, 150 mM NaCl, $[I^-]$ = 200 mM), c) phosphate buffer (24 mM, pH 7, 200 mM NaCl, $[I^-]$ = 250 mM) and d) phosphate buffer (24 mM, pH 7, 250 mM NaCl, $[I^-]$ = 300 mM). The arrows in c) and d) point to rings.

At low ionic strengths it appears that the AuNPs do not bind to the outer edge of the TMV (Figure 5.10a). The white disks with an inner pore are the TMVcp, and there seems to be no signs of AuNP binding. Adjusting the total ionic strength to 200 mM still does not lead to ring formation (Figure 5.10b). At ionic strengths above 250 mM, it appears that rings start to form (Figure 5.10c and d). The high ionic strength of the buffer was necessary to minimize electrostatic repulsion between Flg-A3 AuNPs and the TMVcp, both of which are negatively charged. Closer examination of the areas highlighted in Figure 5.7c and d reveal ring-like structures with an inner pore of approximately 18 nm, which suggests there is sufficient charge screening to overcome the electrostatic repulsion experienced between the AuNPs and the

TMVcp. Since there were reproducibility issues at a total ionic strength of 250 mM, 300 mM was chosen as the total ionic strength for subsequent experiments.

In order for ring-binding to occur, the AuNPs must be in excess when compared to the TMV. The optimal ratio for ring formation was found to be 2 AuNPs to 1 TMVcp. As a consequence of the excess amount of AuNP present, there is a significant amount of free nanoparticles left after ring formation. It is therefore necessary to remove them and purify the rings before any further experiments can be done with them. This was readily achieved via centrifugal filtration. The ring solution was passed through a filter with a 300K MWCO until it was colourless. The rings were further characterized by TEM (Figure 5.11).

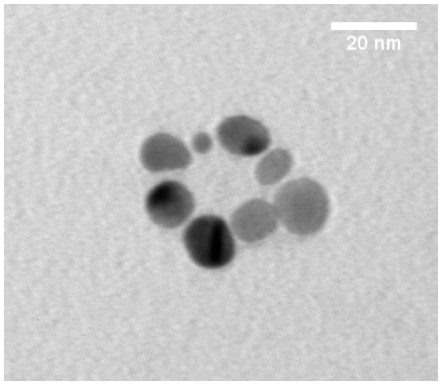

Figure 5.11 TEM micrograph for Flg-A3 AuNPs covalently bound to SAG TMVcp.

In some cases, as in Figure 5.11, the inner diameter is slightly less than 18 nm. Instead, it is on the order of 16 to 17 nm. The likely explanation for this is that the extended N terminus allows the nanoparticle some positional flexibility. There are 6 ± 1 AuNPs per ring and their separation is 2.0 ± 0.5 nm which is ideal for molecular electronics applications. The separation is small enough that conducting molecules could hypothetically bind between neighbouring nanoparticles. One issue though is that the yield is quite low and before these rings can be characterized further the yield must be increased.

5.5 Conclusions

The 20S disk phase of the tobacco mosaic virus coat protein was studied for its ability to serve as a template for the self-assembly of Flg-A3 gold nanoparticles. The N terminus was modified to contain an α-lipoic acid moiety which is expected to bind gold strongly. Originally, a cysteine containing mutant of the TMVcp was selected due to its preference for the disk phase, however in this conformation the N terminus is not readily accessible for conjugation so low yields were obtained. When three extra amino acid residues were added to the N terminus, the yield improved significantly. Following this it was possible to covalently bind Flg-A3 AuNPs to the circumference of the disk under conditions of high ionic strength to form rings, however at present the yield is quite low.

5.6 References

(1) Conklin, D.; Nanayakkara, S.; Park, T.-H.; Lagadec, M. F.; Stecher, J. T.; Therien, M. J.; Bonnell, D. a. *Nano Lett.* **2012**, *12* (5), 2414–2419.
(2) Conklin, D.; Nanayakkara, S.; Park, T.-H.; Lagadec, M. F.; Stecher, J. T.; Chen, X.; Therien, M. J.; Bonnell, D. a. *ACS Nano* **2013**, *7* (5), 4479–4486.
(3) Joanis, P.; Tie, M.; Dhirani, A.-A. *Langmuir* **2013**, *29* (4), 1264–1272.
(4) Asbahi, M.; Lim, K. T. P.; Wang, F.; Duan, H.; Thiyagarajah, N.; Ng, V.; Yang, J. K. W. *Langmuir* **2012**, *28* (49), 16782–16787.
(5) Schaal, P. a; Besmehn, A.; Maynicke, E.; Noyong, M.; Beschoten, B.; Simon, U. *Langmuir* **2012**, *28* (5), 2448–2454.
(6) Wnuk, J. D.; Rosenberg, S. G.; Gorham, J. M.; van Dorp, W. F.; Hagen, C. W.; Fairbrother, D. H. *Surf. Sci.* **2011**, *605* (3-4), 257–266.
(7) Sarikaya, M.; Tamerler, C.; Jen, A. *Nat. Mater.* **2003**, *2* (9), 577–585.
(8) Atanasova, P.; Stitz, N.; Sanctis, S.; Maurer, J. H. M.; Hoffmann, R. C.; Eiben, S.; Jeske, H.; Schneider, J. J.; Bill, J. *Langmuir* **2015**, *31* (13), 3897–3903.
(9) Kraft, D. J.; Kegel, W. K.; van der Schoot, P. *Biophys. J.* **2012**, *102* (12), 2845–2855.
(10) Kegel, W. K.; van der Schoot, P. *Biophys. J.* **2006**, *91* (4), 1501–1512.
(11) Zahr, O. K.; Blum, A. S. *Nano Lett.* **2012**, *12* (2), 629–633.
(12) Dedeo, M. T.; Duderstadt, K. E.; Berger, J. M.; Francis, M. B. *Nano Lett.* **2010**, *10* (1), 181–186.
(13) Geiger, F. C.; Eber, F. J.; Eiben, S.; Mueller, A.; Jeske, H.; Spatz, J. P.; Wege, C. *Nanoscale* **2013**, *5* (9), 3808–3816.
(14) Khan, A. a; Fox, E. K.; Górzny, M. Ł.; Nikulina, E.; Brougham, D. F.; Wege, C.; Bittner, A. M. *Langmuir* **2013**, *29* (7), 2094–2098.
(15) Brown, A. D.; Naves, L.; Wang, X.; Ghodssi, R.; Culver, J. N. *Biomacromolecules* **2013**,

14 (9), 3123–3129.
(16) Hermanson, G. T. In *Bioconjugate Techniques*; Academic Press: Amsterdam, 2008; pp 214–233.
(17) Miller, R. a; Presley, A. D.; Francis, M. B. *J. Am. Chem. Soc.* **2007**, *129* (11), 3104–3109.
(18) Slocik, J. M.; Naik, R. R. *Adv. Mater.* **2006**, *18* (15), 1988–1992.
(19) Del Re, J.; Blum, A. S. *Appl. Surf. Sci.* **2014**, *296*, 24–30.
(20) Capehart, S. L.; Elsohly, A. M.; Obermeyer, A. C.; Francis, M. B. *Bioconjug. Chem.* **2014**, *25* (10), 1888–1892.
(21) Chhabra, R.; Sharma, J.; Wang, H.; Zou, S.; Lin, S.; Yan, H.; Lindsay, S.; Liu, Y. *Nanotechnology* **2009**, *20* (48), 485201.
(22) Hermanson, G. T. In *Bioconjugate Techniques*; Academic Press: Amsterdam, 2008; pp 169–212.
(23) Perham, R. N.; Richards, F. M. *J. Mol. Biol.* **1968**, *33* (3), 795–807.
(24) Gallwitz, U.; King, L.; Perham, R. N. *J. Mol. Biol.* **1974**, *87* (2), 257–264.
(25) Wetzel, R.; Halualani, R.; Stults, J. T.; Quan, C. *Bioconjug. Chem.* **1990**, *1* (2), 114–122.
(26) Scheck, R. a.; Dedeo, M. T.; Iavarone, A. T.; Francis, M. B. *J. Am. Chem. Soc.* **2008**, *130* (35), 11762–11770.

6 Constructing Molecular Networks from Densely Packed Networks of Peptide-Coated Gold Nanoparticles and Molecular Wires

6.1 Preface

In this chapter the Flg-A3 gold nanoparticle films developed in Chapter 4 were made using silicon dioxide substrates with lithographically defined gold electrodes with the hopes of being able to integrate OPV into them and form a molecular circuit. Following film formation the samples were treated with ultraviolet ozone cleaning to remove the peptide used to form them in order to leave bare gold nanoparticles on the surface thus facilitating device formation. Surface enhanced Raman spectroscopy confirmed peptide removal and SEM confirmed that while some sample damage occurred large areas of the film did not show a significant change in nanoparticle size. Electrical measurements were inconclusive though indicating further work is required.

6.2 Introduction

Gold nanoparticle (AuNP) networks are an attractive area of research as their nanoscale features and interesting optical and electronic properties render them useful in a wide variety of applications such as molecular electronics[1], surfaced enhanced Raman spectroscopy (SERS)[2] and photovoltaics[3]. A common approach to form these networks is to deposit the AuNPs from solution as this method is quite simple[4]. The other advantage is that by first synthesizing the nanoparticles in solution it is possible to gain excellent control over the final size and shape of the nanoparticle[5]. In order to harness the full power of the gold nanoparticles though the ligand that was stabilizing them in solution needs to be removed to expose the gold surface. A variety of surface treatments are available to strip the ligand off the nanoparticle such as solvent

extraction[6], plasma treatment[7] and chemical and thermal treatment[8,9] however these methods tend to cause an increase in the size of the nanoparticles.

One method that has not been explored extensively for gold nanoparticles is the use of ultraviolet ozone cleaning. In this method ultraviolet light reacts with diatomic oxygen to form ozone which then oxidizes organic molecules into products such as water, carbon dioxide and nitrogen[10]. This method has been used extensively to pretreat planar gold surfaces prior to thin film deposition[11–13]. Moreover, previous work has demonstrated that UV ozone cleaning can be used to remove the stabilizing ligands from surface-tethered platinum[14] and palladium[15] nanoparticles. This makes it a very attractive option for ligand removal with gold nanoparticle films so that they can then be studied further for their use in molecular electronic applications.

While a vast amount of research has been done studying the electrical properties of single molecules for their use in molecular electronics applications there has been less work focusing on integrating them into functional molecular circuits. One proposed solution would be to use densely-packed gold nanoparticles to form networks between lithographically-defined gold electrodes on insulating surfaces as detailed in Figure 6.1. If the nanoparticles are spaced closely enough together then conducting molecules can hypothetically bridge the gap and electric current can flow through the device.

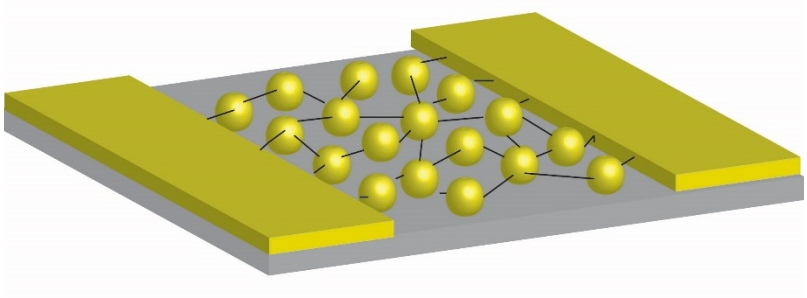

Figure 6.1 Networks of gold nanoparticles and conducting molecules sandwiched between gold electrodes is one proposed design for molecular electronic devices. Black lines represent molecular wires bridging the gap between neighbouring nanoparticles.

Oligophenylene vinylene (OPV) (Figure 6.2) is a well-characterized molecular wire frequently used in molecular electronic devices[16–18]. This is due to its planar π-conjugated structure and low degree of bond-length alteration which facilitates charge transport[19]. In Chapter 3 it was demonstrated that the electrical properties of OPV are sensitive to nitroaromatic analytes in the local environment. This is the result of a π donor-acceptor interaction between the molecule and the analyte. This proves that OPV might eventually be useful in a sensing device however it is first necessary to incorporate the wires into a functional device. As stated in the previous paragraph densely-packed networks of gold nanoparticles on insulating substrates would be ideal for this.

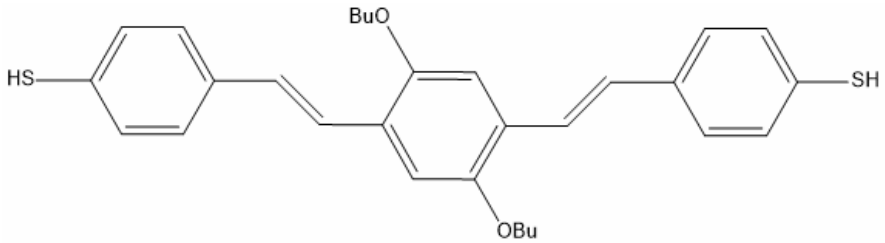

Figure 6.2 The structure of the OPV molecule studied.

Chapter 4 focused on the formation of densely-packed gold nanoparticle networks on silicon dioxide substrates. This was achieved using two different fusion peptide. The Flg-A3 peptide participates in the synthesis and stabilization of gold nanoparticles[20]. It also allows for

the formation of densely-packed nanoparticle aggregates as the peptide interacts with divalent metal ions such as Zn^{2+} to form solution-phase aggregates. These aggregates were shown to be capable of binding to silicon dioxide surfaces in high density because of the A3-QBP1 peptide which tethers them to the surface[4]. These networks were found to be sufficiently large to begin looking at using them to form molecular electronic devices.

The following work builds upon the foundation set in Chapters 3 and 4 to form a molecular electronic device. Molecular networks consisting of peptide-stabilized gold nanoparticles and OPV molecules were formed between gold electrodes on an insulating surface. A chip was made that consisted of lithographically-defined gold electrodes on a silicon dioxide substrate (Figure 6.3). Flg-A3 AuNP aggregates that had been formed with Zn^{2+} were deposited between the electrodes using the A3-QBP1 peptide to achieve high surface coverage. Prior to OPV insertion the gold nanoparticle films were treated with UV/ozone cleaning to remove the peptide leaving the surface of the nanoparticle exposed thus facilitating binding of the molecular wire.

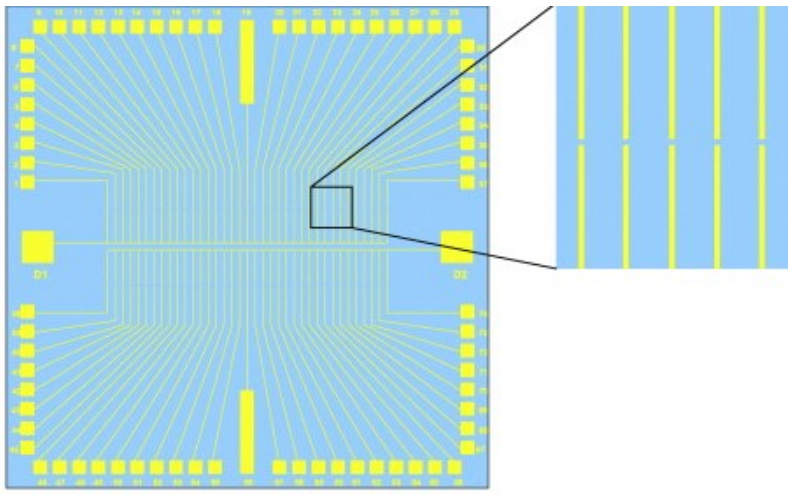

Figure 6.3 Illustration of the chip design used in this experiment. Reprinted with permission from Blum, A.S. et al., *Biosens. Bioelec.*, **2011**, 26 (6), 2852 - 2857. Copyright 2011. Elsevier.

6.3 Experimental Methods

6.3.1 Gold Nanoparticle Synthesis and Film Formation

Flg-A3 AuNPs were synthesized and characterized according to the methods employed in Chapter 4.

6.3.2 Surface Cleaning Experiments

Flg-A3 AuNP films was prepared by sonicating a silicon dioxide substrate 10 minutes in 2-propanol followed by cleaning it with RCA-1. After rinsing the substrates with deionized water and drying them with nitrogen gas 50 μL of A3-QBP1 (1 mg/ml in HEPES (100 mM, pH 7)) was deposited on the surface and the samples were left to incubate overnight at room temperature. They were then rinsed again with deionized water and dried with nitrogen. Following this 50 μL of Flg-A3 AuNPs/0.75 mM Zn^{2+} was plated on the surface and left to incubate overnight at room temperature. The samples were rinsed with deionized water and dried with nitrogen and characterized with a Bruker Senterra Raman microscope (Bruker, Billerica, MA) using a 532 nm laser. They were treated in a ZoneSEM UV/ozone cleaner for varying time frames after which they were rinsed with deionized water and ethanol. The samples were characterized again with Raman microscopy and FEI Inspect F50 scanning electron microscope (SEM).

6.3.3 Electrical Measurements

OPV was synthesized according to procedures described elsewhere[19].

The substrates used in this particular setup were fabricated on a silicon wafer containing a 1 μm thick layer of silicon dioxide. The larger parts of the structure were made by first writing the desired pattern in KRS, which is a positive tone high-contrast chemically amplified resist

based on ketal protecting groups[21]. A 500 nm layer of this resist was coated onto the wafer and baked at 120 °C for 60 s. The electron beam pattern was exposed in a Leica VB6 vector beam electron beam lithography tool using a current of 10 nA and a spot size of 40 nm. The sample was developed in 0.26 N tetramethylammonium hydroxide (TMAH) developer for 60 s and rinsed with deionized water before it was briefly exposed to an oxygen plasma to remove any resist scum. The wafer was coated with a 5 nm layer of Cr followed by a 55 nm layer of Au. The desired structures were then completed by soaking the wafer in n-methyl-2-pyrrolidone (NMP) at 60°C and using ultrasonic agitation to remove the un-exposed resist, completing the lift-off process.

These large structures had a 1.5 micron gap between electrodes which was narrowed to create finer structures. These structures were made by writing the pattern in poly(methyl methacrylate) (PMMA) resist. A 150 nm layer of PMMA was coated onto the wafer and baked for 180 s at 175 °C. Here a much smaller, 0.5 nA beam was used but required just two minutes per sample. The PMMA was developed in a 3:1 mixture of methyl isobutyl ketone (MIBK) and isopropanol for 60 s and rinsed in IPA. The sample was again briefly exposed to an oxygen plasma then placed in the evaporator and coated with a 5 nm layer of Cr followed by a 32 nm layer of Au. Soaking in hot NMP using ultrasonic agitation was again used to complete the lift-off process.

The substrate was sonicated 10 minutes in isopropanol to remove organic contaminants. The substrate was then treated with the RCA-1 cleaning. Following this 50 μL of A3-QBP1 (1 mg/ml in HEPES (100 mM, pH 7)) was deposited on the surface and the sample was left to incubate in a damp chamber at room temperature overnight. It was then rinsed with deionized water and dried with a gentle stream of nitrogen gas. 50 uL of Flg-A3 AuNPs/0.75 mM Zn^{2+}

solution was plated on the substrate and it was left to incubate at room temperature in a damp chamber overnight. It was then rinsed with deionized water and dried with nitrogen gas.

Substrates were characterized with SEM. Following this they were then treated with 30 minutes of UV/ozone cleaning and characterized again with SEM. Only junctions in which nanoparticle aggregates were observed to bridge the gap between electrodes were selected for further analysis. As a control one junction which did not contain any nanoparticles was also studied. I-V curves were collected for these junctions using a Keithley 4200-SCS Semiconductor Parameter Analyser.

Following this 2 mg of acetyl-protected OPV was dissolved in 4 ml tetrahydrofuran (THF) under nitrogen. 40 μL concentration ammonium hydroxide was added to the solution. The substrate was immersed in it and left to incubate at room temperature overnight. Upon removal from the solution it was rinsed vigorously with THF. It was then characterized with a Keithley 4200-SCS Semiconductor Characterization System.

6.4 Results and Discussion

Gold nanoparticle films were formed according to methods employed in Chapter 4. In order for ultraviolet ozone cleaning to be considered a suitable cleaning process for gold nanoparticle films it must be possible to retain the nanoscale features of the surface. This is particularly challenging when the nanoparticles are spaced closely together as it is easier for the nanoparticles to nucleate. Scanning electron microscopy (SEM) was used to characterize the nanoparticle films (Figure 6.4).

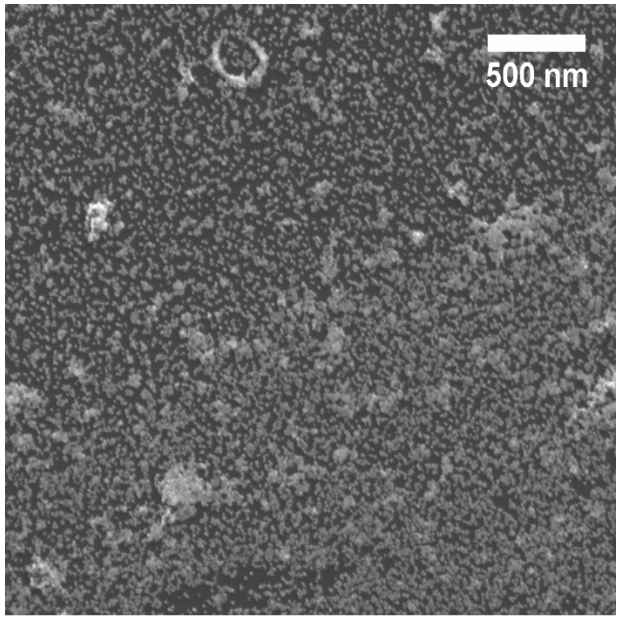

Figure 6.4 SEM micrograph for Flg-A3 AuNP films after 15 minutes of ultraviolet ozone cleaning.

Initially a total destruction of the gold nanoparticle film is observed after only 15 minutes of surface treatment (Figure 6.4). The most likely explanation for this that there was a heating of the nanoparticles which was causing them to melt. The source of the temperature increase could be attributed to heat being released during the oxidation process as this sort of reaction tends to be exothermic in nature. It is also possible that since the sample is directly in the path of the ultraviolet lamp irradiation with the lamp causes some heating. Since the gold nanoparticle films are plated on silicon dioxide which is insulating in nature the heat will not be transferred to the substrate from the nanoparticle causing them to heat up and consequently melt. Since the films would eventually be plated on silicon dioxide substrates containing gold electrodes which could conduct heat away from the nanoparticles gold contact pads were also plated on the substrates being used for the initial studies that studied removal of the Flg-A3 peptide using ultraviolet ozone cleaning. These contact pads had a 2 nm thick layer of Cr and 80 nm thick layer of Au and it was thought that if they were there they would conduct heat away from the nanoparticles

thus reducing or eliminating sample damage. The nanoparticle films were plated on substrates containing the contact pads and imaged in the SEM (Figure 6.5).

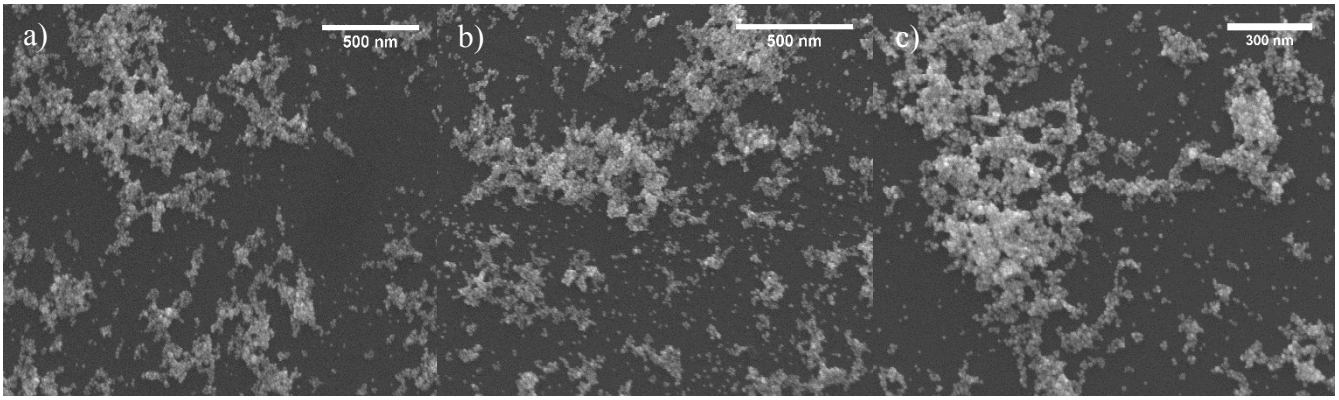

Figure 6.5 SEM micrographs for Flg-A3 AuNP films after ultraviolet ozone treatment for a) 30 minutes, b) 60 minutes and c) 120 minutes.

The SEM reveals that after thirty minutes in the ultraviolet ozone cleaner (Figure 6.5a) the nanoparticle film remains intact. After a total of one hour of surface treatment (Figure 6.5b) the nanoparticles appear to be more or less unchanged and can withstand as much as two hours (Figure 6.5c) without dramatic changes to the surface morphology. There were still areas of sample damage observed in all the films studied however there were also large areas of the surface where the nanoparticles remained unchanged. These areas tended to be closest to the contact pads which indicates that if heat can be transferred away from the nanoparticle the melting will not take place. This further confirms that the observed sample destruction in Figure 6.4 is a result of thermal effects.

Raman spectroscopy was used to track peptide removal. Prior to studying the gold nanoparticle films spectra were collected for both free Flg-A3 peptide and A3-QBP1 peptide to confirm the presence of Raman active modes (Figure 6.6, Table 6.1). Examination of Figure 6.6 reveals that both peptides contain Raman active modes which is due to the amino acids present in the peptide. For example in the Flg-A3 peptide (Figure 6.6a) there is a strong band present at

997.7 cm^{-1} which can be attributed to phenylalanine which is present in the peptide and known to exhibit a Raman active mode at this particular shift due to the aromatic ring present[22].

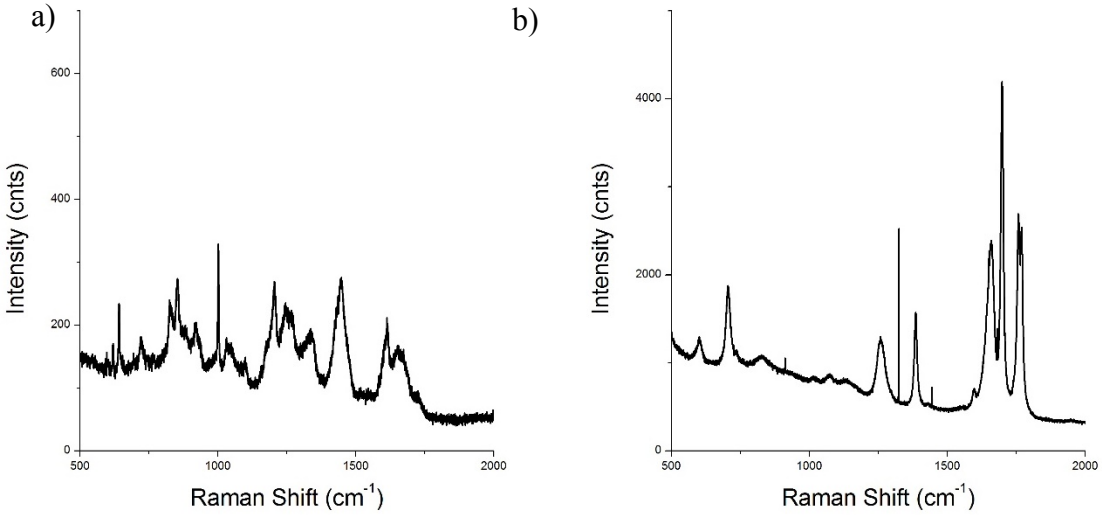

Figure 6.6 Raman spectra for a) free Flg-A3 peptide and b) free A3-QBP1 peptide.

Table 6.1 Raman Shifts for Free Flg-A3 and Free A3-QBP1 Peptide

Peptide	Raman Shift (cm^{-1})
A3-QBP1	601.1
	706.8
	1258.1
	1386.6
	1652.2
	1699.3
	1757.9
Flg-A3	641.8
	720.3
	825.2
	838
	853.8
	997.7
	1204.6
	1241.7
	1336
	1447.7
	1613

A surface enhanced Raman spectrum (SERS) was then collected for the gold nanoparticle film (Figure 6.7, Table 6.2) which had been prepared according to protocols described in Chapter 4. A 532 nm laser was used as this wavelength provides the best overlap with the surface plasmon resonance (SPR) band of the AuNPs which is 530 nm. This was done in order to achieve a SERS signal as without any enhancement from the SPR band there is too little peptide present on the film to be able to observe anything in the Raman spectrum. As evidenced in Figure 6.5 there is a dramatic SERS enhancement from the nanoparticle especially for what is thought to be the phenylalanine band at 1001.5 cm^{-1}. Certain bands do not have the same shift as they do in the free A3-QBP1 or Flg-A3 peptide (Table 6.1) however it is entirely possible that both these peptides adopt a different secondary structure in the AuNP film when compared to the free peptide. Secondary structure is known to play a role in Raman shifts[23].

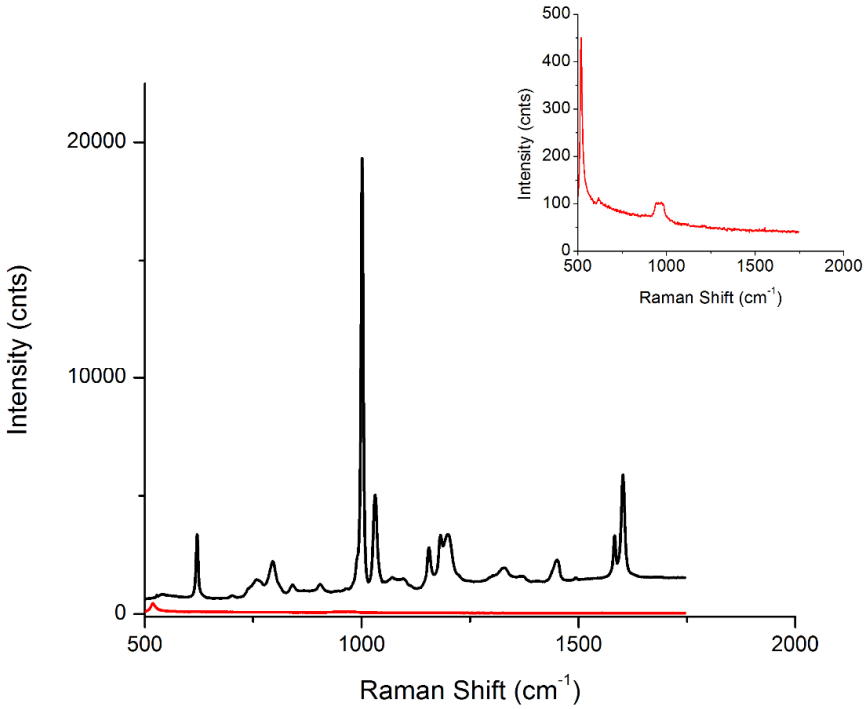

Figure 6.7 SERS spectra for Flg-A3 AuNP films on A3-QBP1-coated silicon dioxide before ozone cleaning (black) and after 30 minutes surface treatment (red). The inset is a blow-up of the SERS spectrum for the film after ozone cleaning.

Table 6.2 Raman Shifts for Flg-A3/A3-QBP1 AuNP Films

Peptide	Raman Shift (cm^{-1})
AuNP Film	620.5
	795.5
	1001.5
	1031.5
	1155
	1182
	1199.5
	1330
	1350
	1583.5
	1602.5

Preliminary Raman spectroscopy data was collected for the substrates treated with ultraviolet ozone cleaning. Following treatment of the substrate with UV/ozone and rinsing with deionized water and ethanol a Raman spectrum was collected using identical settings to the ones used for the initial spectrum (Figure 6.7). Examination of Figure 6.7 reveals that after 30 minutes the bands attributed to the nanoparticle films seem to have been entirely eliminated. Looking more closely at the obtained spectrum (Figure 6.7 inset) it is identical to the one observed for pure silicon[24]. The intense band at 520 cm^{-1} can be attributed to first order phonon scattering in silicon and the weak, broad one at 950 cm^{-1} can be assigned to a second order phonon scattering. Much further study is required though especially for shorter and longer cleaning times.

The nanoparticle films were then plated on silicon dioxide substrates which contained gold electrodes. The silicon dioxide layer was 1 μm thick to ensure no leakage current from the underlying silicon wafer. The gap between electrodes varied from as little as 20 nm to as much as 1 500 nm to determine the optimal separation for this particular system. The AuNP films were deposited on these substrates using the methods employed in Chapter 4. They were then

characterized with SEM to determine which junctions contained nanoparticles. Figure 6.8 represents a junction where densely packed nanoparticles had been observed bridging the gap between the electrodes. In this particular junction the electrode separation is 70 nm. Following characterization in the SEM the sample was treated for 30 minutes in an ultraviolet ozone cleaner. It was then imaged again in the SEM to confirm no sample damage had taken place.

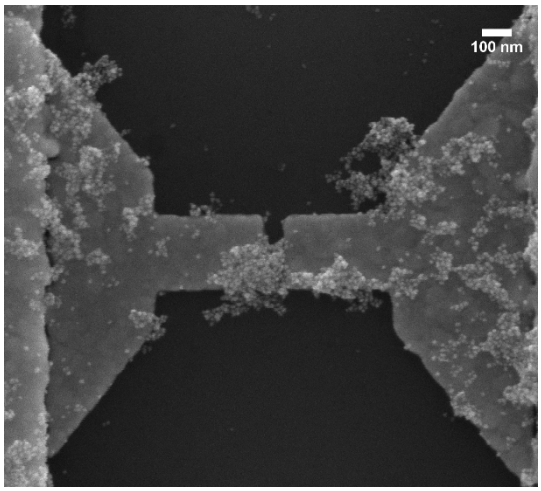

Figure 6.8 SEM micrograph of a junction where the electrode separation is 70 nm and densely-packed Flg-A3 AuNPs are bridging that separation.

Following identification of which gaps contained gold nanoparticles I-V curves were collected for these junctions. I-V curves were collected by sweeping the voltage from -0.5 V to 0.5 V (Figure 6.9). As a control measurement an I-V curve was always collected for a junction containing no nanoparticles. Following this control experiment the substrate was immersed in a 1 mM solution of OPV overnight to allow the molecule to bind between neighbouring gold nanoparticles. The procedure for collecting I-V curves was repeated.

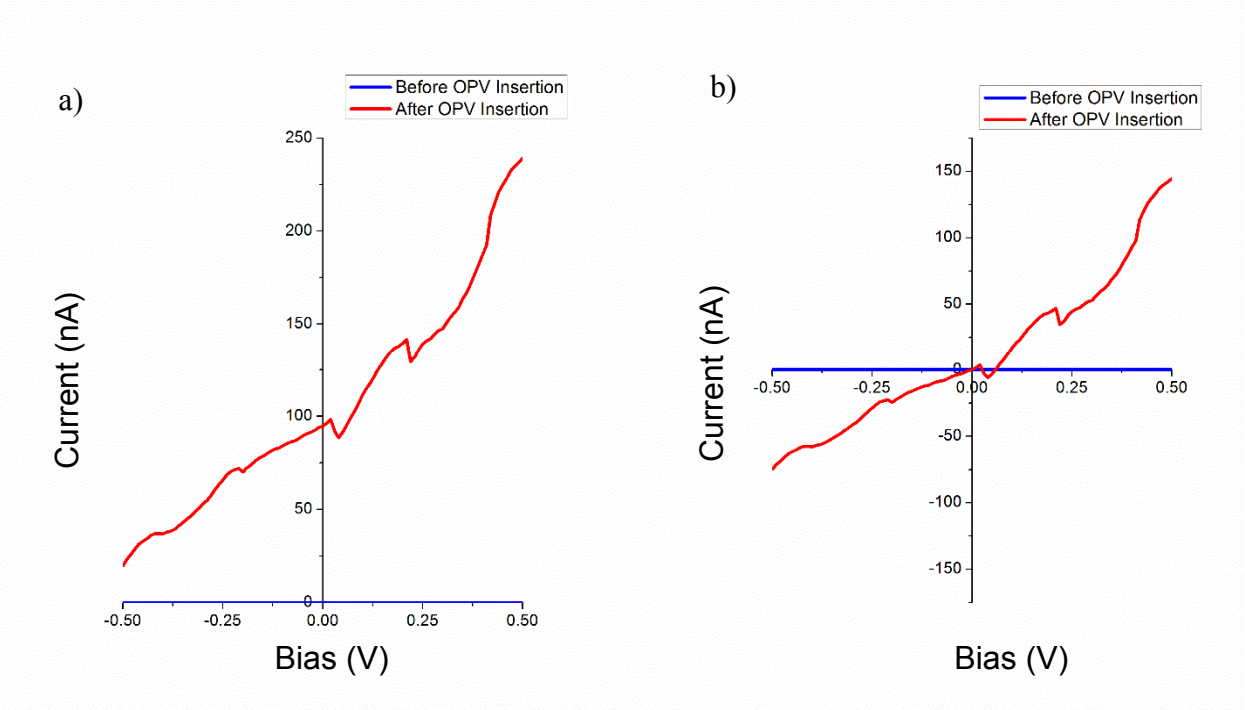

Figure 6.9 a) Raw I-V data for a 35 nm junction and b) corrected I-V data for the same junction.

Prior to OPV insertion there is no measurable current in the nanoparticle network (Figure 6.7a). The I-V curve appears to simply be baseline noise in the pA range. The control junction which contained no nanoparticles also behaved in a similar manner. Following exposure to OPV though the magnitude of the current seems to increase with increasing bias (Figure 6.9a). The curve is somewhat linear in nature with small decreases in current observed around 0.05 V and 0.25 V. The source of these current drops is unknown. Were the nanoparticles used in this work smaller than 2 nm than the Coulomb blockade would be a logical explanation[25]. The Flg-A3 AuNPs however are 10 nm in diameter so it is unlikely that this is the source of the current decrease indicating much further study is required. Another interesting feature is the presence of the offset of the current in Figure 6.9a. The offset appears to be approximately 100 nA in magnitude. Correcting the I-V data by subtracting the value of the offset from the measured current values yields the I-V curve in Figure 6.9b. This particular I-V curve still shows an

approximate linear increase in current with an increase in applied bias however at 0 V the current is 0.

The source of the current offset has to be identified and eventually eliminated as it is inefficient to have a device conducting current even when no bias is applied. One potential source of this issue is charging. This could potentially be explained by incomplete network formation due to insufficient OPV concentrations. If an inadequate number of molecules bound between neighbouring nanoparticles then there would be areas in the network where there are no wires and consequently no current flow. One way to address this issue is to use higher concentrations of the OPV solution for network formation or attempt multiple insertions of the substrate in OPV solution. Multiple insertions into fresh OPV solution would hopefully maximize exposure to single units of OPV instead of oligomers of the molecule which would not bind between neighbouring nanoparticles. Oligomerization is known to occur over time as oxygen and water can oxidize thiols to form disulfide bonds.

6.5 Conclusions

Flg-A3 AuNPs were deposited on silicon dioxide substrates containing gold electrodes using the A3-QBP1 peptide. Prior to electrical measurements the films were treated with ultraviolet ozone cleaning to remove the peptide used to form the film. Preliminary SERS data suggests that the peptide can be completely removed from the film however much more study is required. SEM also showed that while some sample damage did occur there were large areas of the sample that retained their nanoscale features. While preliminary I-V data was observed in a junction with an electrode separation of 70 nm there was an offset present at 0 V which may be indicative of charging in the junction. The source of this offset remains unclear and further study is required to identify it and potentially remove it from the system.

6.6 References

(1) Conklin, D.; Nanayakkara, S.; Park, T.-H.; Lagadec, M. F.; Stecher, J. T.; Chen, X.; Therien, M. J.; Bonnell, D. a. *ACS Nano* **2013**, *7* (5), 4479–4486.
(2) Zhou, X.; Liu, H.; Yang, L.; Liu, J. *Analyst* **2013**, *138* (6), 1858–1864.
(3) Salvador, M.; MacLeod, B. A.; Hess, A.; Kulkarni, A. P.; Munechika, K.; Chen, J. I. L.; Ginger, D. S. *ACS Nano* **2012**, *6* (11), 10024–10032.
(4) Del Re, J.; Blum, A. S. *Appl. Surf. Sci.* **2014**, *296*, 24–30.
(5) Goulet, P. J. G.; Bourret, G. R.; Lennox, R. B. *Langmuir* **2012**, *28* (5), 2909–2913.
(6) Lopez-Sanchez, J. a; Dimitratos, N.; Hammond, C.; Brett, G. L.; Kesavan, L.; White, S.; Miedziak, P.; Tiruvalam, R.; Jenkins, R. L.; Carley, A. F.; Knight, D.; Kiely, C. J.; Hutchings, G. J. *Nat. Chem.* **2011**, *3* (7), 551–556.
(7) Gehl, B.; Frömsdorf, A.; Aleksandrovic, V.; Schmidt, T.; Pretorius, A.; Flege, J. I.; Bernstorff, S.; Rosenauer, A.; Falta, J.; Weller, H.; Bäumer, M. *Adv. Funct. Mater.* **2008**, *18* (16), 2398–2410.
(8) Menard, L. D.; Xu, F.; Nuzzo, R. G.; Yang, J. C. *J. Catal.* **2006**, *243* (1), 64–73.
(9) Ansar, S. M.; Ameer, F. S.; Hu, W.; Zou, S.; Pittman Jr, C. U. *Nano Lett.* **2013**, *13* (3), 1226–1229.
(10) Vig, J. R. *J. Vac. Sci. Technol. A Vacuum, Surfaces, Film.* **1985**, *3* (3), 1027.
(11) Vazquez, H.; Skouta, R.; Schneebeli, S.; Kamenetska, M.; Breslow, R.; Venkataraman, L.; Hybertsen, M. S. *Nat. Nanotechnol.* **2012**, *7* (10), 663–667.
(12) Widawsky, J. R.; Kamenetska, M.; Klare, J.; Nuckolls, C.; Steigerwald, M. L.; Hybertsen, M. S.; Venkataraman, L. *Nanotechnology* **2009**, *20* (43), 434009.
(13) Seferos, D. S.; Blum, A. S.; Kushmerick, J. G.; Bazan, G. C. *J. Am. Chem. Soc.* **2006**, *128* (34), 11260–11267.
(14) Aliaga, C.; Park, J. Y.; Yamada, Y.; Lee, H. S.; Tsung, C.; Yang, P.; Somorjai, G. a. *J. Phys. Chem. C* **2009**, *113* (15), 6150–6155.
(15) Crespo-Quesada, M.; Andanson, J. M.; Yarulin, A.; Lim, B.; Xia, Y.; Kiwi-Minsker, L. *Langmuir* **2011**, *27* (12), 7909–7916.
(16) Das, B. *Nanotechnology* **2010**, *21* (39), 395201.
(17) Tsoi, S.; Griva, I.; Trammell, S. a; Blum, A. S.; Schnur, J. M.; Lebedev, N. *ACS Nano* **2008**, *2* (6), 1289–1295.
(18) Blum, A. S.; Yang, J. C.; Shashidhar, R.; Ratna, B. *Appl. Phys. Lett.* **2003**, *82* (19), 3322.
(19) Kushmerick, J. G.; Holt, D. B.; Pollack, S. K.; Ratner, M. a; Yang, J. C.; Schull, T. L.; Naciri, J.; Moore, M. H.; Shashidhar, R. *J. Am. Chem. Soc.* **2002**, *124* (36), 10654–10655.
(20) Slocik, J. M.; Naik, R. R. *Adv. Mater.* **2006**, *18* (15), 1988–1992.
(21) Lee, K. Y.; Huang, W. S. *J. Vac. Sci. Technol. B Microelectron. Nanom. Struct.* **1993**, *11* (6), 2807.
(22) He, L.; Lamont, E.; Veeregowda, B.; Sreevatsan, S.; Haynes, C. L.; Diez-Gonzalez, F.; Labuza, T. P. *Chem. Sci.* **2011**, *2* (8), 1579.
(23) Pérez-Pineiro, R.; Correa-Duarte, M. a.; Salgueirino, V.; Alvarez-Puebla, R. a. *Nanoscale* **2012**, *4* (1), 113.
(24) Parker, J. H.; Feldman, D. W.; Ashkin, M. *Phys. Rev.* **1967**, *155* (3), 712–714.
(25) Morita, T.; Lindsay, S. *J. Am. Chem. Soc.* **2007**, *129* (23), 7262–7263.

7 Preliminary Studies Examining the Link Between Molecular Switching and Structure

7.1 Preface

Voltage-induced switching was studied in bipyridyl-dinitro oligophenylene ethynylene dithiol (BPDN), which has previously been shown to undergo this effect. BPDN and a derivative were studied to determine how the molecular structure played a role in the switching process. Preliminary results indicate that nitro groups are not a requirement for switching but do enhance the effect, while the bipyridal group also undergoes switching, which is irreversible in nature. Charging effects were also observed and therefore they may play a role as well, however further study is required.

7.2 Introduction

Ever since Aviram and Ratner's ground-breaking paper launched the field of molecular electronics in 1974 it has attracted a significant amount of interest[1]. There exists a significant body of work demonstrating conduction through a variety of molecules such as alkanethiols[2], oligo(phenylene vinylenes)[3,4] and oligo(phenylene ethylenes)[5,6]. This has proved to be invaluable in understanding charge transport in molecular junctions. In order to further continue the development of molecular electronic devices for technological applications, it is necessary to understand non-linear charge transport such as diode behaviour or voltage induced changes in transport such when a conducting molecule switches between a high and low conductance state.

Switching behaviour has been previously described in the literature and attributed to a variety of mechanisms[7–9]. One such example is stochastic switching, which is the result of random, statistical fluctuations[10]. It is thought that this arises from changes in the molecular

geometry, and since it is independent of variables like applied bias, it is an unreliable tool for incorporating switching functions into molecular devices[11]. For technological applications, it should be possible to control switching behaviour with an external stimulus. Voltage-induced switching has been previously reported, but the mechanisms behind it are not well understood[12,13]. An example of a molecule that can exhibit this sort of behaviour is bipyridyl-dinitro oligophenylene ethynylene dithiol (BPDN)[12]. One plausible explanation is that the structure plays a significant role in this observed behaviour. The effect of molecular structure on the gap between the highest molecular orbital (HOMO) and lowest unoccupied molecular orbital (LUMO) is well-understood,[14] however less is known how different functional groups affect charge transport[15].

The following chapter attempts to understand how the structure of BPDN contributes to its ability to undergo voltage-induced switching. The electrical properties of a BPDN derivative lacking nitro groups (Scheme 7.1) were studied to elucidate the effect that the bipyridal core may have on the switching behaviour observed. The results were compared to the original BPDN molecule (Scheme 7.1).

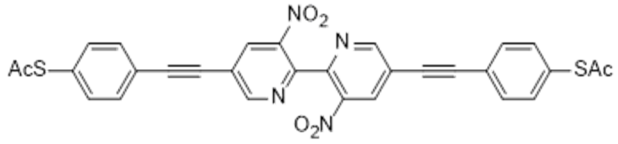

1

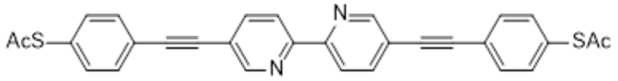

2

Scheme 7.1. Molecular structures of BPDN (1) and a BPDN derivative that is missing the nitro group (2).

7.3 Experimental

Gold (111) (SPI Supplies, Westchester, PA) was immersed in a 1 mM solution of 1-decanethiol (Sigma Aldrich, Missisauga, ON) in ethanol and left to incubate for 18 hours to form a C10 self-assembled monolayer (SAM). Upon removal from the thiol solution, the SAM was rinsed with ethanol. 1.5 mg of **1** or **2** was then dissolved in 4 ml of anhydrous tetrahydrofuran (THF) under an inert, nitrogen atmosphere. 20 μL of concentrated ammonium hydroxide was added to the solution, and the C10 self-assembled monolayer (SAM) was immersed in this solution for an hour. The SAM was then rinsed with THF and ethanol. The multicomponent SAM was then immersed in a suspension of 5 nm colloidal gold nanoparticles (SPI Supplies, Westchester, PA). The SAM was then rinsed with deionized water and dried with a gentle stream of nitrogen gas.

7.4 Results and Discussion

Molecules of **1** and **2** were isolated in an insulating C10 alkanethiol monolayer. This particular technique for studying the electrical properties of molecular junctions is particular in well-defined insulating environments. Scanning tunneling microscopy (STM) was used to characterizing the molecules. Individual junctions of the test molecules appear as bright protrusions in the insulating monolayer (Figure 7.1). Single molecules tended to insert themselves around gold vacancy islands.

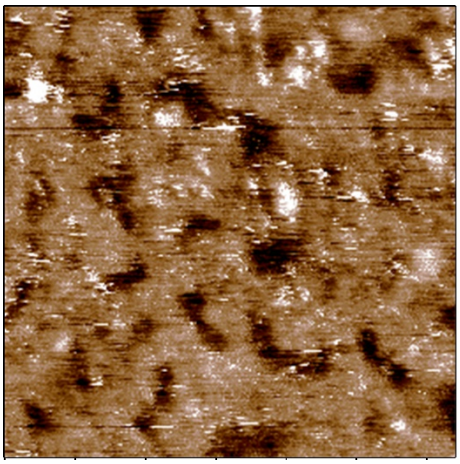

Figure 7.1 A 65 by 65 nm^2 STM image of 2 inserted in a C10 alkanethiol monolayer. V_{bias} = 500 mV, I = 1 nA

The I-V characteristics of the test molecules were studied by positioning the STM tip over the junction and sweeping the voltage from -1.5 V to 1.5 V and back to -1.5 V (Figure 7.2). For molecules **1** and **2**, a discontinuity was frequently observed as the bias voltage increased from 0 to 1.5 V. This discontinuity corresponds to a sudden increase in tunnelling current. Upon reversing the sweep from 1.5 V to 0 V, the tunneling current remained larger than for the initial pre-discontinuity sweep. This observation suggests that the molecule can exist in two different states, which have different charge transport properties. Approximately 80 % of the junctions for **1** and **2** that were studied displayed this two state behaviour.

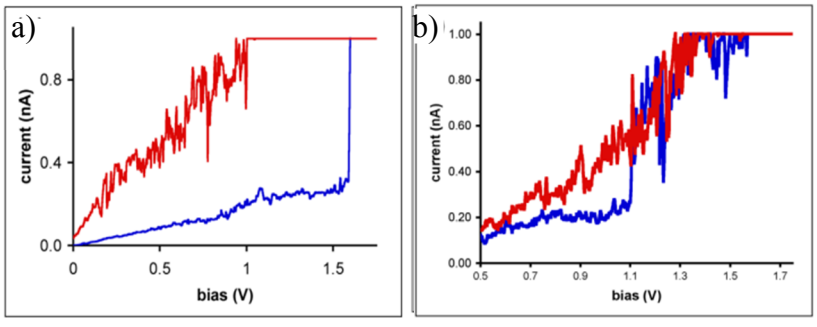

Figure 7.2 I-V data for a) 1 and b) 2. The blue indicates when the voltage is being increased and the red denotes when the voltage is being decreased.

Examination of the I-V curves reveals that **1** and **2** appears to switch to a high conductance between 1 and 1.5 V. This effect is significantly more pronounced for **1** though. Furthermore the molecules remain in this state until the voltage is reduced to 0 V. At this point it returns to its low conductance state. For molecule **1**, this switching between high and low conductance states appears to be reversible and reproducible in subsequent sweeps with 90 % of junctions showing reversible switching (Figure 7.2a)[12] . In contrast, in the case of **2** only 20 % of the junctions studied showed the ability to reversibly switch between high and low conductance states (Figure 7.2b). The functional groups on the molecular wire are known to impact the measured current in a molecular wire[15] and it is also thought that these can play a role in voltage-induced mechanisms for reasons that are not well understood[16]. The results indicate that the nitro groups are not necessary for switching however they do enhance the effect.

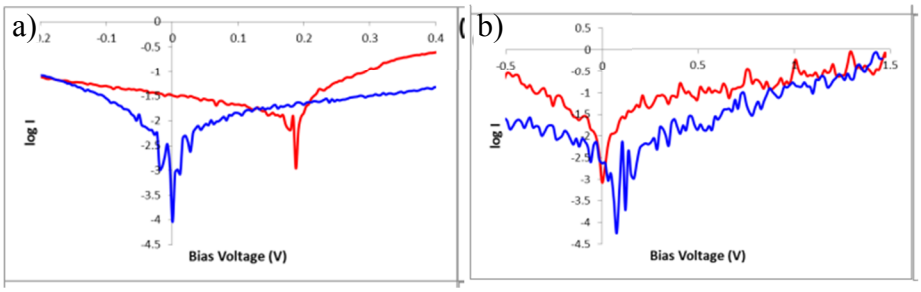

Figure 7.3 LogI vs bias data for a) **1** and b) **2**. The blue indicates when the voltage is being increased and the red denotes when the voltage is being decreased.

To further analyze the data and help elucidate possible mechanisms, logI vs bias plots were made for the collected I-V curves (Figure 7.3). Examination of Figure 7.3 reveals the the lowest current point, which should occur at 0 V in a tunneling experiment, is offset from 0 V for one of the conductance states in both **1** and **2**, however the effect is less pronounced in **2**. In addition, the offset is opposite in nature between molecules **1** and **2.** For **1,** the lowest current point for the high conductance state is shifted positive from the low conductance state. For **2**, the

lowest current point for the high conductance state is shifted negative from the low conductance state. The presence of this shift is indicative that there may be charging occurring such that the local bias experienced by the molecule is different from the applied bias voltage. Originally, a charge-based mechanism was thought to not contribute to switching of **1** however these results indicate that charging may indeed play a role[17]. Since the bipyridal group is the common link between **1** and **2,** the difference in charging effects can be attributed to the nitro groups on **1**. To further understand what was going on, the ratio between the current in the high and low conductance state at 0.5 V was calculated (Table 7.1). This particular bias was chosen because at this point the high and low conductance values can be clearly determined.

Table 7.1 Voltage-Triggered Switching Data for Molecules 1 and 2

Molecule	**% Molecules observed switching**	**% I-V curves observed switching for an individual molecule**	**High conductance to low conductance ratio**	**Offset from low state**
1	95	90	30 $\pm$ 10	+0.10 $\pm$ 0.04 V
2	83	20	3.5 $\pm$ 2	-0.09 $\pm$ 0.04 V

Examination of Table 7.1 further solidifies the I-V data that suggests that the nitro groups enhance the switching effect, but are not a requirement to observe the phenomenon. The results also indicate that charging may play a role, however more data is needed. The subsequent steps involve looking at other BPDN analogs to determine the effect that they have on switching behaviour in order to fully elucidate the mechanism for voltage-induced switching.

7.5 Conclusion

The electrical properties of BPDN and a derivative were studied in order to elucidate a mechanism for voltage-induced switching. The molecular structure appears to play a role however it is still not entirely clear what role exactly. It was found that nitro groups enhance

switching behaviour however they are not a requirement for switching. A bipyridal core was also found to exhibit switching behaviour however it is not reversible making it difficult to determine its role in the phenomenon. Charging effects may play a role however more BPDN derivatives need to be studied to solidly determine a mechanism.

7.6 References

(1) Aviram, A.; Ratner, M. A. *Chem. Phys. Lett.* **1974**, *29*, 277–283.
(2) Morita, T.; Lindsay, S. *J. Am. Chem. Soc.* **2007**, *129*, 7262–7263.
(3) Del Re, J.; Moore, M. H.; Ratna, B. R.; Blum, A. S. *Phys. Chem. Chem. Phys.* **2013**, *15*, 8318–8323.
(4) Blum, A. S.; Kushmerick, J. G.; Pollack, S. K.; Yang, J. C.; Moore, M.; Naciri, J.; Shashidhar, R.; Ratna, B. R. *J. Phys. Chem. B* **2004**, *108*, 18124–18128.
(5) Hong, W.; Li, H.; Liu, S.-X.; Fu, Y.; Li, J.; Kaliginedi, V.; Decurtins, S.; Wandlowski, T. *J. Am. Chem. Soc.* **2012**, *134*, 19425–19431.
(6) Martín, S.; Grace, I.; Bryce, M. R.; Wang, C.; Jitchati, R.; Batsanov, A. S.; Higgins, S. J.; Lambert, C. J.; Nichols, R. J. *J. Am. Chem. Soc.* **2010**, *132*, 9157–9164.
(7) Liao, J.; Agustsson, J. S.; Wu, S.; Schönenberger, C.; Calame, M.; Leroux, Y.; Mayor, M.; Jeannin, O.; Ran, Y.-F.; Liu, S.-X.; Decurtins, S. *Nano Lett.* **2010**, *10*, 759–764.
(8) Dhungana, K. B.; Mandal, S.; Pati, R. *J. Phys. Chem. C* **2012**, *116*, 17268–17273.
(9) Van der Molen, S. J.; Liao, J.; Kudernac, T.; Agustsson, J. S.; Bernard, L.; Calame, M.; van Wees, B. J.; Feringa, B. L.; Scho nenberger, C. *Nano Lett.* **2008**, *9*, 76–80.
(10) Bâldea, I. *J. Am. Chem. Soc.* **2012**, *134*, 7958–7962.
(11) Basch, H.; Cohen, R.; Ratner, M. a. *Nano Lett.* **2005**, *5*, 1668–1675.
(12) Blum, A. S.; Kushmerick, J. G.; Long, D. P.; Patterson, C. H.; Yang, J. C.; Henderson, J. C.; Yao, Y.; Tour, J. M.; Shashidhar, R.; Ratna, B. R. *Nat. Mater.* **2005**, *4*, 167–172.
(13) Seo, K.; Konchenko, A. V; Lee, J.; Bang, G. S.; Lee, H. *J. Am. Chem. Soc.* **2008**, *130*, 2553–2559.
(14) Kushmerick, J. G.; Holt, D. B.; Pollack, S. K.; Ratner, M. a; Yang, J. C.; Schull, T. L.; Naciri, J.; Moore, M. H.; Shashidhar, R. *J. Am. Chem. Soc.* **2002**, *124*, 10654–10655.
(15) Venkataraman, L.; Park, Y. S.; Whalley, A. C.; Nuckolls, C.; Hybertsen, M. S.; Steigerwald, M. L. *Nano Lett.* **2007**, *7*, 502–506.
(16) Lörtscher, E.; Ciszek, J. W.; Tour, J.; Riel, H. *Small* **2006**, *2*, 973–977.
(17) Keane, Z. K.; Ciszek, J. W.; Tour, J. M.; Natelson, D. *Nano Lett.* **2006**, *6*, 1518–1521.

8 Conclusions and Future Directions

8.1 Conclusions

In this thesis the properties of single molecular wires were investigated as well as methods for integrating them into functional devices. The single molecule experiments demonstrated that the conduction of molecular wires is sensitive to their local environment thus rendering them useful in sensing applications. Moreover, the switching properties of a molecular wire were studied in order to better understand the phenomenon of voltage-induced switching. The thesis also examined the use of gold nanoparticle networks for integration of conducting molecules into functional devices. A facile method was developed for forming densely-packed gold nanoparticles on silicon dioxide substrates using peptides to control the nanoparticle synthesis, assembly and binding. These nanoparticle films were also studied for their use in molecular electronic devices by plating them on silicon dioxide surfaces with lithographically-defined gold electrodes in an attempt to form a functional molecular circuit. Ultraviolet ozone cleaning was used to strip the peptide once the films had been formed and they were then characterized electrically. In order to further enhance the assembly properties of the nanoparticles their binding to tobacco mosaic virus coat protein (TMVcp) disks was studied.

In Chapter 3 it was demonstrated that the conduction of oligophenylene (OPV) molecules is sensitive to nitroaromatic molecules in its local environment thus creating the potential to develop a novel sensor. It is suspected that this was a result of π donor-acceptor interactions between an analyte rich in electron-withdrawing groups and OPV. Three analytes were studied: 1,4-dinitrobenzene, nitrobenzene and toluene. It was expected that toluene would not have any effect on conduction as it does not contain electron-withdrawing groups and experiments confirmed this. Nitrobenzene and 1,4-dinitrobenzene both caused measurable decreases in OPV

conduction. 1,4-dinitrobenzene had the largest effect which is expected since it contains an additional electron-withdrawing nitro group. In order to confirm that observed effects were from π donor-acceptor interactions the electrical measurements were correlated with fluorescence measurements on OPV. The same analytes were studied to see what effect they would have on fluorescence intensity. The analytes behaved exactly as they did in the electrical measurements. Toluene did not affect the fluorescence intensity while both nitrobenzene and 1,4-dinitrobenzene did with the latter having a larger effect. This confirms the hypothesis that the changes in conduction are a result of π donor-acceptor interactions. The next step becomes to look at integrating the molecule into a functional molecular circuit.

Gold nanoparticle networks on insulating substrates have been one proposed solution for integrating conducting molecules into functional devices. One requirement for the gold nanoparticle networks is that the nanoparticles are spaced closely enough together so that molecular wires are capable of binding between two neighbouring nanoparticles. If the nanoparticles are too far apart the molecule fails to bind and the device's efficiency is diminished because of conductive breaks. In Chapter 4 fusion peptides gold nanoparticles were successfully bound to silicon dioxide substrates with a high surface coverage. Gold nanoparticles were synthesized using the Flg-A3 peptide which stabilizes the resulting AuNP and allows it to form stable solution-phase aggregates via transition metal ion interactions. While a variety of metal ions were tests the nanoparticles formed the largest aggregates upon addition of Zn^{2+} to the AuNP dispersion. With these aggregates the nanoparticles were sufficiently close to make them useful for molecular electronics applications. Using the A3-QBP1 peptide these aggregates were bound to silicon dioxide substrates. Scanning electron microscopy demonstrated that while the

Flg-A3 AuNPs can bind non-specifically to the substrate the A3-QBP1 peptide is necessary to achieve excellent surface coverage.

In an attempt to increase the size of the aggregates which the Flg-A3 AuNPs form they were covalently bound to TMVcp disks in Chapter 5. It was thought that if the N terminus, which lies along the circumference of the disk, was modified with an α-lipoic acid moiety AuNPs would covalently bind to it and form rings which could then be studied the same way that the free AuNPs were studied in Chapter 4. Initially an attempt was made to modify a mutant of TMVcp, where a serine residue was replaced with a cysteine at the 123 position and prefers the disk phase. It was found though that in this configuration the N terminus is sterically hindered which lead to low conjugation yields. The TMVcp was mutated and three additional amino acids were added at the N terminus to make it more accessible in solution. This increased conjugation yields dramatically. It was then possible to covalently bind Flg-A3 AuNPs to the conjugated disk forming gold nanorings.

In Chapter 6 the Flg-A3 AuNP films were formed on silicon dioxide substrates which had gold electrodes in hopes of forming a functional molecular electronic device with OPV. Following film formation the sample was treated with ultraviolet ozone cleaning to remove the peptide leaving bare nanoparticles thus facilitating OPV integration. Preliminary surface enhanced Raman spectroscopy (SERS) data did suggest complete peptide loss though further study is required especially for longer surface treatment times. Furthermore, scanning electron microscopy (SEM) showed that while areas of the film maintained their nanoscale features other sections were damaged which is thought to be the result of localized heating of the nanoparticles which caused them to melt. When electrical measurements were carried out with OPV the junctions did display I-V character however there was an offset present at 0 V which may be

indicative of charging. It is possible that the OPV concentration was too low and the molecule failed to bind between neighbouring nanoparticles in some areas of the film thus leading to insulating sections of the network.

Preliminary work in Chapter 7 also looked at understanding voltage-induced switching in bipyridyl-dinitro oligophenylene ethynylene dithiol (BPDN), a molecule known to exhibit this phenomenon. The molecular wire displayed a high and low conductance state which was dependent on the applied bias. While further study is still required the data is suggesting that the molecular structure does play a role in voltage-induced switching. Moreover nitro groups present in the molecule seem to enhance the effect but they are not a requirement for it. Further study is needed though to fully understand the role that molecular structure plays in switching.

8.2 Future Directions

The following work leads to many new directions for future work. First and foremost it is necessary to continue working on forming a functional molecular electronic device by integrating OPV into AuNP films made using Flg-A3 AuNPs. The first step is to continue surface treatments of the Flg-A3 AuNP films to further characterize them with SERS and determine the exact point at which the peptide is completely removed. From there the next step is to identify the source of the current offset in the I-V curves and eliminate it. One possible suggestion is to work with higher concentrations of OPV to decrease the likelihood of it not binding between neighbouring nanoparticles. Another option is to do multiple insertion steps with the molecule to ensure that the formation of the metal nanoparticle – molecular networks goes to completion.

It would also be very interesting to carry out further electrical characterization of the molecular circuits to gain a better understanding of their properties. Conductive probe atomic

force microscopy (Cp-AFM) could provide interesting information about charge flow through the networks. In the area of organic photovoltaics Cp-AFM has been used to show areas of high and low conductivity when the device is in the off state, thus making it possible to distinguish between the different polymeric components of the device[1]. The combination of localized conduction measurements with topographic information could provide key insights on how network topology impacts charge flow in a network of nanoparticles. Since the networks are on a strongly insulating substrate, it may be possible to infer that any areas of high current in the current retrace images are due to lateral current flow through the network[2].

Ideally a subsequent step would be to look at using the molecular circuits as sensors for nitroaromatic molecules. This would involve testing the conductivity of the network in response to these analytes in the local environment. Based on the observations made in Chapter 3, it is expected that network conductivity would decrease as the nitroaromatics form π donor-acceptor interactions with OPV molecules exposed at the surface of the circuit. In order to make molecular electronics based devices practical for use as sensors, it would be necessary to look at how sensitive the device is and establish limits of detection. Furthermore, it would also be necessary to characterize how rapidly the sensor could detect analytes. In order to be practical it must be capable of quick detection. Lastly it would also be necessary to confirm that the sensor is selective for nitroaromatic analytes.

Another interesting direction for this particular work would be to study whether or not exciting the plasmon of the nanoparticles imparts any interesting optoelectronic properties on the network. Conklin et al. have demonstrated that in molecules capable of conducting photocurrent, the plasmon of the metallic nanoparticles can enhance the measured photoconductance. It is thought that when the plasmon is excited, “hot” charge carriers can be extracted from the

nanoparticle and can contribute to the measured current[3]. It has already been demonstrated that OPV has optoelectronic properties[4]. It would therefore be very interesting to see if any photocurrent could be measured in this particular setup and whether or not exciting the plasmon of the gold nanoparticles enhances that effect.

Lastly, another avenue worth pursuing would be to test the versatility of these particular networks. In order to accomplish this, the type of molecular wire being used should be alternated. One example would be to look at incorporating BPDN into the device with the hopes of being able to form a molecular circuit that could switch between an off and on state.

The preliminary data on BPDN demonstrated that molecular structure may play a role in voltage-induced switching. Further studies are needed though to truly confirm this hypothesis. The subsequent steps should look at studying how other parts of the structure affect switching properties. One such example would be to study a BPDN analog where the bipyridal groups have been replaced by benzene rings or benzene rings containing nitro groups to see if switching is still observed.

The successful binding of Flg-A3 AuNPs to TMVcp would open the door to many interesting new avenues for research. The first step is to study the aggregation properties of the rings once the yield has increased and the remaining free nanoparticles have been removed from solution. The logical step would be to study the same metal ions examined in Chapter 4 and to characterize the aggregation properties (Figure 8.1). If the yield could really be increased then it may be possible to characterize the samples optically by measuring the shift in the surface plasmon resonance band (SPR) in the UV/VIS spectrum. Furthermore, dynamic light scattering measurements could also be done to confirm possible aggregation effects.

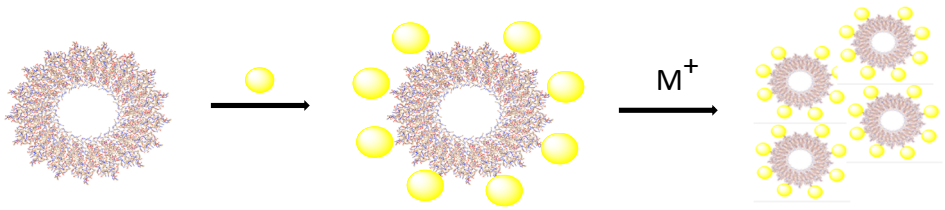

Figure 8.1 Proposed scheme for studying the aggregation properties of Flg-A3 TMVcp rings

Following successful solution-phase aggregation of the Flg-A3 AuNP TMVcp rings the subsequent step would be to see if they can be deposited on silicon dioxide substrates for molecular electronics measurements (Figure 8.2) akin to what was done in Chapter 6. It is expected that these aggregates would be significantly larger than the ones formed from the free nanoparticles in Chapter 3, which could potentially enable the use of larger gaps in these devices. The obvious advantage to this would be that photolithography could be used to define the gap between electrodes instead of electron beam lithography which would greatly speed up the process of making the devices.

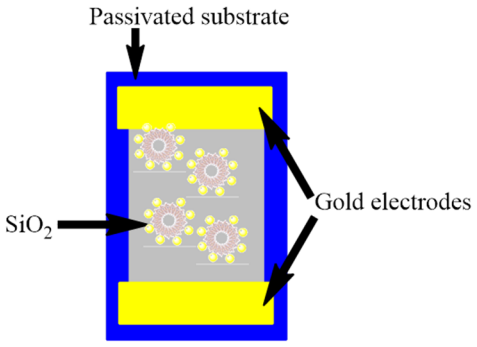

Figure 8.2 The final step would be to look at depositing the Flg-A3 AuNP TMVcp rings on silicon dixide substrates for molecular electronics measurements akin to what was done in Chapter 4.

8.3 References

(1) Pingree, L. S. C.; Reid, O. G.; Ginger, D. S. *Adv. Mater.* **2009**, *21*, 19–28.

(2) Hendriksen, B. L.; Martin, F.; Qi, Y.; Mauldin, C.; Vukmirovic, N.; Ren, J.; Wormeester, H.; Katan, a J.; Altoe, V.; Aloni, S.; Frechet, J. M.; Wang, L. W.; Salmeron, M. *Nano Lett* **2011**, *11*, 4107–4112.

(3) Conklin, D.; Nanayakkara, S.; Park, T.-H.; Lagadec, M. F.; Stecher, J. T.; Chen, X.; Therien, M. J.; Bonnell, D. a. *ACS Nano* **2013**, *7*, 4479–4486.

(4) Mangold, M. a; Calame, M.; Mayor, M.; Holleitner, A. W. *J. Am. Chem. Soc.* **2011**, *133*, 12185–12191.